博士学位論文

Analytical and Experimental Study for Interfacial Slip in Shrink- Fitted Bimetallic Work Roll

スリーブ組立式ロールにおける界面すべりに関する解析的及び実験的研究

Rahimah Binti ABDUL RAFAR

Supervisor: Prof. Nao-Aki Noda

Thesis submitted to the Graduate School of Engineering, Kyushu Institute of Technology, in Fulfilment of the Requirements for the degree of

Doctor of Philosophy in Engineering

March 2022

Abstract

Among rolling rolls used in steel industries, instead of a solid roll, sleeve assembly types were tried to be used and some of them were practically and successfully used by shrink-fitting shafts into a hollow cylinder. They have some advantages for back-up rolls having a large trunk diameter exceeding 1000mm and also for large H-section steel rolls. The sleeve assembly type roll has the advantage that the shaft can be reused continuously by replacing only the worn sleeve due to the rolling. In addition, materials with excellent wear resistance and heat resistance, such as super cermet rolls and ceramic rolls, have poor toughness and high cost. Since these rolls are impractical, the sleeve assembly type structure is essential. On the other hand, this shrink-fitted structure has several peculiar problems such as residual roll bending and sleeve cracking due to the circumferential sleeve slip. The circumferential slippage sometimes occurs even the resistance torque at the interface is larger than the motor torque.

Therefore, it is important to clarify the cause of the sleeve slip phenomenon in a sleeve structure. In this paper, the mechanism of interfacial slip in a sleeve assembly type roll constructed by shrink-fitting is verified by FEM analysis, and to apply it to the actual machine, the roll material, the fitting conditions, and the effect of the rolling load is considered. Finally, the experimental method of a miniature roll is demonstrated to verify the analysis. This paper consists of 7 chapters and is organized as follows.

Chapter 1 introduced the bimetallic work roll and the problems encountered in the sleeve assembly type rolls. Although the shrink-fitting sleeve assembly roll has many advantages compared to the solid roll, it also has unique problems such as residual bending and sleeve slip. Therefore, the necessity to clarify the sleeve slip in the bimetallic work roll is described in this paper.

In Chapter 2, the mechanism of the sleeve slip formation under free rolling for the hot rolling roll is considered. It has been shown that the sleeve slippage, known as an interfacial creep in bearings, is formed from the accumulations of the relative displacements on the shrink-fitted surface. In the actual roll problem, it is necessary to consider not only the sleeve but also the elastic deformation of the shaft, and the relative displacement between sleeve and shaft caused the interfacial slip. Therefore, in this chapter, to get closer to the actual rolling conditions, the effect of elastic deformation of the shaft on the interfacial slip is investigated under the free rolling state with reference to the previous study which the shaft is a rigid body. Furthermore, in addition to the steel shaft, other shaft materials are also considered to clarify the effect of elastic deformation of the shaft material on the interfacial slip.

In Chapter 3, as in the previous chapter, the effect of rolling torque on the interfacial slip is considered for hot rolling rolls. In this chapter, the motor torque with the frictional force from the rolled steel may promote the slippage in the sleeve rolls significantly causing serious failure. Therefore, the motor torque effect will be investigated quantitatively. In this sense, the effects of the shrink-fitting ratio and the friction coefficient which are the parameters of the resistance torque are also considered since they may contribute to slippage resistance. Here, the interface slip and the displacement increase rate are analyzed.

In Chapter 4, the interfacial slip in shrink-fitted roll is confirmed experimentally under free rolling conditions by using a miniature roll. Then, the behavior of the sleeve slip obtained in the experiment is considered and is compared with the numerical analysis results. The length of the scratch observed from the marking line of the miniature roll is equal to the calculated length of the scratch on the sleeve inner surface. This clarified that the relative slippage caused scratches on the interface. Also, it has been observed that the scratch caused by the interfacial slip forms a large egg-shaped. In addition, the effect of the sleeve inner surface scratches due to the interfacial slip on the sleeve strength is considered. In this chapter, the fatigue risk in terms of the stress concentration factor, Kt of the defect is evaluated.

Chapter 5 focuses on the high-speed steel bimetallic sleeve rolls, which are made by shrink-fitting the composite sleeve and shaft. In this chapter, the inner surface stress of the sleeve caused by the sleeve slippage under the actual rolling conditions is obtained by numerical simulation; then its effect on fatigue fracture is clarified. Here, the damage caused by the sleeve slip is regarded as a defect, and the fatigue limit obtained by considering the root area $\sqrt{area}$ of the defect is used in the durability diagram to evaluate the safety side of the damage in the sleeve roll. In this chapter, the maximum stress, minimum stress, and stress amplitude is clarified. It is shown that the stress amplitude under the impact force condition is significantly increased about twice from the standard condition.

In Chapter 6, the difference of the residual stress generated between the bimetallic solid roll and the current study of bimetallic sleeve roll constructed by shrink-fitting is studied. Two types of the manufacturing process are considered in this chapter. Method 1 is turning inside of the solid roll after heat treatment. Method 2 is heat treatment after turning inside of the solid roll. The results show that Method 2 is better than Method 1 since the tensile residual stress can be reduced at the inside of the sleeve. After shrink-fitting of the shaft, the residual stress is compared with one of the solid rolls. Then, the evaluation of the fatigue risk in consideration of the residual stress is also studied.

Chapter 7 summarizes the main conclusions of this study.

5 The inner surface stress and fatigue fracture analysis of shrink-fitted bimetallic sleeve roll..104

6 Residual stress simulation for bimetallic sleeve roll........................131

1 Introduction

1.1 Research background

Many metalworking companies use rolling in their production method. The demands are not only for the high quality of metal sheets but also high productivity, energy-saving, and cost-effective operation. The rolling process is a metal forming process carried out in a rolling mill in which metal/steel stock is passed through one or more pairs of roll operations such as transportation of stock to rolls, disposal after rolling, cutting, melting, piling or coiling as described in Fig. 1-1(a). The most commonly rolling used in metalworking is the hot rolling mill. Among the hot strip rolling mill, this study considers 4-high rolling mill. A 4-high rolling mill has four horizontal rolls is arranged in a single vertical plane as shown in Fig. 1-1(b). Two rolls (inner) are the work rolls and two rolls (outer) are the back-up rolls. In the 4-high rolling mill processes, the work rolls are driven while the back-up rolls are friction driven.

The important factor where roll life is concerned is the wear properties of the roll material. The work roll body is the most important part of the rolling mill because it works on the most difficult conditions consisting of high temperatures and pressures from the input material and also from the back-up roll. Under the conditions of the continuous rolling process, the contact area of the roll experiences wears. Because of the wear surface on the work roll body for example abrasion and the surface roughening, the work roll tends to consume in a short period of time. In addition, to avoid catastrophic wear in the rolling mill, the total roll body with wear will be removed from the mill stand and changed with the new roll body. For conventional rolls, material consumptions are large and the exchange cost is high to change the whole roll.

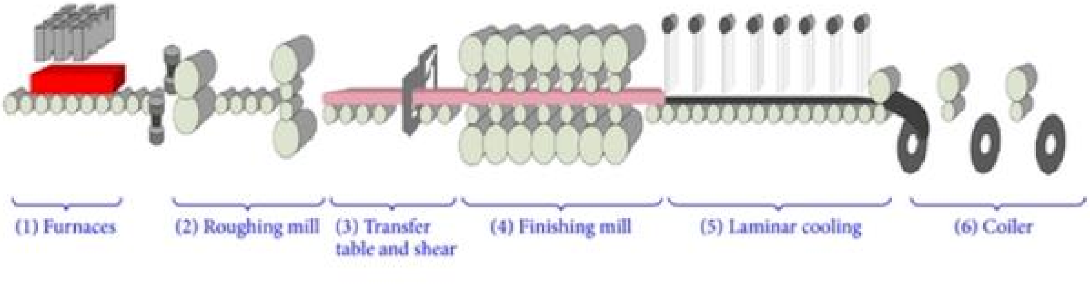

(a) Hot strip layout and working

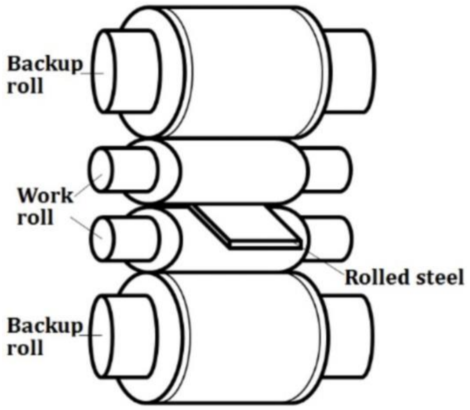

(b) Four-high rolling mill

Fig. 1-1 Hot rolling mill

Since rolls are very costly consumables in a rolling mill and to increase the practicability of the rolling roll, bimetallic work rolls are tried to be used and some of them are practically and successfully used in the steel industries to replace the single conventional roll. Regarding the bimetallic work roll, the sleeve assembly types as shown in Fig. 1-2(c)in which the shaft is shrink-fitted into the hollow sleeve are considered in this study. Many studies have been conducted regarding the manufacturing of the bimetallic work roll [1-35]. The shrink-fitted assembly type has some advantages for back-up rolls having a large diameter that exceeded 1000mm [4] and also for large H-section rolling steel [6, 7]. In addition, in the shrink-fitted assembly type roll, the shaft can be reused even the roll body has already reached the threshold minimum diameter.

Furthermore, the sleeve wear resistance can be improved independently without loosening the shaft ductility.

1.2 Bimetallic sleeve assembly type roll

In the technology of hot rolling, the steel industries have been making efforts to improve the product quality and to develop the rolling process with many innovations. Since the hot rolling rolls are used under very severe cyclic heat shock, heating up with rolled material and cooling down by cooling water, various roll wear modes exist for example abrasion and thermal fatigue. The abrasive wear is caused by rubbing contact between the rolls and the metal stock, and also from the contact of the back-up roll and work roll. The thermal fatigue cracks are from huge thermal stress due to the large temperature difference. In detail, the alternately deep heating on the roll surface by contacting hot steel and deep cooling by water spray will induce large circumferential compressive stress and tensile stress. These surface stresses can be severe enough to exceed the yield stress of the roll material and cause the surface layer to deform plastically [36]. Therefore, it is important for the hot rolling roll to have superior performance such as excellent resistance to wear and surface roughening, high toughness and strength, and excellent heat crack resistance.

Since the work roll life of hot rolling mills is strongly affected by roll material, a composite or bimetallic sleeve roll for example the super-cermet roll [23] and ceramic roll [24] has been developed to improve further work roll life. These rolls are suitable for maintenance and reducing the cost because the roll body with wear can exchange the sleeve part only. In addition, these types of rolls have high temperature resistance and high wear and corrosion resistance

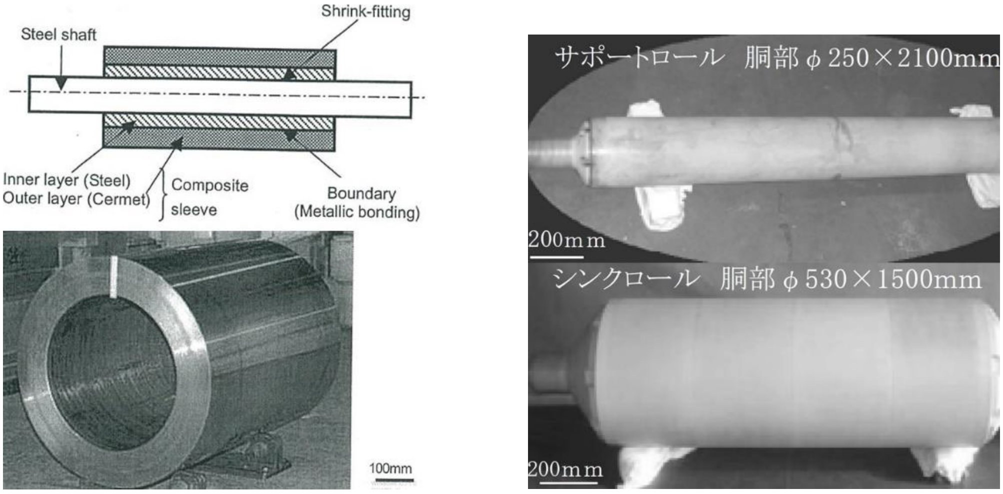

(a) Super-cermet roll (b) Ceramic roll

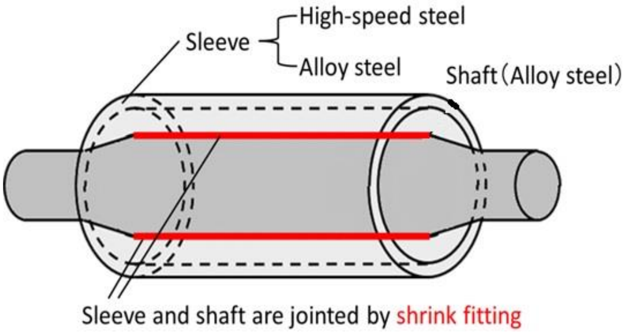

(c) Bimetallic sleeve roll

Fig. 1-2 Bimetallic hot strip mill work roll

Fig. 1-2(a) shows a super-cermet roll in which the steel shaft is shrink-fitted to the composite sleeve which is composed of cermet as an outer layer and steel as an inner layer. In the super-cermet roll, the bonding strength between cermet and steel which is the weakest part of the roll has been increased over 1000MPa which makes the roll has high strength and high anti-adhering behavior.

Fig. 1-2(b) shows a ceramic sleeve roll where two short steel shafts are connected by shrink-fitting to both ends of the ceramic sleeve. In a previous study [37], the steel sleeve and the steel shaft are connected by shrink-fitting, and the steel sleeve is coated by ceramic on the surface to improve wear resistance.

However, the mismatch of the thermal expansion may induce surface failure such as crack, peeling, wearing resulting in short roll life. If the total structure of the sleeve roll is ceramic, it may prevent most of the defects observed at the coated ceramic roll, hence extending the roll life significantly. However, these rolls are impractical because of their poor toughness and high cost.

In the work roll structure, fracture toughness is required at the roll center while wear resistance and heat resistance are required at the roll surface. Therefore, a new composite roll or bimetallic sleeve roll as shown in Fig. 1-2(c) in which the steel shaft is shrink-fitted to the composite sleeve which is composed of high-speed steel (HSS) as an outer layer and ductile cast iron (DCI) as an inner layer is widely used. This bimetallic sleeve roll or known as the HSS roll has excellent hardness, wear resistance, and high temperature properties, and the core layer consisting of cast iron or forged steel has high strength and toughness [38].

1.3 Sleeve slippage problem on shrink-fitted structure

Hot rolling is an important steel production process. The conditions of the rolls in a hot rolling mill becoming stricter since it cost significantly and influences the quality of products. The rolling process of hot steel is often done hot, and an alternate heating and cooling cycle is added to the rolling rolls at each roll rotation. In addition, the rolling roll is loaded with hundreds to thousands of tons. Thus it must be ensured that the physical dimensions and material of the roll are capable of withstanding severe extremes of temperature and load. For this reason, the shaft is required to have strength and toughness to withstand high loads, and the body is required to have heat resistance, wear resistance, and high hardness against thermal and mechanical loads. To meet these requirements, composite solid rolls with separate outer and inner layers are often used. In addition, to achieve a quality target, the outer layer of the roll can be made from high-alloy steel and the inner layer can be made from tough forged steel.

In order to ensure the process is economical, the sleeve assembly rolls have been developed for rolling roll (Fig. 1-2(c)) [1-10, 23-35]. In the sleeve assembly roll, the inner layer or shaft is shrink-fitted to the outer layer or sleeve body. Fundamentally, shrink-fitting is a simple operation involving either contraction or expansion of one component on another to cause interference and the development of pressure, holding the two components together mechanically. Usually, the temperatures involved in heating for expansion are significantly lower to avoid changes in metallurgical structure as in tempering or melting. In practice, parts assembled by shrink-fitting can be disassembled by selectively heating the outside component. The shrink-fitting operation offers advantages to the inner part of the roll body to be reused when the outer layer needs to be exchanged.

One of the examples of a sleeve assembly type roll is a large trunk back-up roll of 4- high rolling mill. The sleeve back-up roll consists of a roll core made of high ductile steel material, and a roll sleeve made of high hardness and high wear resistant steel material. Then, these two parts are assembled together by shrink-fit. The application and development of sleeve back-up roll present several advantages in preventing roll break, increasing operating rate, and reducing roll consumption and the cost of rolling. However, the residual roll bending occurs during the operation in which the roll core remains bent after rolling [27, 30]. In addition, sleeve breakage due to the circumferential sleeve slip during the rolling process has been reported Fig. 1-3 [32-35]. During the rolling, the circumferential slip may occur in the shrink-fitting surface and leads to the sleeve slippage. This slippage will cause local swell and it will then become a stress concentration

(a) Outer surface

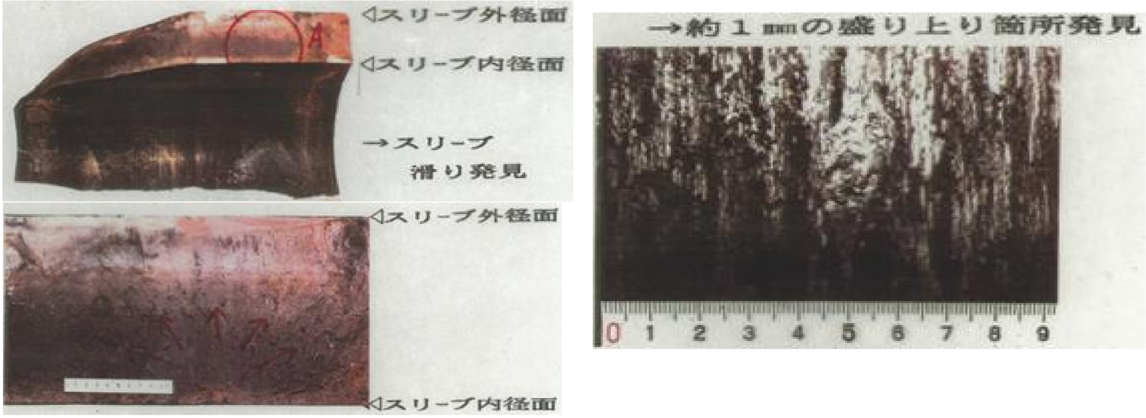

(b) Inner surface and fracture surface

Fig. 1-3 Sleeve breakage

source which will increase the rolling stress. Eventually, the crack will initiate from the inside and moves to the surface, that leads to the sleeve breakage.

In the hot rolling sleeve assembly type, besides the compressive stress on the outer layer of the sleeve and tensile stress generated in the inner layer, shrinkage stress, rolling stress, thermal stress, and rolling torque are added to the roll. Therefore, in the sleeve assembly type roll structure, to prevent circumferential slippage, the resistance torque is designed to be larger than the motor torque. By using this condition, the interfacial slippage on the whole sleeve surface is prevented. However, the circumferential slippage in which the sleeve moves in the opposite direction of the rolling still occurs even though this condition is applied.

A similar phenomenon is known as an interfacial creep in ball bearing attracts attention. The creep phenomenon in rolling bearings has been known for over 60 years. One of the race creeps theories found in the literature justifies the creep phenomenon as the local strain in the contact area [39, 40]. This literature found out that in consequence of the constantly increasing specific loads acting on the rolling bearing, the outer ring creeps resulting from the local deformation of the outer ring caused by the relative movement of the rolling element. Besides that, it is known the creep phenomenon can be regarded as relative slippage as a common phenomenon in rolling bearing [41]. Mainly, two types of slippage are known as the creep phenomenon in the bearing. One is the relative slippage appearing in the same circumferential direction as the bearing rotating direction [42, 43]. The other is the relative slippage appearing in the opposite circumferential direction to the bearing rotating direction [44]. It is also known that one of the relative slippage appearing in the opposite direction is caused by the accumulation of elastic deformation [42]. These movements can lead to fretting corrosion, setting free particles that might cause problems in other places of a bearing. Also, misalignment and ultimately breaking of components can be caused, leading to failures of entire bearing [45]. Many studies have been done to improve the performances of the rolling bearings [43, 46, 47]. However, few studies are available to realize the creep phenomenon in the numerical simulation that is useful for investigating the detail. Although there are some similarities such as the sliding direction, no analytical studies were available discussing the phenomenon quantitatively in ball bearing and rolling roll.

1.4 Motivation and Objectives

Among rolling rolls used in steel industries, instead of a solid roll, sleeve assembly types were tried to be used and some of them were practically and successfully used by shrink-fitting shafts into a hollow cylinder. However, this shrink-fitted structure has several peculiar problems such as residual roll bending and sleeve cracking due to the circumferential sleeve slip. Therefore, it is important to clarify the cause of the sleeve slip phenomenon in a sleeve structure. In this paper, the mechanism of interfacial slip in a sleeve assembly type roll constructed by shrink-fitting is verified by FEM analysis, and to apply it to the actual machine, the roll material, the fitting conditions, and the effect of the rolling load is considered. Finally, the experimental method of a miniature roll is demonstrated to verify the analysis. This paper consists of 7 chapters and is organized as follows.

Chapter 1 introduced the bimetallic work roll and the problems encountered in the sleeve assembly type rolls. Although the shrink-fitting sleeve assembly roll has many advantages compared to the solid roll, it also has unique problems such as residual bending and sleeve slip. Therefore, the necessity to clarify the sleeve slip in the bimetallic work roll is described in this paper.

In Chapter 2, the mechanism of the sleeve slip formation under free rolling for the hot rolling roll is considered. It has been shown that the sleeve slippage, known as an interfacial creep in bearings, is formed from the accumulations of the relative displacements on the shrink-fitted surface. In the actual roll problem, it is necessary to consider not only the sleeve but also the elastic deformation of the shaft, and the relative displacement between sleeve and shaft caused the interfacial slip. Therefore, in this chapter, to get closer to the actual rolling conditions, the effect of elastic deformation of the shaft on the interfacial slip is investigated under the free rolling state with reference to the previous study which the shaft is a rigid body. Furthermore, in addition to the steel shaft, other shaft materials are also considered to clarify the effect of elastic deformation of the shaft material on the interfacial slip.

In Chapter 3, as in the previous chapter, the effect of rolling torque on the interfacial slip is considered for hot rolling rolls. In this chapter, the motor torque with the frictional force from the rolled steel may promote the slippage in the sleeve rolls significantly causing serious failure. Therefore, the motor torque effect will be investigated quantitatively. In this sense, the effects of the shrink-fitting ratio and the friction coefficient which are the parameters of the resistance torque are also considered since they may contribute to slippage resistance. Here, the interface slip and the displacement increase rate are analyzed.

In Chapter 4, the interfacial slip in shrink-fitted roll is confirmed experimentally under free rolling conditions by using a miniature roll. Then, the behavior of the sleeve slip obtained in the experiment is considered and is compared with the numerical analysis results. In addition, the effect of the sleeve inner surface scratches due to the interfacial slip on the sleeve strength is considered. In this chapter, the fatigue risk in terms of the stress concentration factor, Kt of the defect is evaluated.

Chapter 5 focuses on the high-speed steel bimetallic sleeve rolls, which are made by shrink-fitting the composite sleeve and shaft. In this chapter, the inner surface stress of the sleeve caused by the sleeve slippage under the actual rolling conditions is obtained by numerical simulation; then its effect on fatigue fracture is clarified. Here, the damage caused by the sleeve slip is regarded as a defect, and the fatigue limit obtained by considering the root area $\sqrt{area}$ of the defect is used in the durability diagram to evaluate the safety side of the damage in the sleeve roll. In this chapter, the maximum stress, minimum stress, and stress amplitude is clarified.

In Chapter 6, the difference of the residual stress generated between the bimetallic solid roll and the current study of bimetallic sleeve roll constructed by shrink-fitting is studied. Two types of the manufacturing process are considered in this chapter. Method 1 is turning inside of the solid roll after heat treatment. Method 2 is heat treatment after turning inside of the solid roll. The results show that Method 2 is better than Method 1 since the tensile residual stress can be reduced at the inside of the sleeve. After shrink-fitting of the shaft, the residual stress is compared with one of the solid rolls. Then, the evaluation of the fatigue risk in consideration of the residual stress is also studied.

Chapter 7 summarizes the main conclusions of this study.

References for Chapter 1

[1] K. Hori: 70th Grand Lecture Meeting of The Iron and Steel Institute of Japan: Tokyo, Japan, pp.200–202 (1965).
[2] H. Shimoda, S. Onodera, K. Hori: Trans. Japan Soc. Mech. Eng., Vol. 32, pp. 1–7 (1966).
[3] H. Shimoda, S. Onodera, K. Hori: Trans. Japan Soc. Mech. Eng., Vol. 32, pp. 440–446 (1966).
[4] H. Shimoda, S. Onodera, K. Hori: Trans. Japan Soc. Mech. Eng., Vol. 32, pp. 689–694 (1966).
[5] H. Shimoda, S. Onodera, K. Hori: Trans. Japan Soc. Mech. Eng., Vol. 33, 11–18 (1967).
[6] H. Takigawa, K. Hashimoto, G. konno, S. Uchida: CAMP-ISIJ, ISIJ, Tokyo, Vol. 16, No. 1150 (2003).
[7] T. Irie, K. Takaki, I. Tsutsunaga, Y. Sano: Testu-to-Hagane, Vol. 65, No. 293 (1979).
[8] M. Kawai, K. Kitsuki, Y. Nozaki, H. Takeuchi, K. Miura: 66th Grand Lecture Meeting of The Iron and Steel Institute of Japan, Tokyo, Japan, Vol. 1, pp. 1613–1615 (1963).
[9] N.A. Noda, Y. Sano, X. Wang, Y. Nakagawa, W.H. Guan, K. Ono, K. Hu: J. Automot. Eng., Vol. 46, pp. 831–837 (2015).
[10] Z. Zhua, D. Suryadi: Appl. Mech. Mater., Vol. 1, pp. 139–142 (2012).
[11] N.A. Noda, D. Suryadi, S. Kumasaki, Y. Sano, Y. Takase: Eng. Fail. Anal., Vol. 57, pp. 219-235 (2015).
[12] N.A. Noda, Y. Xu, D. Suryadi, Y. Sano, Y. Takase: J. ISIJ Int., Vol. 56, pp. 303–310 (2016).

[13] E. Matsunaga, Y. Sano, S. Nishida: Camp-ISIJ, Vol. 10, pp. 1078 (1997).
[14] S. Harada, N.A. Noda, O. Uehara, M. Nagano: Transactions of the JSME, Vol. 57, No. 539, 173 (1991).
[15] N.A. Noda, Hendra, Y. Takase, M. Tsuyunaru: Jounal of Solid Mechanics and Materials Engineering, Vol. 2, No. 11, pp. 1410-1419 (2008).
[16] Hendra, M. Tsuyunaru, N.A. Noda, Y. Takase: Key Engineering Materials, Vols. 385-387, pp. 513-516 (2008).
[17] W. Li, N.A. Noda, H. Sakai, Y. Higashi: Key Engineering Materials, Vols. 452-453, pp. 241-244 (2011).
[18] N.A. Noda, Y. Yamada, Y. Sano, S. Sugiyama, S. Kobayashi: Engineering Failure Analysis, Vol. 15, No. 4, pp. 261-274 (2008).
[19] N.A. Noda, Hendra, Y. Takase, W. Li: Jounal of Solid Mechanics and Materials Engineering, Vol. 3, No. 10, pp. 1090-1100 (2009).
[20] N.A. Noda, Hendra, Y. Takase, H. Ogura, Y. Higashi: Jounal of Solid Mechanics and Materials Engineering, Vol. 4, No. 8, 1198-1213 (2010).
[21] Y. Takase, W. Li, Hendra, H. Ogura, Y. Higashi, N.A. Noda: Key Engineering Materials, Vols. 452-453, pp. 233-236 (2011).
[22] N.A. Noda, Y. Sano, Y. Takase, W. Li, H. Sakai: International Journal of Engineering Innovation and Management, Vol. 1, pp. 77-82 (2011).
[23] T. Hattori, Y. Kamitani, K. Sugino, H. Tomita, Y. Sano: International Conference on Tribology in Manufacturing Process, 24-26 September 2007, Yokohama.
[24] S. Hamayoshi, E. Ogawa, K. Shimizu, N. Noda, K. Kishi, S. Koga: SOKEIZAI, Vol. 51, No. 12, pp. 54–58 (2010).
[25] Y. Sano, Fatigue failure problem in the inside of roll body for hot strip rolling-Crack initiation problem and its estimation in the actual plant. The 245th JSMS Committee on Fatigue of Materials and The 36th JSMS Committee on Strength Design, Safety Evaluation (1999), 40.
[26] E. Matsunaga, T. Tsuyuki, Y. Sano: Camp-ISIJ, Vol. 11, pp. 362 (1998).
[27] S. Tsutsumi, S. Hara, S. Yoshi: The Residual Deflection of Sleeved Back-up Rolls, Tetsu-to-Hagane, Vol. 57, pp. 818–822 (1971).
[28] S. Spuzic, K.N. Strafford, C. Subramanian, G. Savage: Wear, Vol. 176, No. 2, pp. 261-271 (1994).
[29] N. A. Noda, K. Hu, Y. Sano, K. Ono, Y. Hosokawa: Steel Res. Int., Vol. 87, No. 11, pp. 1478-1488 (2016).
[30] N.A. Noda, Y. Sano, Y. Takase, Y. Shimoda, G. Zhang: J. Jpn. Soc. Technol. Plast., Vol. 58, No. 66 (2017).
[31] K. Hu, Y. Xia, F. Zhu, N.A. Noda: Steel Res. Int., Vol. 89, No. 4, 1700368 (2017).
[32] N.A. Noda, H. Sakai, Y. Sano, Y. Takase, Y. Shimoda: Metals, Vol. 8, No. 998 (2018).
[33] H. Sakai, N.A. Noda, Y. Sano, G. Zhang, Y: TakaseTetsu-to-Hagane, Vol. 105, No. 12, pp. 1126-1134 (2019).
[34] H. Sakai, N.A. Noda, Y. Sano, Y. Takase, G. Zhang: Testu-to-Hagane, Vol. 105, No. 4 (2019).
[35] H. Sakai, N.A. Noda, Y. Sano, G. Zhang, Y. Takase: ISIJ Int., Vol. 59, No. 5, pp. 889-894 (2019).
[36] P. G. Stevens, K.P. Ivens, P. Harper: J.Iron and Steel Inst, Vol. 209, No. 1, pp. 1-11 (1971).
[37] M. Fujii, A. Yoshida, J. Ishimaru, S. Shigemura, K. Tani:. Transaction of the JSME Part C, Vol. 72, No. 716, pp.1354–1360 (2006).
[38] M. Ooshima, Y. Sugimura, and Y. Sano: 32nd Mechanical Working and Steel Processing, Vol. 28, 31–34 (1990).
[39] J. Zhan, H. Takemura, K. Yukawa: A study on bearing creep mechanism with

FEM simulation. Proceedings of IMECE2007, 2007 Seattle, Washington, USA.
[40] J. Zhan, K. Yukawa, H. Takemura: Analysis of bearing outer ring creep with FEM. Advanced Tribology, 2009, Springer, Berlin, Heidelberg.
[41] N. Soda: Bearing. Iwanami Shoten, Tokyo, pp. 196-203 (1964).
[42] T. Niwa: A creep mechanism of rolling bearings. NTN Tech. Rev., Vol. 81, pp. 100-103 (2013).
[43] A. Maiwald, E. Leidich: FE simulations of irreversible relative movements (creeping) in rolling bearing seats –Influential parameters and remedies. World Congress on Engineering and Computer Science 2013 Vol II, San Francisco, USA.
[44] J. Murata, T. Onizuka: Generation mechanism of inner ring creep. Koyo Eng. J., Vol. 166, pp. 41-47 (2005).

2 Interfacial slip in shrink-fitted bimetallic work roll promoted by roll deformation

2.1 Introduction

In metalworking, rolling processes are more tonnage than any other manufacturing process. Rolling technology is developing and advancing further although seemingly mature [1-15]. Fig. 2-1 illustrates the rolling roll in roughing stands of hot rolling stand mills. The rolls are classified into two types; one is a single-solid type, and the other is a shrink-fitted assembled type consisting of a sleeve and a shaft.

Some sleeve rolls are practically and successfully used as the back-up rolls having large trunk diameter exceeding 1000mm and also used as the rolling rolls for large H-section steel [1-3]. Those sleeve rolls have several advantages. The shaft can be reused by replacing the sleeve after consumed due to the abrasion or the surface roughening. Furthermore, the sleeve wear resistance can be improved independently without loosening the shaft ductility.

On the other hand, this shrink-fitted sleeve roll has several peculiar problems such as residual bend deformation, fretting fatigue cracks at the sleeve end and sleeve fracture due to the circumferential sleeve slippage [5-13]. Among them, no detail studies are available for this circumferential slippage in rolling roll. It should be noted that the circumferential slippage sometimes occurs even though the resistance torque at the interface is larger than the motor torque. It is known that this slippage is irreversible since the slippage does not go back to the initial state in a reversible way after removing the load. Since the initial conditions cannot be restored exactly [12-15], this phenomenon is hard to be proved. Considering no quantitative study available for rolling rolls, our previous study assumed a rigid shaft to simplify the phenomenon and to realize the

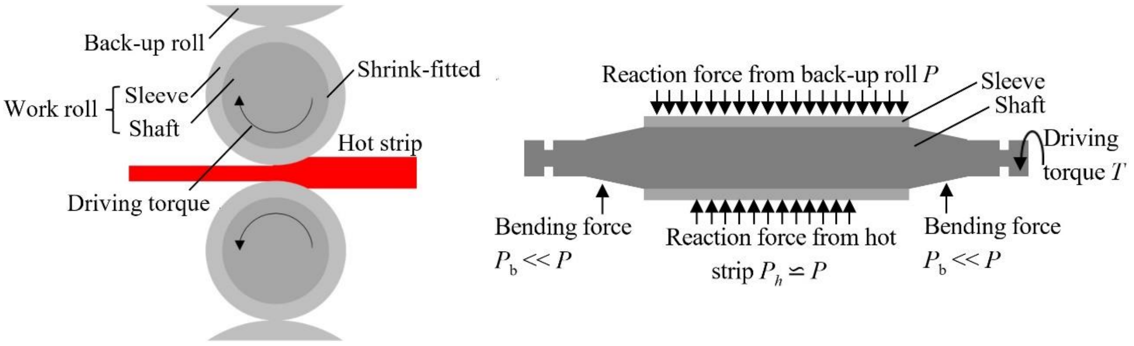

(a) Central cross-section view of rolling roll.

(b) Axial section view of rolling roll.

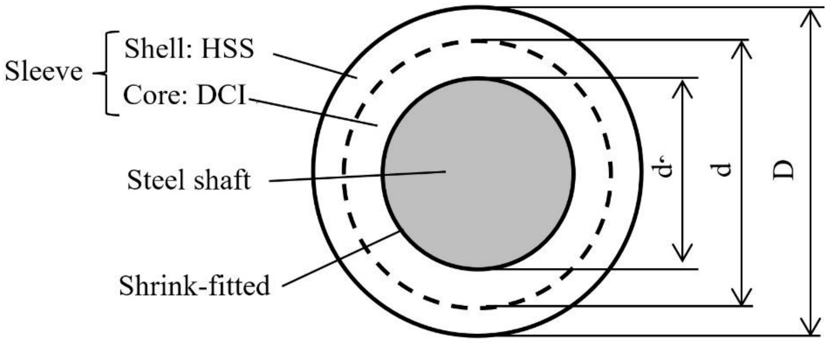

(c) A target of this study: HSS bimetallic roll in central cross-section.

Fig. 2-1 Schematic illustration for real hot strip rolling roll.

slippage in the numerical simulation [12-15]. However, similar phenomenon is known as "interfacial creep" in ball bearing. In this failure, the bearing gradually moves circumferentially to the stationary shaft or housing [16-26]. To explain this failure, Soda [16] explained two factors; one is the clearance between the ring and the shaft or housing, and the other is the elastic deformation which Imai [17] proved experimentally. Those studies treated the interface creep in the opposite direction to the bearing rotation [17, 18] but another reports treated the creep in the same direction [19, 20]. Several other studies are also available for the bearing creep phenomenon [21-28]. However, few studies discussed the phenomenon quantitatively.

In this study, to understand the phenomena essentially, the elastic roll deformation effect will be discussed in the simulation under free rolling. Furthermore, by using miniature rolling facility, the interfacial slip will be verified experimentally. Different from ball bearings, as shown in Fig. 2-1(a), the driving torque and the frictional force may promote the slippage in the sleeve rolls causing serious failure. However, before considering additional factors such as the motor torque, it is necessary to investigate and verify the essence of the phenomena under free rolling like ball bearing creep. By clarifying the phenomenon, in this way, such unknown failure can be prevented in the near future and the sleeve assembly type roll can be used much more widely.

2.2 Interfacial slip simulation focusing on the relative displacement

Fig. 2-1 illustrates a sleeve assembly type roll used in rolling. Fig. 2-1(a) illustrates the central cross-section and Fig. 2-1(b) illustrates the axial cross-section. As shown in Fig. 2-1, the sleeve roll consists of a sleeve and a shaft shrink-fitted. Fig. 2-1(c) shows an example of a commonly used bimetallic sleeve roll manufactured by centrifugal casting method. Here, the outer layer is made of high-speed steel (HSS) having high abrasion resistance and the inner layer is made of ductile casting iron (DCI) having high ductility. In this study a single material sleeve roll is considered instead of the bimetallic roll to simplify the analysis and to clarify the interfacial slip.

As shown in Fig. 2-1(a), the roll is subjected to the contact force P from the back-up roll, the rolling force P_h and the frictional force S from the rolling plate. Since two-dimensional modeling is applied, the external force per unit length should be considered as well as motor torque T. In Fig. 2-1(b), the back-up roll is longer than the width the rolling plate; and therefore, the bending force P_b is acting at the bearing. Here, the rolling force P, the rolling reaction force P_h and

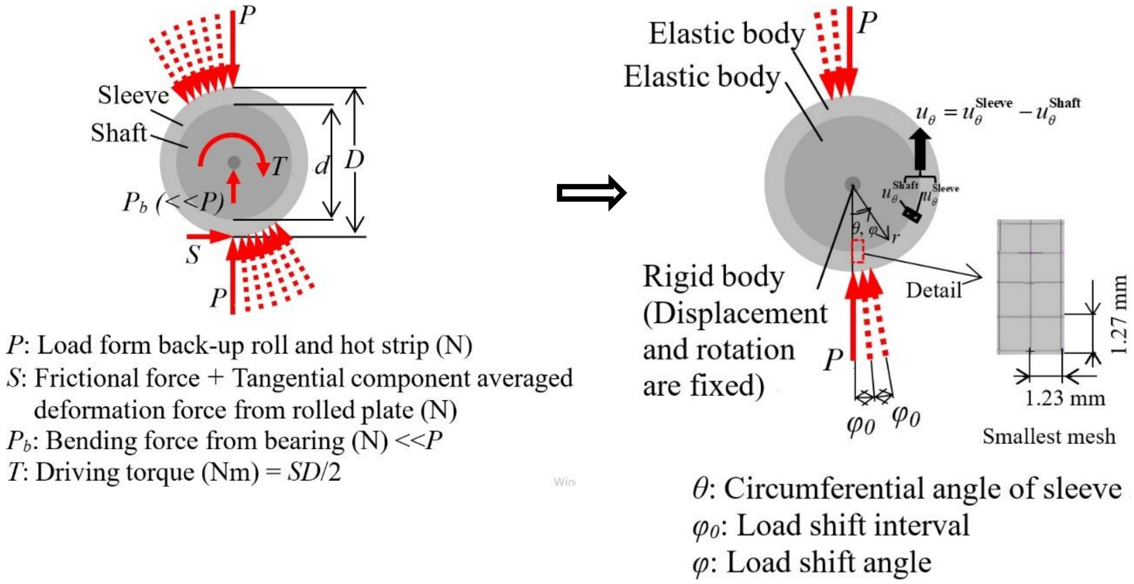

P: Load form back-up roll and hot strip (N)
S: Frictional force + Tangential component averaged deformation force from rolled plate (N)
P_b: Bending force from bearing (N) <<P
T: Driving torque (Nm) = $SD/2$

θ: Circumferential angle of sleeve
φ_0: Load shift interval
φ: Load shift angle

(a) Real roll.

(b) Roll model (T, S, P_b = 0).

Fig. 2-2 Modeling and simulation for interfacial slip.

Table 2-1
Mechanical properties, dimensions and boundary conditions in Fig. 2-2(b) [13-15].

Mechanical properties	Sleeve	Young's modulus of steel sleeve E_{sleeve}	210 GPa
		Poisson's ratio of steel sleeve v	0.28
	Shaft	Young's modulus of elastic shaft E_{shaft}	210 GPa
		Poisson's ratio of steel shaft v	0.28
Roll size		Outer diameter of sleeve	700 mm
		Inner diameter sleeve d	560 mm
Shrink fitting		Shrink fitting ratio δ/d	0.5×10^{-3}
		Friction coefficient between sleeve and shaft μ	0.3
External force		Concentrated load per unit thickness P	13270 N/mm Total: 1.327×10^{7} N Rolled width: 1000 mm
		Frictional force per unit thickness S	0 N/mm
		Motor torque per unit thickness T	0 N/mm
		Bending force from bearing P_b	0 N/mm

the bending force P_b should be balanced, but P_b is estimated to be less than 10% of P and P_h [5]. Therefore, in this study, assume the bending force $P_b = 0$; then, the rolling force (=~P × back-up roll body length) is equal to the rolling force (=~P_h × strip width) as $P \doteq P_h$. This modeling refers to the case study of the loading at the fifth stage of hot finishing roll [5].

Fig. 2-2 illustrates two-dimensional modeling in numerical simulation. As shown in the Appendix A.1 in detail, the roll rotation is expressed by the load shifting on the fixed roll surface [12-15]. Fig. 2-2(a) illustrates the real roll by shifting the load on the roll surface with the roll center fixed. The roll is assumed to be subjected to the concentrated rolling load P = 13270N/mm [4, 5]. In rolling the friction S is used to compress the rolling plate between the rolls. In this study, however, the free rolling with $T = 0$ and $S = 0$ will be discussed as shown in Fig. 2-2(b). This is similar to the ball bearing where the torque is not applied on the ball but either on the inner or outer ring and the balls freely rotates to minimize the friction. Fig. 2-2(b) also shows an example of the mesh division for the finite element method (FEM). To realize the interface slippage, the FEM simulation should be well conducted on basis of the experience and skills for engineering applications. In the previous studies [29-32], the FEM mesh error was discussed for bonded problems and mesh-independent technique was proposed confirming that the displacement boundary condition applied confirming that the displacement boundary condition is relatively insensitive. Contact status change was clarified when the pitch-difference nut is tightened [33] and dynamic deformation was investigated through consecutive quasi-static analyses [34]. On the basis of those skills, during the ceramic roll rotation, the axial movement of the shaft was analyzed by shifting the load on the fixed shaft [35-38]. In this study, the circumferential sleeve slippage will be realized by extending the above technique and applying FEM code Marc/Mentat 2012 to the elastic contact quasi-static analysis for rolling rolls. In this code, the complete Newton-Raphson method and the direct constraint method for the contact analysis are used. As shown in Fig. 2-2(b), a 4-node quadrilateral plane strain is used with the number of mesh elements are 309,440 with confirming the mesh independency of the results [39].

Table 2-1 shows mechanical properties, dimensions and boundary conditions of the model in Fig. 2-2(b). The loading condition used in this study is based on the data at No. 5 stand for roll hot strip finishing roll mill [4, 5]. Assume the concentrated loading P from the back-up roll and the reaction P from the strip with P = 13270N/mm [4, 5]. Small effect can be confirmed by replacing Hertzian contact stress with the concentrated force P. The shrink-fitting ratio is defined as δ/d, where δ is the diameter difference between the inner diameter of the sleeve and the outer diameter of the shaft. Usually, the shrink-fitting ratio in the range $\delta/d=0.4\times10^{-3} \sim 1.0\times10^{-3}$ is applied to sleeve rolls on the basis of long year experience. This is because a smaller value $\delta/d<0.4\times10^{-3}$ may cause interface slip easily and a larger value $\delta/d>1.0\times10^{-3}$ may increase the risk of sleeve fracture [6]. To study the irreversible interfacial slip, in this paper, $\delta/d = 0.5\times10^{-3}$ is focused. The effect of the shrink-fitting ratio is discussed in Section 3.4.2 . Regarding the friction coefficient μ controlling the slippage resistance on the interface, μ = 0.2 was used in an experimental study and μ = 0.4 was often used for steel surfaces previously [1, 40]. In this way, since μ = 0.2~0.4 is usually used for sleeve assembly type rolls, in this study, the friction coefficient μ = 0.3 between the sleeve and the shaft is used.

2.3 Irreversible relative displacement causing interfacial slip

The relative displacement accumulation between the sleeve and shaft may represent the interfacial slip. In Fig. 2-3(a), the relative displacement $u_\theta^{P(0)\sim P(\varphi)}(\theta)$ due to the load shifting $P(0)\sim P(\varphi)$ is defined between the sleeve and shaft when the load moves from the angle $\varphi = 0$ to $\varphi = \varphi$. Here, notation φ denotes the angle where the load is shifting and notation θ denotes the position

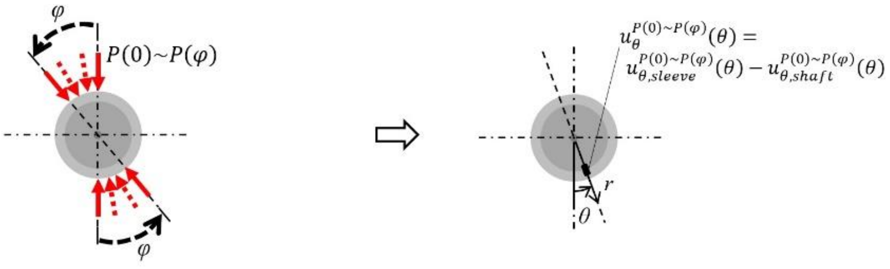

(i) Define the pair of the loads shift from $\varphi = 0$ to φ, and $\varphi = \pi$ to $(\pi + \varphi)$ as $P(0)\sim P(\varphi)$.

(ii) Define the displacement $u_\theta(\theta)$ due to $P(0)\sim P(\varphi)$ as $u_\theta^{P(0)\sim P(\varphi)}(\theta)$.

(a) Definition of interfacial displacement $u_\theta^{P(0)\sim P(\varphi)}(\theta)$ due to the load shifting $P(0)\sim P(\varphi)$.

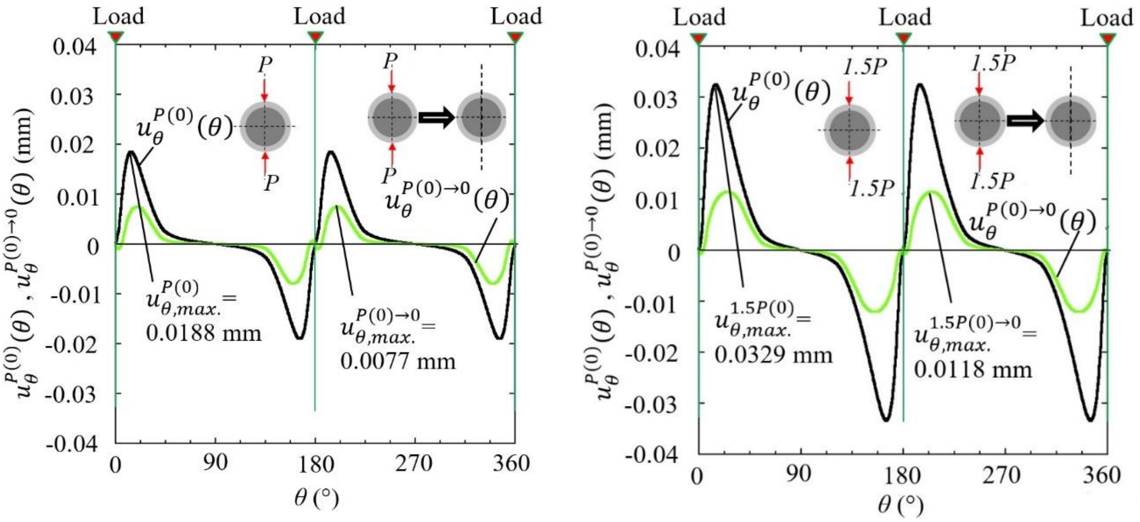

(b) Interfacial displacement $u_\theta^{P(0)}(\theta)$ due to the initial load $P(0)$=P and irreversible interfacial displacement $u_\theta^{P(0)\to 0}(\theta)$ after removing the initial load $P(0)$ as $P(0)$→0 when E_{shaft} =E_{sleeve}= 210GPa.

(c) Interfacial displacement $u_\theta^{P(0)}(\theta)$ due to the initial load $P(0)$=1.5P and irreversible interfacial displacement $u_\theta^{P(0)\to 0}(\theta)$ after removing the initial load $P(0)$ =1.5P as $P(0)$→0 when E_{shaft} = E_{sleeve}= 210GPa.

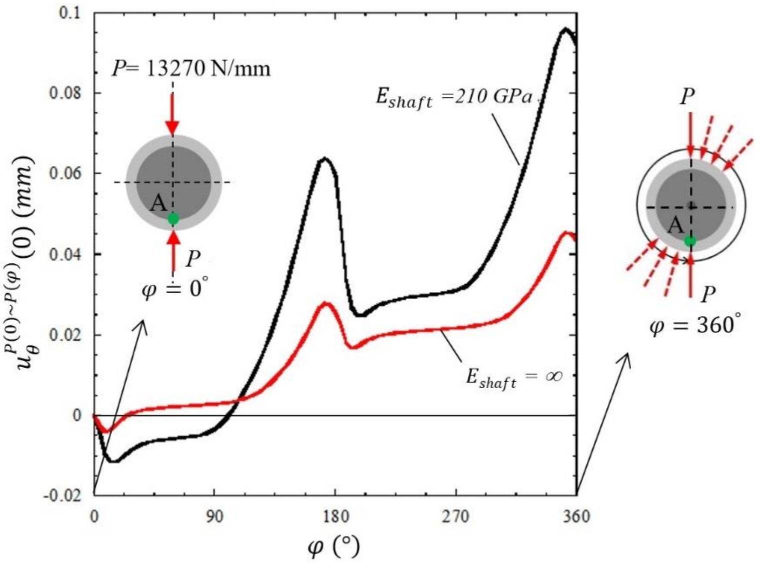

(d) Interfacial displacement $u_\theta^{P(0)\sim P(\varphi)}(0)$ due to the load shifting $P(0)$= P from from $\varphi = 0$ to $\varphi = \varphi$ when E_{shaft} = E_{sleeve}= 210GPa and when E_{shaft} =∞ and E_{sleeve}= 210GPa.

Fig. 2-3 Interfacial displacement and irreversible interfacial displacement.

where the displacement is evaluated. The load $P(\varphi)$ is defined as the pair of forces acting at $\varphi = \varphi$ and $\varphi = \varphi + \pi$. The notation $u_\theta^{P(0)\sim P(\varphi)}(\theta)$ means the relative displacement $u_\theta(\theta)$ at $\theta = \theta$ when the pair of loads are applied at $\varphi = 0$ to $\varphi = \varphi$ and $\varphi = \pi$ to $\varphi = \varphi + \pi$.

Fig. 2-3(b) illustrates an example of the interfacial displacement $u_\theta^{P(0)}(\theta)$ due to an initial load $P(0)$ when $E_{shaft} = E_{sleeve}$ =210GPa. Fig. 2-3(b) also indicates the displacement $u_\theta^{P(0)\to 0}(\theta)$, which is the residual displacement when the initial load $P(0)$ is removed as $P(0) \to 0$. As shown in Fig. 2-3, $u_\theta^{P(0)\to 0}(\theta)$ are not zero as well as $u_\theta^{P(0)}(\theta)$. This non-zero $u_\theta^{P(0)\to 0}(\theta)$ means the displacement $u_\theta^{P(0)}(\theta)$ and $u_\theta^{P(0)\sim P(\varphi)}(\theta)$ is irreversible. Fig. 2-3(c) shows $u_\theta^{P(0)}(\theta)$ and $u_\theta^{P(0)\to 0}(\theta)$ when the larger load $P(0) = 1.5P$ is applied and removed as $P(0) \to 0$. The maximum value of the slip $u_\theta^{P(0)}(\theta)$ increases from 0.0329/0.0188≈1.75, which is larger than 1.5. This non-linearity is caused by contact status change although the displacement is elastic. The maximum value of the irreversible slip $u_{\theta}^{P(0)\to 0}(\theta)$ increases from 0.0118/0.0077≈1.53, which is also larger than 1.5. Fig. 2-3(b) and 2-3(c) illustrate the irreversible displacement $u_{\theta}^{P(0)\to 0}(\theta)$ in a fundamental way by removing the initial load completely. During the roll rotation that can be expressed as the load shifting, such irreversible displacement is accumulated and appears in a complicated way.

When the load is shifted from $\varphi = 0$ to $\varphi = 2\pi$, Fig. 2-3(d) illustrates the relative displacement $u_{\theta}^{P(0)\sim P(\varphi)}(0)$ at $\theta = 0$. As shown in Fig. 2-3(b), under the initial load $u_{\theta}^{P(0)}(0) = 0$. Due to the irreversible slip, $u_{\theta}^{P(0)\sim P(\varphi)}(0)$ becomes negative as $u_{\theta}^{P(0)\sim P(\varphi)}(0) < 0$ in the range $0 < \varphi \leq 96^{\circ}$ and becomes positive $u_{\theta}^{P(0)\sim P(\varphi)}(0) \geq 0$ in the range $\varphi > 96^{\circ}$ when E_{shaft} = E_{sleeve}= 210GPa. Since the slip varies depending on θ, the variations are indicated in Appendix A.1 for half rotation as $u_{\theta}^{P(0)\sim P(\pi)}(\theta)$ and for one rotation as $u_{\theta}^{P(0)\sim P(2\pi)}(\theta)$ in the range $\theta =$ $0\sim 2\pi$. To express the amount of the slip with increasing φ, the average displacement can be defined by the following equation.

$$u_{\theta,ave.}^{P(0)\sim P(\varphi)} = \frac{1}{2\pi}\int_{0}^{2\pi} u_{\theta}^{P(0)\sim P(\varphi)}(\theta)\, d\theta \qquad (2-1)$$

As shown in Fig. 2-3, when the initial load P is applied at $\varphi = 0$, the average displacement is zero as $u_{\theta,ave.}^{P(0)} = 0$. Also, when the initial load is removed as $P(0) \to 0$ the average displacement is zero as $u_{\theta,ave.}^{P(0)\to 0} = 0$. It should be noted that the displacements themselves $u_{\theta}^{P(0)}(\theta)$ and $u_{\theta}^{P(0)\to 0}(\theta)$ are not zero except at θ= 0, π, and 2π. This non-zero displacement means once the load is applied, such local slippage may appear. Although $u_{\theta}^{P(0)}(\theta)$ is symmetric as shown in Fig. 2-3(b), with increasing the load shifting angle φ, the average displacement $u_{\theta,ave.}^{P(0)\sim P(\varphi)}$ increases after losing the symmetry (see Fig. A-2 in Appendix A.1).

Fig. 2-4 illustrates the average displacement $u_{\theta,ave.}^{P(0)\sim P(\varphi)}$ by varying Young's modulus of the shaft, E_{shaft}. As indicated in Fig. 2-4 and Table 2-2,

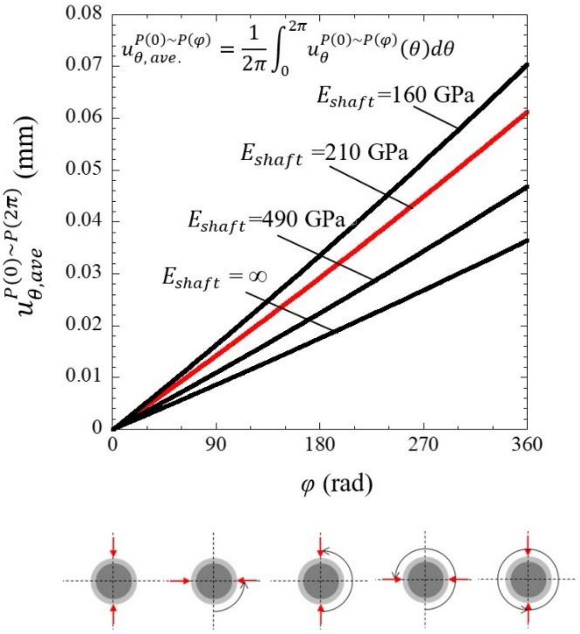

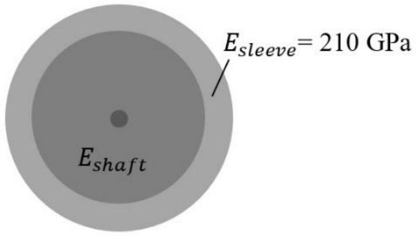

Table 2-2
Shaft Young's modulus E_{shaft} and shrink- fitting stress $\sigma_{r_{shrink}}$ when δ/d = 0.5× 10^{-3}

Material	Shaft Young's modulus E_{shaft} [GPa]	$\sigma_{r_{shrink}}$[MPa] (Normalized when E_{shaft} = 210 GPa)
DCI	160	19.42(0.967)
Steel	210	20.09(1.000)
Cermet	490	21.43(1.067)
Rigid	∞	22.57(1.123)

Fig. 2-4 Average displacement $u_{\theta,\ ave.}^{P(0)\sim P(2\pi)}(\theta)$ increases almost linearly with increasing load shift angle ϕ.

assumed shaft materials are ductile cast iron (DCI), steel, cermet and rigid. Table 2-2 also indicates the shrink-fitting stress $\sigma_{r_{shrink}}$ by varying E_{shaft}. The average displacement $u_{\theta,ave.}^{P(0)\sim P(\varphi)}$ increases with increasing the load shift angle φ. With decreasing E_{shaft}, the shrink-fitting stress $\sigma_{r_{shrink}}$ decreases slightly as shown in Table 2-2. It should be noted that the average displacement $u_{\theta,ave.}^{P(0)\sim P(\varphi)}$ is accelerated more significantly with decreasing E_{shaft}. The interface slip may occur as soon as the load shifting starts. It should be noted that the amount of interfacial slip $u_{\theta,ave.}^{P(0)\sim P(\varphi)}$ increases almost linearly with increasing the load shift angle φ as shown in Fig. 2-4. In the following, therefore, the load shift $P(0)\sim P(2\pi)$ which represents one rotation load will be considered to discuss the interfacial slip since the results under many rotations can be linearly estimated.

Fig. 2-5 illustrates the average displacement $u_{\theta,ave.}^{P(0)\sim P(2\pi)}$ due to the load shifting $P(0)\sim P(2\pi)$ versus the shaft Young's modulus E_{shaft}. The average displacement for ductile iron (DCI) is larger compared to steel, cermet and rigid

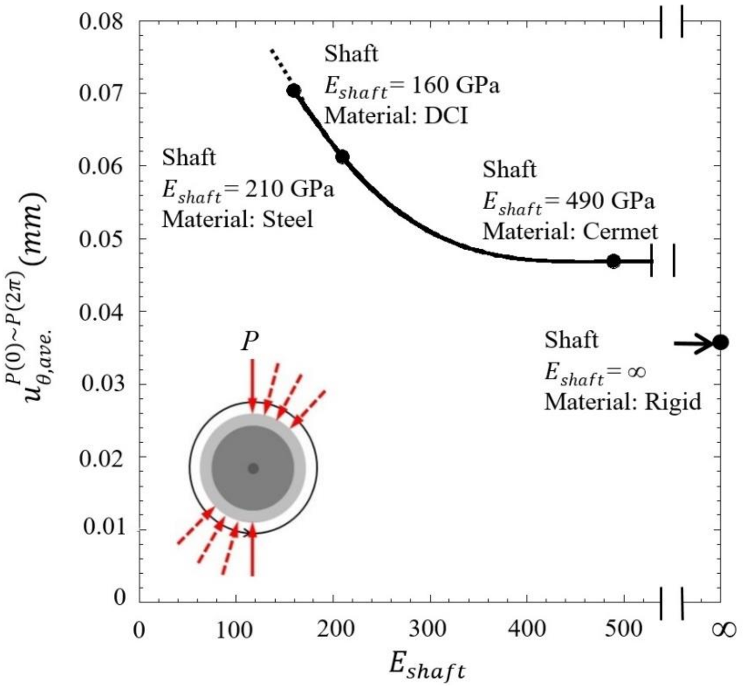

Fig. 2-5 Average displacement $u_{\theta,ave.}^{P(0)\sim P(2\pi)}$ versus E_{shaft} when E_{sleeve}= 210 GPa.

shaft. It may be concluded that the shaft elastic deformation contributes to the interfacial slip. In the following section, the effect of the shaft materials to the interfacial slip will be discussed in detail. The relation between $u_{\theta,ave.}^{P(0)\sim P(2\pi)}$ and E_{shaft} in Fig. 2-5 should be compared with other relations to find out the controlling parameter of $u_{\theta,ave.}^{P(0)\sim P(2\pi)}$ (see Fig. 2-7, Fig. 2-8, Fig. 2-10).

2.4 Discussion of shaft elastic deformation on interfacial slip

Fig. 2-6 shows the shear stress distribution $\tau_{r\theta}^{P(0)\sim P(2\pi)}$ in comparison with the frictional stress $\mu\sigma_r^{P(0)\sim P(2\pi)}$ along the shrink-fitting surface. Fig. 2-6(a) shows the rigid shaft result under the load shifting $P(0)\sim P(2\pi)$. Fig. 2-6(b) shows the elastic shaft result when E_{shaft}=210GPa under the load shifting $P(0)\sim P(2\pi)$. The notation $P(0)\sim P(2\pi)$ denotes one rotation loading from $\varphi = 0$ to $\varphi = 2\pi$. It should be noted that the displacement increases with increasing φ as shown in Fig. 2-4 but the stresses σ_θ does not change with increasing φ [13].

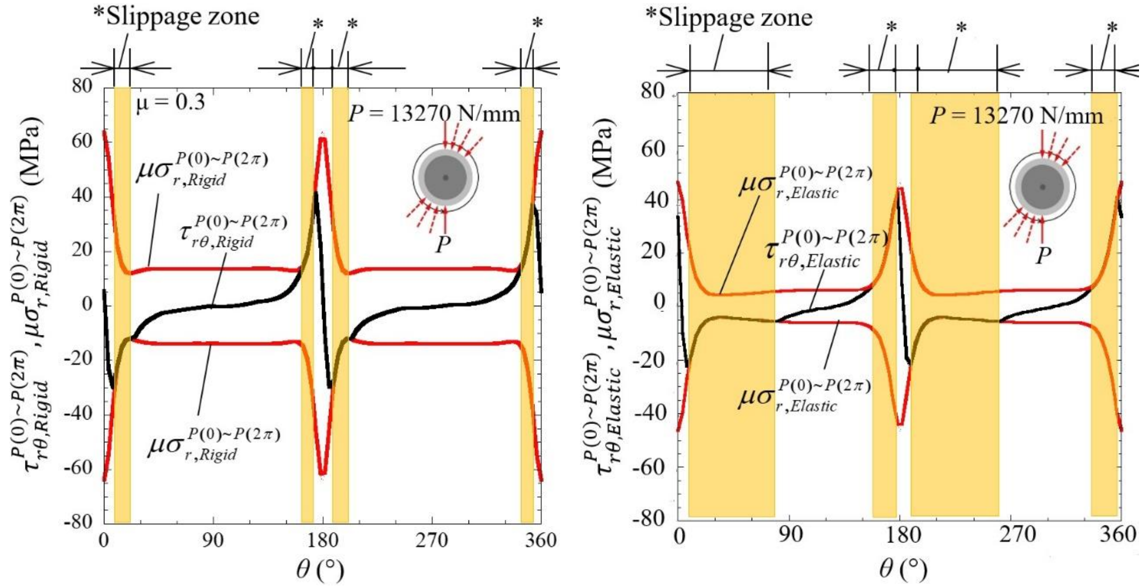

(a) Rigid shaft under the load shifting $P(0)\sim P(2\pi)$.

(b) Elastic shaft when E_{shaft}= 210 GPa under the load shifting $P(0)\sim P(2\pi)$.

Fig. 2-6 Comparison of slippage zone of rigid shaft and elastic shaft under the load shifting $P(0)\sim P(2\pi)$.

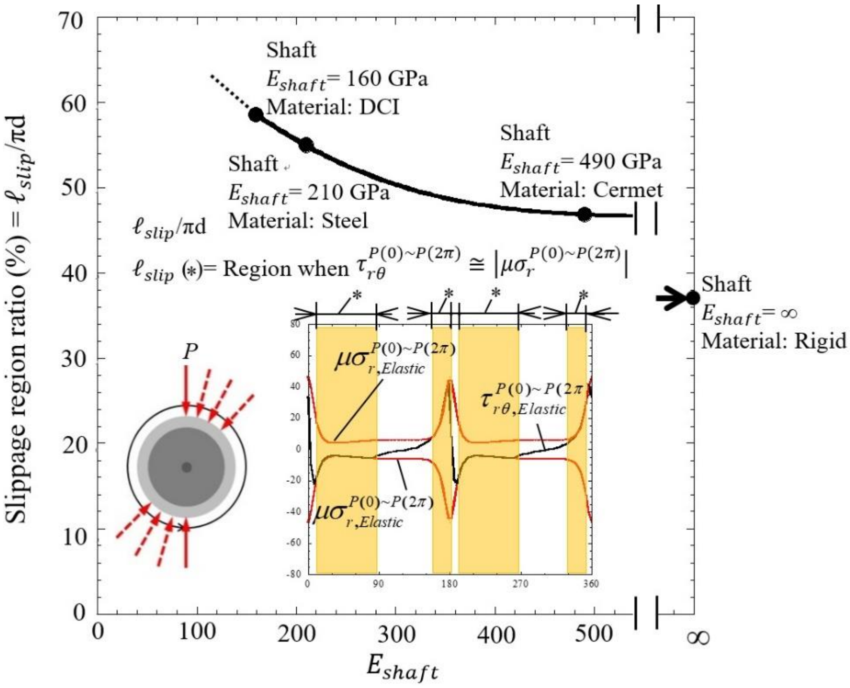

Fig. 2-7 Slippage range ratio ℓ_{slip}/πd versus E_{shaft} when E_{sleeve}= 210 GPa.

In this study, the friction coefficient $\mu = 0.3$ is assumed between the sleeve and the shaft. By considering the FEM accuracy, the irreversible relative displacement may appear when $\tau_{r\theta} \cong |\mu\sigma_r|$ within the error ±1MPa. This region can be defined as the slippage region ℓ_{slip}. In the previous study by Noda et. al. [12], the region was named "quasi-equilibrium stress zone $\tau_{r\theta} \cong |\mu\sigma_r|$" where the irreversible displacement occurs. As shown in Figs. 2-6(a) and 2-6(b), the slippage region ℓ_{slip} is much larger for the elastic shaft compared to the rigid shaft. This behaviour explained the larger irreversible displacement appears as shown in Fig. 2-5.

Fig. 2-7 shows the slippage region ratio that is defined as $\ell_{slip}/\pi d$ due to the load shifting $P(0){\sim}P(2\pi)$. Here the slippage region ℓ_{slip} is where $\tau_{r\theta}^{P(0)\sim P(2\pi)} \cong \left|\mu\sigma_r^{P(0)\sim P(2\pi)}\right|$.

$$\text{Slippage region ratio } = \ell_{slip}/\pi d$$

$$\ell_{slip} = \text{ Region where } \tau_{r\theta}^{P(0)\sim P(2\pi)} \cong \mu\sigma_r^{P(0)\sim P(2\pi)} \qquad (2-2)$$

As shown in Fig. 2-7, the slippage region ratio $\ell_{slip}/\pi d$ decreases with increasing E_{shaft}. As shown in Fig. 2-5, the average displacement $u_{\theta,ave.}^{P(0)\sim P(2\pi)}$also decreases with increasing $E_{shaft.}$ In this way, the interfacial displacement may be promoted by larger elastic deformation due to smaller E_{shaft}. Therefore, the reason why $\ell_{slip}/\pi d$ decreases with increasing E_{shaft} is discussed in this section.

First, as a typical elastic deformation, the diameter increase in the lateral direction Δd is focused. Fig. 2-8 shows the lateral diameter increment $\Delta d^{P(0)\sim P(2\pi)}$ after the one cycle loading $P(0){\sim}P(2\pi)$ when the final loads are applied in the vertical direction at $\theta = 0°$ and $\theta = 180°$. With increasing E_{shaft}, the lateral diameter increment $\Delta d^{P(0)\sim P(2\pi)}$ decreases and goes to zero. Figs. 2-7 and 2-8 show the same trend although in Fig. 2-8 $\Delta d \rightarrow 0$ when $E_{shaft} \rightarrow \infty$. It can be concluded that the interfacial slip can be accelerated by the larger elastic shaft

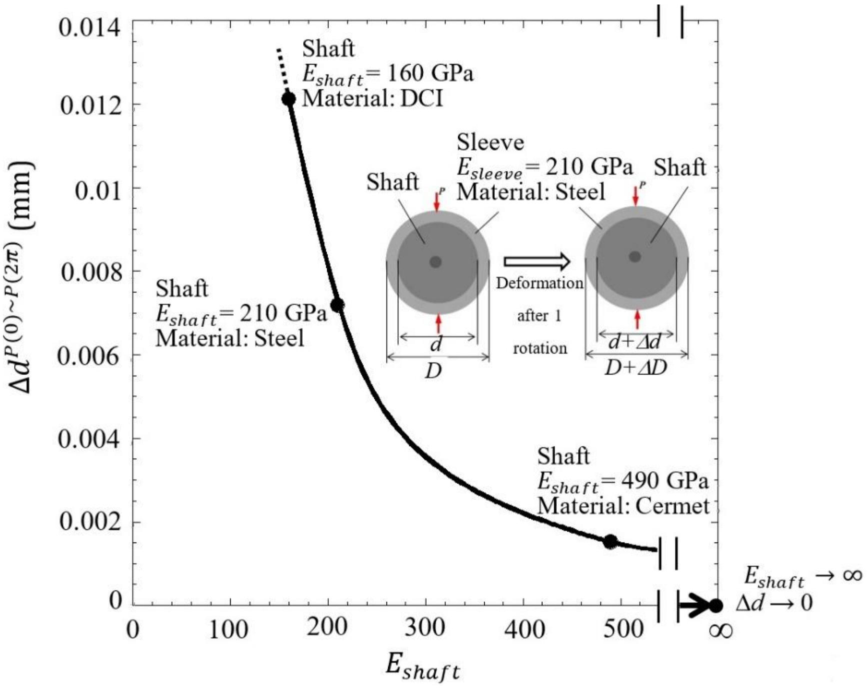

Fig. 2-8 Shaft diameter increment $\Delta d^{P(0)\sim P(2\pi)}$ versus E_{shaft} when E_{sleeve}= 210 GPa.

deformation due to smaller E_{shaft}.

Next, the contact stress change due to the external loading is focused. Fig. 2-9 illustrates the contact stress $\sigma_r^{P(0)\sim P(2\pi)}$ along the interface due to the load shifting $P(0)\sim P(2\pi)$. As shown in Fig. 2-9, there is the region ℓ_{small} where the contact stress $\sigma_r^{P(0)\sim P(2\pi)}$ becomes smaller than the original shrink-fitted stress $\sigma_{r_{shrink}}$ as $\sigma_r^{P(0)\sim P(2\pi)} \leqq \sigma_{r_{shrink}}$. Here, $\sigma_{r_{shrink}}$ denotes the shrink-fitting stress without applying the load P when $E_{shaft} = E_{sleeve} = 210\text{GPa}$. The region ℓ_{small} can be named "the smaller contact stress region" where $\sigma_r^{P(0)\sim P(2\pi)} \leqq \sigma_{r_{shrink}}$. In Fig. 2-9, the length of the smaller contact stress region ℓ_{small} is express as $\ell_{small} = \theta_{small} \times d/2$ by using the angle θ_{small} as described in Fig. 2-10. As shown in Fig. 2-9, the DCI shaft has a larger ℓ_{small} followed by steel and cermet shaft, while rigid shaft has a smallest ℓ_{small}.

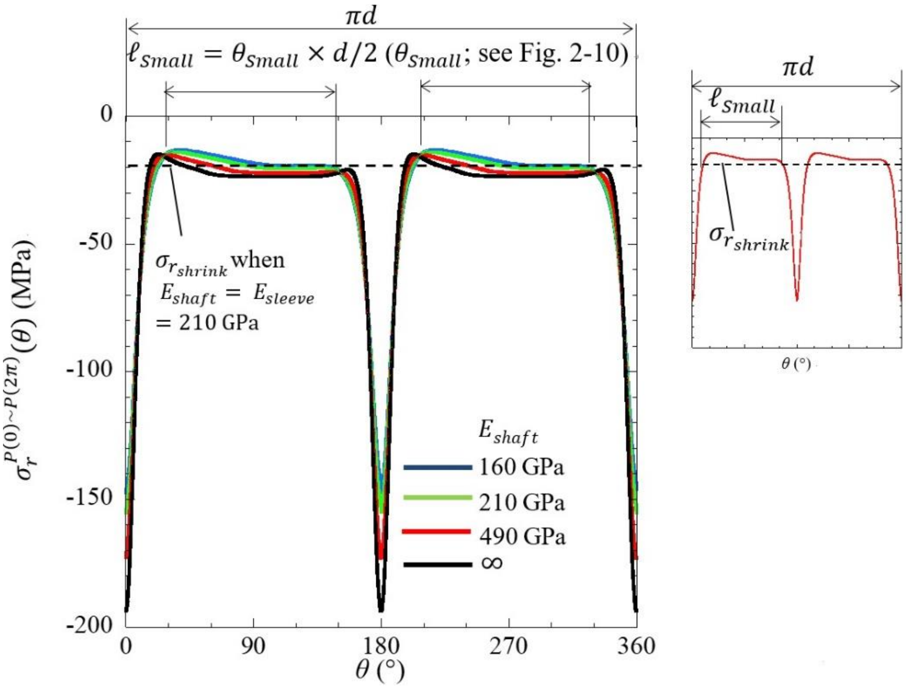

Fig. 2-9 Definition of smaller contact stress region ℓ_{small} where $\sigma_r^{P(0)\sim P(2\pi)} \leqq \sigma_{r_{shrink}}$.

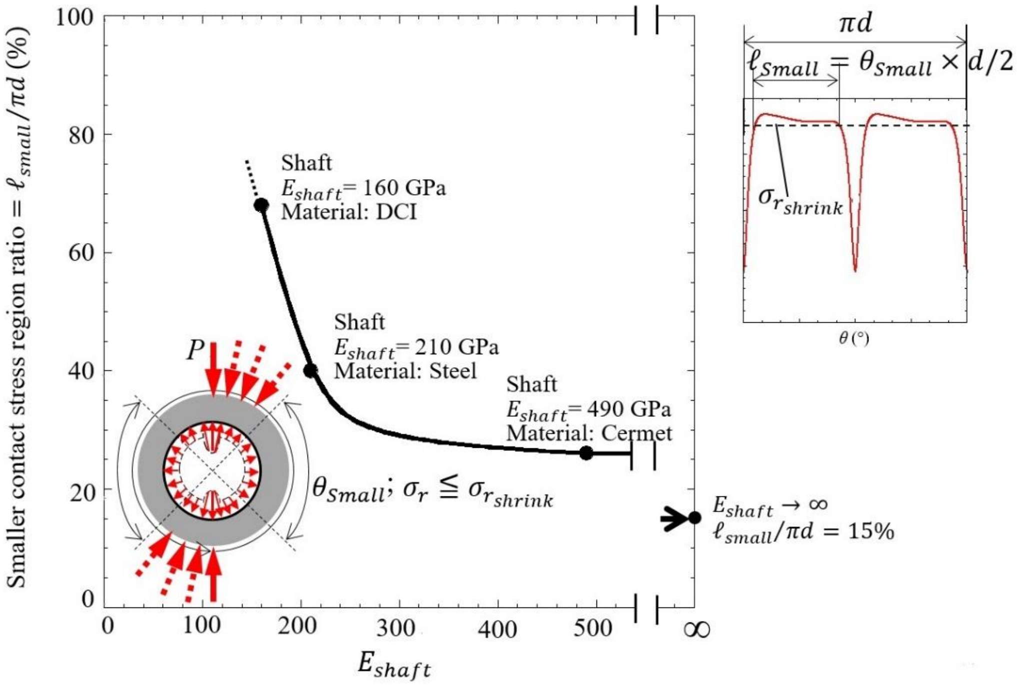

Fig. 2-10 Smaller contact stress region ratio $\ell_{small}/\pi d$ versus E_{shaft} when E_{sleeve}= 210 GPa.

Fig. 2-10 shows the smaller contact stress region ratio $\ell_{small}/\pi d$ normalized by the total circumferential length πd by varying E_{shaft}. The smaller contact stress region ratio is given by the following equation.

Smaller contact stress region ratio $= \ell_{small}/\pi d$,

ℓ_{small} =Region where $\sigma_r^{P(0)\sim P(2\pi)} \leqq \sigma_{r_{shrink}}$ when $E_{shaft} = E_{sleeve} = 210GPa$ (2-3)

The ratio $\ell_{small}/\pi d$ increases with decreasing E_{shaft}. Similar trend can be seen for $\ell_{slip}/\pi d$ in Fig. 2-7. With increasing the smaller contact stress region, the slippage may happen easily. It can be concluded that the slippage region ℓ_{slip} is closely related to the smaller contact stress region ℓ_{small}.

In this paper, under fixed E_{sleeve}=210GPa, the interfacial slip is discussed by varying E_{shaft} as shown in Table 2-2. One may think that E_{shaft} assumed in Figs. 2-4 – 2-10 is not very realistic; and instead, larger E_{sleeve} such as ceramics sleeve should be discussed to reduce the surface wear. In this paper, however, to develop the bimetallic sleeve roll in Fig. 2-1(c), the effect of the shaft elastic deformation on the interface slippage is focused to clarify the phenomena. After understanding the essential phenomena in this way, the interface slippage will be prevented.

2.5 Experimental confirmation for interfacial slip by using miniature roll under free rolling

In this paper, the effect of the motor torque on the interfacial slip is mainly investigated through numerical simulation. To verify the simulation experimentally, Fig. 2-11 illustrates the miniature roll specimen whose diameter is 60 mm used to confirm the interfacial slip [14]. Table 2-3 shows the experimental conditions with no motor torque because a similar phenomenon known as “interfacial creep” in ball bearing was under free rolling. The work roll

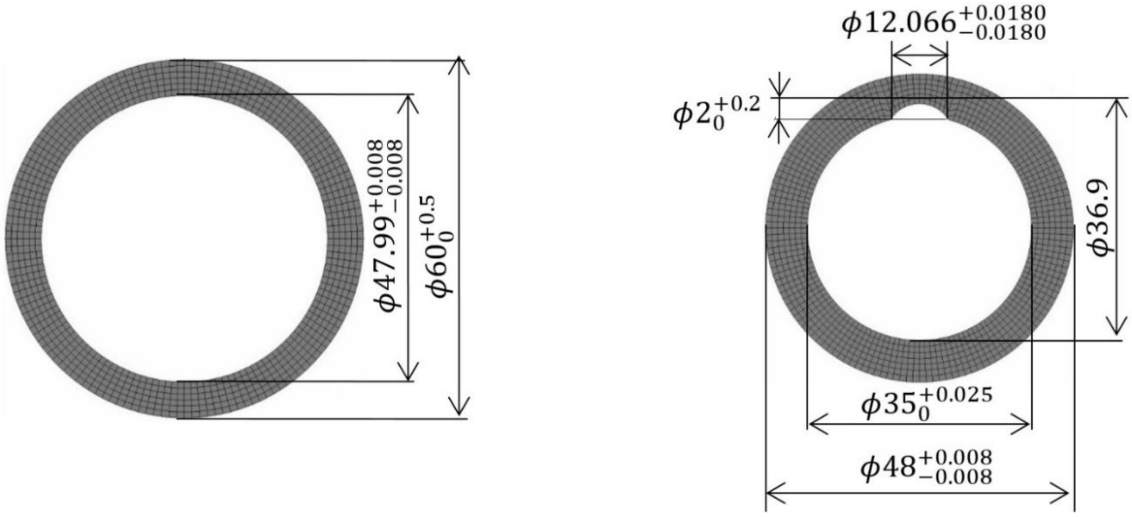

(a) Sleeve 1 (b) Sleeve 2

Fig. 2-11 FEM mesh for test specimen used in a miniature roll.

Table 2-3

Experimental conditions by using a miniature roll in Fig. 2-11.

Test roll	
Shrink-fitting ratio $\delta/d = 0.21\times10^{-3}$	
Driving condition	
Test roll	Free rolling.
Pair roll	Driven by the torque 457Nm.
Load P (ton)	1.0
Rotating speed (rpm)	106~212
Roll cooling: Front side (L/min), Back side	Water 0.25, 2.0
Roll temperature (℃): $\delta/d=0.21\times10^{-3}$, 0	16.0～21.0
Number of rotation n	Rotations until sleeve slip

consists of two sleeves and a shaft. To realize the slip between sleeve 1 and sleeve 2 in Fig. 2-11, sleeve 2 and the inserted shaft are fixed by the key. In the experiment, the work roll was cooled down by water at room temperature to prevent the change of the shrink-fitting ratio due to rising temperature. Under the steady rotation, the load of 1 ton was applied confirming the roll surface

Table 2-4
Comparison of experimental data and simulation results for average displacement during one roll rotation

Shrink-fitting ratio δ/d = 0.21×10^{-3}			
	Experimental results for miniature roll in Fig. 2-11	Simulation results for miniature roll in Fig. 2-11	Simulation results for real roll in Fig. 2-1
$u_{\theta,ave.}^{P(0)\sim P(2\pi)}$	0.108×10^{-2} mm	0.384×10^{-2} mm	2.92×10^{-2} mm

temperature change was within 5 ° C or less during the experiment by a contact thermometer.

The FEM simulation is also performed by using the mesh in Fig. 2-11. Four-node quadrilateral plane strain elements are used, and the total number of mesh elements is 7408. By assuming the loading P = 245 N/mm, the shrink-fitting ratio δ/d = 0.21×10^{-3} and the constant friction coefficient μ = 0.3 between sleeve 1 and sleeve 2, the numerical simulation is newly performed for the miniature roll. Similar to Fig. 2-3, $u_{\theta}^{P(0)\sim P(\varphi)}(\theta)$ is defined as the relative displacement between sleeve 1 and sleeve 2.

Table 2-4 summarizes the average values of the displacement obtained by the simulation in comparison with the slip distance in the experiment when δ/d = 0.21×10^{-3}. The experimental value corresponds to $u_{\theta,ave.}^{P(0)\sim P(2\pi)}$ during one roll rotation that can be calculated in the following way.

$$\begin{aligned} u_{\theta,ave.}^{P(0)\sim P(2\pi)} &= \frac{\theta_{slip}\times\pi d}{360°\times n} \\ &= \frac{77°\times\pi\times 48\,mm}{360°\times 3\times 10^4} \qquad (2-4) \\ &= \frac{32\,mm}{3\times 10^4} \\ &= 0.108\times 10^{-2} mm \end{aligned}$$

In Eq. (2-4), θ_{slip} is the slip angle observed in the experiment, d is the inner diameter of sleeve 1 and n is the number of the roll rotation.

As shown in Table 2-4, although the numerical simulation result is 3.56 times larger than the experimental result, their orders are in agreement. The difference can be explained by the experimental observation. Due to the circumferential slip, slip defects start with thin and shallow scratches, then, it becomes thicker and deeper with erosive wear and cohesive wear, and eventually form large defects that completely stop the slip. In the simulation, a constant friction coefficient μ= 0.3 should be changed to μ =0.3～∞, but actually the change reflecting the real defect evolution is almost impossible in practice. This is the reason why 3.56 times difference appears between the experiment and the simulation. Although the experimental and simulation results are not in good agreement, the model is useful for understanding the phenomenon especially when this is no slip defect, and the model can be used for comparative purposes or similar claims.

2.6 Conclusions for Chapter 2

Shrink-fitted sleeve rolls have several advantages in rolling although interfacial slip sometimes appears and causes the roll damage. Since there were no detail studies are available, in this study, numerical and experimental simulations were performed to clarify the phenomenon of the irreversible relative displacement. Under free rolling condition that is similar to ball bearing, the effect of roll deformation on the circumferential slippage was discussed. The irreversible relative displacement was focused, which is corresponding to the interfacial slip in ball bearing. The conclusions can be summarized as follows:

1. In the numerical simulation, the irreversible relative displacement was confirmed by removing the external load. The accumulation of the irreversible relative displacement $u_{\theta,ave.}^{P(0)\sim P(2\pi)}$ due to the rotation force can be regarded as the slip per rotation since the order of the experiment agrees with the simulation results.
2. The interfacial displacement is promoted by the roll deformation since $u_{\theta,ave.}^{P(0)\sim P(\varphi)}$ increases with decreasing the shaft Young's modulus E_{shaft} as shown in Fig. 2-5. The effect of E_{shaft} on the irreversible relative displacement is related to the interface slippage region size ℓ_{slip} as shown in Fig. 2-7.
3. The interface slippage region ℓ_{slip} can be explained from the smaller contact stress region ℓ_{small} as shown in Fig. 2-9. This is because as the smaller contact stress region size ℓ_{small} becomes larger, the slippage may occur easily. The smaller stress region increases with decreasing shaft Young's modulus E_{shaft} as shown in Fig. 2-10.

In this study, the interfacial slip was confirmed under free rolling condition. It is crucial to understand that the interfacial slip appears due to the elastic roll deformation even under no driving torque. By clarifying the phenomenon in this way, such unknown failure can be prevented, and the sleeve assembly type roll can be use much more widely, the authors believe.

References for Chapter 2

[1] H. Shimoda, S. Onodera, K. Hori: Trans. Jpn. Soc. Mech. Eng., Vol. 32, pp. 689-694 (1966).
[2] T. Irie, K. Takaki, I. Tsutsunaga, Y. Sano: Tetsu-to-Hagane, Vol. 65, 293 (1979).
[3] H. Takigawa, K. Hashimoto, G. Konno, S. Uchida: CAMP-ISIJ, Vol. 16 1150-1153 (2003).
[4] Y. Sano, Recent advances in rolling rolls. Proc of the No. 148-149 Nishiyama Memorial Technology Course, Tokyo, Japan, 193-226 (1993).
[5] Y. Sano: The 245th JSMS Committee on Fatigue of Materials and The 36th JSMS Committee on Strength Design, Safety Evaluation, 40 (1999).

[6] E. Matsunaga, T. Tsuyuki, Y. Sano: CAMP-ISIJ, Vol. 11, 362 (1998).

[7] S. Tutumi, S. Hara, S. Yoshi: Tetsu-to-Hagane, Vol. 57, No. 5, pp. 818-822 (1971).

[8] S. Spuzic, K.N. Strafford, C. Subramanian, G. Savage: Wear, Vol. 176, No. 2, pp. 261-271 (1994).

[9] N. A. Noda, K. Hu, Y. Sano, K. Ono, Y. Hosokawa: Steel Res. Int., Vol. 87, No. 11, pp. 1478-1488 (2016).

[10] N. A. Noda, Y. Sano, Y. Takase, Y. Shimoda, G. Zhang: J. JSTP, Vol. 58, 66 (2017).

[11] K. Hu, Y. Xia, F. Zhu, N. A. Noda: Steel Res. Int., Vol. 89, No. 4, 1700368 (2017).

[12] N.A. Noda, H. Sakai, Y. Sano, Y. Takase, Y. Shimoda: Metals, Vol. 8, No.12, 998 (2018).

[13] H. Sakai, N.A. Noda, Y. Sano, G. Zhang, Y. Takase: Tetsu-to-Hagane, Vol. 105, No. 12, pp. 1126-1134 (2019).

[14] H. Sakai, N.A. Noda, Y. Sano, G. Zhang, Y. Takase: Tetsu-to-Hagane, Vol. 105, pp. 411-417 (2019).

[15] H. Sakai, N.A. Noda, Y. Sano, G. Zhang, Y. Takase: ISIJ Int., Vol. 59, No. 5, pp. 889-894 (2019).

[16] N. Soda: Bearing. Iwanami Shoten, Tokyo, pp. 196-203 (1964).

[17] Imai: Lubrication, Vol. 4, pp. 307 (1959).

[18] J. Murata, T. Onizuka: Koyo Eng. J., Vol. 166, pp. 41-47 (2005).

[19] T. Niwa: NTN Tech. Rev., Vol. 81, pp. 100-103 (2013).

[20] Ten, Sakajiri, Takemura, Yukawa: NSK Tech. J., Vol. 680, pp.13 (2006).

[21] New Bearing Doctor: Diagnosis of bearing problems. Objective: Smooth & reliable operation. NSK (1997).

[22] J. Zhan, H. Takemura, K. Yukawa: A study on bearing creep mechanism with FEM simulation. Proceedings of IMECE2007, 2007 Seattle, Washington, USA.

[23] J. Zhan, K. Yukawa, H. Takemura: Analysis of bearing outer ring creep with FEM. Advanced Tribology, 2009, Springer, Berlin, Heidelberg.

[24] S. Noguchi, K. Ichikawa, A study about creep between inner ring of ball bearing and shaft. Proceeding of Academic Lectures of the Japan Society for Precision Engineering, 2010, Japan.

[25] T. Teramoto, Y. Sato: Trans. Of Society of Automotive Eng. of Japan, Vol. 46, pp. 355-360 (2015).

[26] C. Bovet, L. Zamponi: Mech. Mach. Theory, Vol. 101, pp. 1-22 (2016).

[27] A. Maiwald, E. Leidich, FE simulations of irreversible relative movements (creeping) in rolling bearing seats –Influential parameters and remedies. World Congress on Engineering and Computer Science 2013 Vol II, San Francisco, USA.

[28] T. Schiemann, S. Porsch, E. Leidich, B. Sauer: Wind Energy, Vol. 21, pp. 426-440 (2018).

[29] T. Miyazaki, N.A. Noda, F. Ren, Z. Wang, Y. Sano, K. Iida: Int. J. Adhes. Adhes., Vol. 77, pp. 118-137 (2017).

[30] N.A. Noda, T. Miyazaki, R. Li, T. Uchikoba, Y. Sano, Y. Takase: Int. J. Adhes. Adhes., Vol. 61, pp. 46-64 (2015).

[31] N.A. Noda, T. Uchikoba, M. Ueno, Y. Sano, K. Iida, Z. Wang, G. Wang: ISIJ Int., Vol. 55, No. 12, pp. 2624-2630 (2015).

[32] Z. Wang, N.A. Noda, M. Ueno, Y. Sano: Steel Res. Int., Vol. 88, pp. 1-9 (2016).

[33] N.A. Noda, X. Chen, Y. Sano, M.A. Wahab, H. Maruyama, R. Fujisawa, Y. Takase: Mater. Des., Vol. 96, pp. 476-489 (2016).

[34] N.A. Noda, R. Takaki, Y. Shen, A. Inoue, Y. Sano, D. Akagi, Y. Takase, P. Galvez: Mech. Mater., Vol. 131, pp. 141-157 (2019).

[35]S. Matsuda, D. Suryadi, N. A. Noda, Y. Sano, Y. Takase, S. Harada: Trans. JSME Ser. A, Vol. 79, No. 803, pp. 989-999 (2013).
[36]N.A. Noda, D. Suryadi, S. Kumasaki, Y. Sano, Y. Takase: Eng. Fail. Anal., Vol. 57, pp. 219-235 (2015).
[37]N.A. Noda, Y. Xu, D. Suryadi, Y. Sano, Y. Takase: ISIJ Int., Vol. 56, No. 2, pp. 303-310 (2016).
[38]G. Zhang, H. Sakai, N.A. Noda, Y. Sano, S. Oshiro: ISIJ Int., Vol. 59, No. 2, pp. 293-299 (2019).
[39]Marc Mentat team: Theory and User Information, Vol. A, MSC, Software, Tokyo, 713 (2008).
[40]Misumi-vona Top, Technical information, Dry coefficient of friction. https://jp.misumi-ec.com/tech-info/categories/plastic_mold_design/pl07/c0874.html.

3 Interfacial slip in shrink-fitted bimetallic work roll promoted by motor torque

3.1 Introduction

In steel manufacturing industries, rolling processes more tonnage than any other metalworking process [1-15]. Four-high type consisting of a pair of work rolls and a pair of back-up rolls are most commonly used as strip mills. The technical innovations in the rolling strip mills have been conducted on the application and the improvement of large sleeved back-up roll [1-3], rolled steel with cross-section [4, 5], hot rolling strip mills [6-9], and bimetallic work roll [10-15].

Fig. 3-1(a) illustrates the rolling roll in steel roughing of a hot rolling stand mill. The rolls can be classified into two types; one is a single-solid type, and the other is a shrink-fitted assembly type consisting of a sleeve and a shaft as shown in Fig. 3-1(b) and Fig. 3-1(c). The shrink-fitted assembly type rolls are efficiently used as the back-up rolls having large trunk diameter exceeding 1000 mm and used for large H-section steel rolling rolls [1-3]. Those sleeve rolls have several advantages; the shaft can be reused by replacing the damaged sleeve due to the abrasion and the surface roughening and the sleeve wear resistance can be improved independently without loosening the shaft ductility.

On the other hand, this shrink-fitted assembly type roll has several particular problems such as residual bending of the roll, fatigue fracture at the end of the sleeve and sleeve fracture due to the circumferential slippage [5-12]. Among them, there is no detailed studies are available for the interfacial slippage in a rolling roll. It should also be pointed out that the interfacial slippage in shrink-fitted roll sometimes occurs even if the resistance torque at the interface is larger than the motor torque. Considering no quantitative study available for

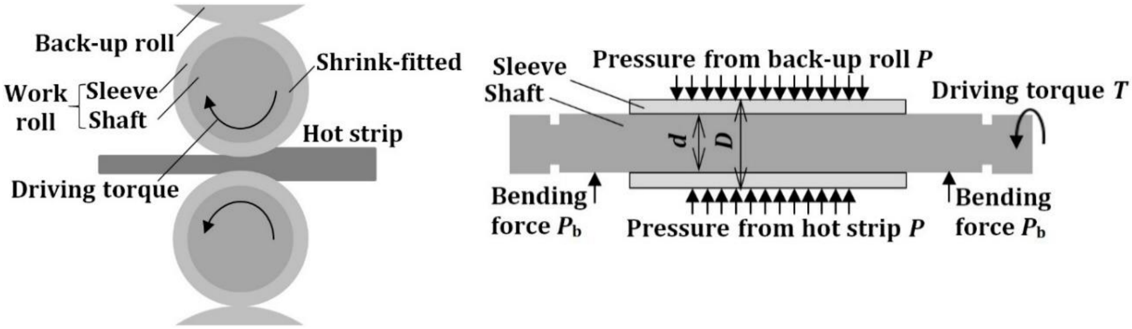

(a) Central cross-section view of rolling roll.

(b) Axial section view of rolling roll.

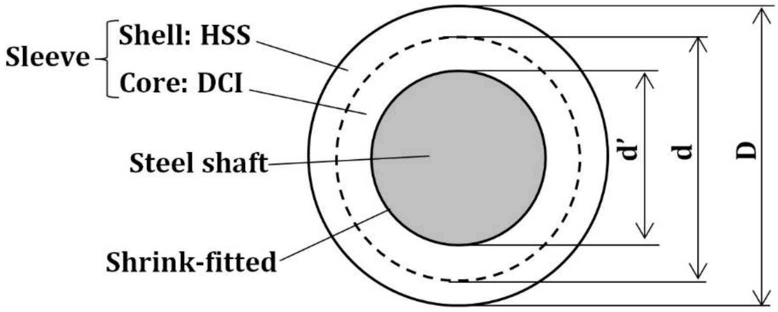

(c) A target of this study: HSS bimetallic roll in central cross-section.

Fig. 3-1 Schematic illustration for real hot strip rolling roll.

rolling rolls, by focusing on the sleeve displacement, the previous study assumed a rigid shaft modeling to simplify the phenomenon and to realize the slippage in the numerical simulation [13].

Although few studies are available for this new failure in shrink-fitted assembly type rolls, a similar phenomenon is known as “interfacial creep” in ball bearing appearing between the bearing and the stationary shaft and between the bearing and the housing [16-26]. However, even in the ball bearing field, few papers discussed the phenomenon quantitatively. In our previous study, therefore, the interfacial slip in the shrink-fitted roll under the free rolling condition was discussed without considering motor torque [14]. Then, it was found that the interfacial slip occurs even under free rolling conditions and under no friction and no motor torque. However, in the real rolling process, to reduce the thickness of the rolling plate, pair of sleeve rolls are driven by motor torque. Far differently from free rolling, a larger amount of slippage may happen due to the motor torque.

To clarify the effect of the motor torque on the interfacial slip, in this study, the actual work roll of a hot rolling stand mill will be simulated under a similar condition of the real roll. Fig. 3-1(a) illustrates that the motor torque and the balanced frictional force from the rolled steel promote the slippage significantly. In the actual work roll of a hot rolling stand, differently from ball bearings, such promoted slippage may cause a serious failure. In this sense, the effects of the shrink-fitting ratio and the friction coefficient will be discussed since they may contribute to slippage resistance. Finally, the novel design concept for the sleeve roll will be proposed from the discussion.

3.2 Simulation for non-uniform slip versus overall slip considered in conventional design

Fig. 3-1 shows a sleeve assembly type roll used in rolling roll. Fig. 3-1(a) shows the central cross-section and Fig. 3-1(b) shows the axial cross-section. As shown in Fig. 3-1, the sleeve roll consists of a shrink-fitted sleeve and shaft. Fig. 3-1(c) shows an example of a commonly used bimetallic sleeve roll made by the centrifugal casting method. Here, the outer layer is high-speed steel (HSS) having high abrasion resistance and the inner layer is ductile casting iron (DCI) having high ductility. To simplify the analysis and to clarify “the interfacial slip”, this present study will focus on a single material sleeve roll instead of the bimetallic sleeve roll. In the field of ball bearing, the phenomenon of such slip is referred to as “interfacial creep”. In this paper, however, the phenomenon is named “an

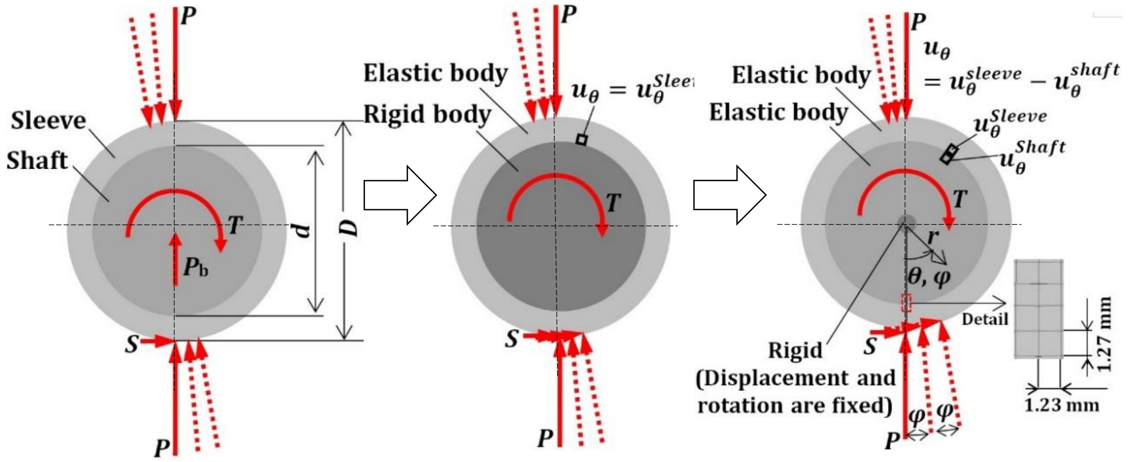

P: Load form back-up roll and hot strip (N)
S: Frictional force (N)
P_b: Bending force from bearing (N)
T: Driving torque (Nm), $T = SD/2$
T_m: Rated torque of motor (Nm)
T_r: Slippage resistance torque (Nm)

$T = 0 \sim 10T_m$
$10T_m > T_r = 3193$ Nm /mm
$T_m = 471$ Nm /mm
$P_b = 0$

θ: Circumferential angle of sleeve
φ_0: Load shift interval
φ : Load shift angle

(a) Real roll

(b) Rigid shaft when $E_{shaft} \to \infty$

(c) Elastic shaft when $E_{shaft} = 210$ GPa

Fig. 3-2 Modeling for "non-uniform interfacial slip" different from "overall slip" considered in the conventional design.

interface slip" according to the usage of sleeve assembly type rolls in the rolling field.

As shown in Fig. 3-1(a), the roll is subjected to the contact force P from the back-up roll, the rolling force P_h and the frictional force S (shear force) from the rolling plate. Since two-dimensional modeling is used in this study, the external force per unit length, as well as motor torque T, should be considered. In Fig. 3-1(b), the back-up roll is longer than the width of the rolling plate; and therefore, the bending force P_b is acting at the bearing. Here, the rolling force P, the rolling reaction force P_h and the bending force P_b should be balanced, but P_b is estimated to be less than 10% of P and P_h [5]. Therefore, in this study, by assuming the bending force $P_b = 0$, the rolling force ($= \sim P \times$ back-up roll body length) is equal to the rolling force ($= \sim P_h \times$ strip width) as $P \simeq P_h$. This modeling refers to the loading at the fifth stage of the hot finishing roll [5].

Fig. 3-2 indicates the numerical simulation model used in this study concerning the actual roll approach. The rotation of the roll is expressed by the circumferential load transfer on the roll surface without rotating the roll [13, 14]. Fig. 3-2(a) shows two-dimensional real roll conditions. Fig. 3-2(b) shows a roll model in which the entire shaft is rigid assumed in the previous paper to simplify the phenomenon and to realize the slippage in the numerical simulation [13]. This is because this phenomenon is hard to be proved and considering no quantitative study available for rolling rolls. Based on the analysis of the rigid shaft, the analysis method can be confirmed and clarified for the elastic shaft, which is closer to the real roll conditions. As shown in Fig. 3-2(c), to restrain the displacement and rotation of the center of the roll in order to justify the elastic deformation of the sleeve and shaft, a small rigid body at the center of the shaft is introduced. In this analysis, the rigid body size at the center has been confirmed does not affect the result and the diameter is set to be 8 mm. The load transfer interval is set to be $\varphi = 4^o$ in consideration of computational time without loosening the analysis accuracy.

The roll is subjected to the force P from the back-up roll, the rolling reaction force P and the frictional force S from the roll material, and the driving torque T from the motor. In the previous paper, the interface slip was discussed under the motor torque $T = 0$ and the friction force $S = 0$ [14]. In this paper, the interfacial slip will be considered under driving torque $T \neq 0$ and the friction force $S \neq 0$.

To distinguish from “an overall slip” considered in the conventional design, the slip considered in this study can be named as “a non-uniform slip”.

This is because due to the applied force P, a non-uniform deformation appears at the interface. Instead, the conventional machine design has considered the following condition conventionally stating that the motor torque should be smaller than the slippage resistance torque T_r as defined in Eq. (3-1).

$$T < T_r, \qquad T_r = \xi \frac{d}{2} \pi d l_b \mu \sigma_{r_{shrink}} (Nm/mm) \qquad (3-1)$$

Here, d is the shaft outer diameter, which is equal to the sleeve inner diameter, l_b is the roll barrel length, μ is the friction coefficient between the shaft and the sleeve, and $\sigma_{r_{shrink}}$ is the shrink-fitting stress. The notation ξ denotes the effective shrink-fitting ratio considering manufacturing error. Although under $T < T_r$ the overall slip can be prevented, the non-uniform slip may happen.

The sleeve resistance torque T_r can be calculated as $T_r = 3193$ Nm/mm under the standard conditions when $\xi = 1$, $l_b = 1$ mm, $\mu = 0.3$, $\sigma_{r_{shrink}} = -21.6$ MPa and $\delta/d = 0.5 \times 10^{-3}$. The real torque can be expressed as $T_m = \eta 471$ Nm/mm by using the reduction ratio $\eta = 1.882$ [39]. In this study, $\eta = 1$ is used to express the rated motor torque as $T_m = 471$ Nm/mm to confirm that the smaller rated torque may cause the interfacial slip.

In the shrink-fitting type roll, the slippage resistance torque T_r on the roll side has to be larger than the shaft driving torque T as shown in Eq. (3-2) by using α denoting the slippage safety factor.

$$T_r = \alpha T \ (Nm/mm) \qquad (3-2)$$

Under the rated motor torque as $T = T_m = 471$ Nm/mm, the safety factor $\alpha = 6.77$ from Eq. (3-2). The shear force S can be obtained from Eq. (3-3).

$$T_m = S \frac{D}{2} (Nm/mm) \qquad (3-3)$$

When the rated motor torque is $T_m = 471$ Nm/mm, the friction force (=shearing force) is obtained as $S = 1346$ Nm/mm from Eq. (3-3).

Table 3-1
Mechanical properties, dimensions and boundary conditions in Fig. 3-2(c) [13, 14].

Mechanical properties	Sleeve	Young's modulus of steel sleeve E_{sleeve}	210 GPa
		Poisson's ratio of steel sleeve υ	0.28
	Shaft	Young's modulus of elastic shaft E_{shaft}	210 GPa
		Poisson's ratio of steel shaft υ	0.28
Roll size		Outer diameter of sleeve	700 mm
		Inner diameter sleeve d	560 mm
Shrink fitting		Shrink fitting ratio δ/d	0.5×10^{-3}
		Friction coefficient between sleeve and shaft μ	0.3
External force		Concentrated load per unit thickness $P = P_0$	13270 N/mm Total: 1.327×10^{7} N Rolled width: 1000 mm
		Frictional force per unit thickness S	1346 N/mm
		Rated torque of motor per unit thickness T_m	471 Nm/mm
		Resistance torque per unit thickness T_r	3193 Nm/mm
		Bending force from bearing P_b	0 N/mm

On the basis of the experience and skills for engineering applications, the finite element method (FEM) should be well conducted to realize the interface slippage. Therefore, Fig. 3-2(c) also shows the mesh division for the finite element simulation model. In the previous studies, the FEM mesh error was discussed for bonded problems and the mesh-independent technique was proposed confirming that the provided displacement boundary condition is relatively insensitive to mesh division [27-30]. The tightening process of the pitch-difference nut with the dynamic deformation was investigated through consecutive quasi-static analyses to clarify the contact status change in the bolt and nuts threads [31, 32]. On the basis of those skills, the axial movement of the shaft during the ceramic roll rotation was analyzed by shifting the load on the fixed shaft [33-36]. The circumferential sleeve slippage will be realized in this study by extending the above technique to the elastic contact quasi-static analysis for rolling rolls and applying FEM code Marc/Mentat 2012. In this code, the complete Newton-Raphson method and the direct constraint method for the contact analysis are used. As shown in Fig. 3-2(c), 4-node quadrilateral plane strain elements are used with the number of mesh elements are 309440 with confirming the mesh independence of the results [37].

Table 3-1 shows the mechanical properties, dimensions and boundary conditions of the model in Fig. 3-2(c). In this study, the loading condition used is based on the data at No. 5 stand for roll hot strip finishing roll mill [4, 5]. Assume the concentrated load $P = P_0 = 13270$ N/mm from the back-up roll, which is equal to the reaction from the strip [4, 5]. By replacing Hertzian contact stress with the concentrated force P, the small effect on the analysis can be confirmed. The shrink-fitting ratio is defined as δ/d, where δ is the diameter difference between sleeve inner diameter and shaft outer diameter. Usually, the shrink-fitting ratio in the range $\delta/d = 0.4 \times 10^{-3} \sim 1.0 \times 10^{-3}$ is applied to sleeve rolls based on the long year experience. This is because a smaller value $\delta/d < 0.4 \times 10^{-3}$ may cause an interface to slip easily and a larger value $\delta/d < 0.4 \times 10^{-3}$ may increase the risk of sleeve fracture [6]. In this paper, $\delta/d = 0.5 \times 10^{-3}$ is focused to study the irreversible interfacial slip. The effect of the shrink-fitting ratio is discussed in Section 3.4.2. Previously, regarding the friction coefficient μ which controls the slippage resistance on the interface, $\mu =$

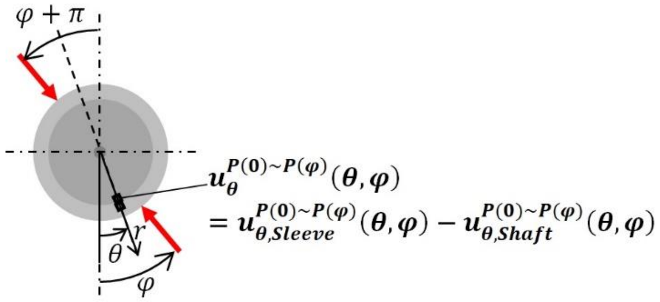

$$u_{\theta,ave.,T=T_m}^{P(0)\sim P(\varphi)}(\varphi)=\frac{1}{2\pi}\int_0^{2\pi}u_\theta^{P(0)\sim P(\varphi)}(\theta,\varphi)\,d\theta$$

(a) Definition of interfacial displacement $u_\theta^{P(0)\sim P(\varphi)}(\theta,\varphi)$ due to the load shifting $P(0)\sim P(\varphi)$.

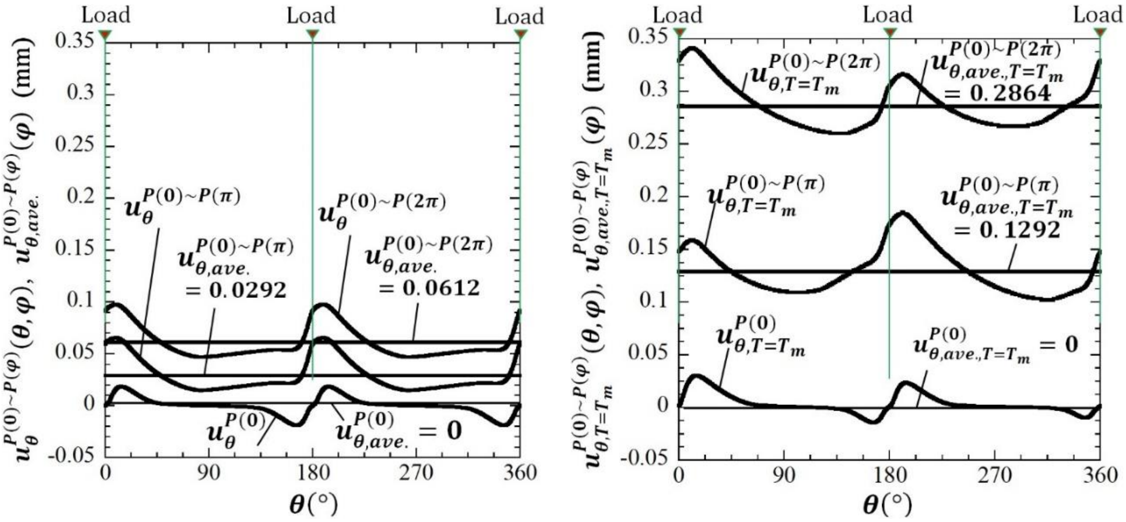

(b) Non-uniform interfacial slip for $T=0$

(c) Non-uniform interfacial slip for $T=T_m$

Fig. 3-3 (a) Definition of $u_\theta^{P(0)\sim P(\varphi)}$, (b) $u_\theta^{P(0)\sim P(\varphi)}$ when $T=0$ and $E_{shaft}=$ 210 GPa, and (c) $u_\theta^{P(0)\sim P(\varphi)}$ when $T=T_m$ and $E_{shaft}=210$ GPa.

0.2 was used in an experimental study, and $\mu=0.4$ was often used for steel surfaces [1, 38]. Therefore, since $\mu=0.2\sim0.4$ is usually used for sleeve assembly type rolls, the friction coefficient $\mu=0.3$ between the sleeve and the shaft is used in this study.

The relative displacement accumulation between the sleeve and shaft may represent the interfacial slip. In Fig. 3-3(a), the relative displacement between the sleeve and shaft due to the load shifting $P(0)\sim P(\varphi)$ when the load moves from the angle $\varphi = 0$ to $\varphi = \varphi$ is defined as $u_\theta^{P(0)\sim P(\varphi)}(\theta, \varphi)$. The relative displacement u_θ between the elastic shaft and elastic sleeve on the shrink-fitted surface can be expressed as in Eq. (3-4) which is defined as the interfacial slip on the shrink-fitted surface.

$$u_\theta^{P(0)\sim P(\varphi)}(\theta, \varphi) = u_{\theta,Sleeve}^{P(0)\sim P(\varphi)}(\theta, \varphi) - u_{\theta,Shaft}^{P(0)\sim P(\varphi)}(\theta, \varphi) \qquad (3-4)$$

Here, notation φ denotes the angle where the load is shifting and notation θ denotes the position where the displacement is evaluated. The load $P(\varphi)$ used in this study is defined as the symmetry forces acting at $\varphi = \varphi$ and $\varphi = \varphi + \pi$. The relative displacement $u_\theta(\theta, \varphi)$ at $\theta = \theta$ when the pair of loads are applied at $\varphi = 0$ to $\varphi = \varphi$ and $\varphi = \pi$ to $\varphi = \varphi + \pi$ is denoted as $u_\theta^{P(0)\sim P(\varphi)}(\theta, \varphi)$. To express the amount of the slip with increasing φ, the average displacement can be defined in the following equation.

$$u_{\theta,ave.,T=T_m}^{P(0)\sim P(\varphi)}(\varphi) = \frac{1}{2\pi}\int_0^{2\pi} u_\theta^{P(0)\sim P(\varphi)}(\theta, \varphi)\, d\theta \qquad (3-5)$$

Fig. 3-3(b) shows the effect of no torque condition $T = 0$ on the displacement distribution $u_\theta^{P(0)\sim P(\varphi)}(\theta, \varphi)$ and Fig. 3-3(c) shows the effect of the rated motor torque $T = T_m$ on the displacement distribution $u_\theta^{P(0)\sim P(\varphi)}(\theta, \varphi)$ when the load is moving to $\varphi = 0$, $\varphi = \pi$ and $\varphi = 2\pi$. As shown in Fig. 3-3(b), the average displacement is zero as $u_{\theta,ave.}^{P(0)}(\varphi) = 0$ when the initial load P is applied at $\varphi = 0$. It is important to note that the distribution of the displacements $u_\theta^{P(0)}(\theta)$ is non-zero except at $\theta = 0$, π and 2π. This non-zero displacement means such local slippage may appear once the load is applied. Although $u_\theta^{P(0)}(\theta)$ is symmetric as shown in Fig. 3-3(b), with increasing the load shifting angle φ, the average displacement $u_{\theta,ave.}^{P(0)\sim P(\varphi)}(\varphi)$ increases after losing the symmetry. On the other hand, as shown in Fig. 3-3(c), at the initial load $\varphi = 0^o$, the magnitude of the displacement is different near both sides of the load position (at $\theta < 0$ and $\theta > 0$) on which the shear forces are applied ($\theta = 0^o$). Due to the shear force, the magnitude of the displacement is larger on the positive direction of the shear force ($\theta > 0^o$), $\left|u_{\theta,T=T_m}^{P(\varphi)}(-\theta)\right| < \left|u_{\theta,T=T_m}^{P(\varphi)}(+\theta)\right|$. Moreover, the displacement distributions are not symmetric anymore due to the effect of the rated motor torque T_{m} as given in the following equation:

$$\left|u_{\theta,T=T_m}^{P(\varphi)}(-\theta)\right| < \left|u_{\theta,T=T_m}^{P(\varphi)}(+\theta)\right| \qquad (3-6)$$

As shown in Fig. 3-3(b) and Fig. 3-3(c), the average displacement of half roll rotation $u_{\theta,ave.}^{P(0)\sim P(\pi)}(\varphi)$ when $T = T_m$ is about 4 times larger than that under no torque condition $T = 0$. In addition, the average displacement of one roll rotation $u_{\theta,ave.}^{P(0)\sim P(2\pi)}(\varphi)$ when $T = T_m$ is about 5 times larger than no torque condition $T = 0$. This result shows that the presence of the motor torque significantly accelerates the interfacial slip.

3.3 Interfacial slip under rated motor torque $T = T_m$

3.3.1 Interfacial displacement and increase rate of interfacial displacement

Fig. 3-4(a) shows the relationship between the average displacement $u_{\theta,\mathrm{ave.}}^{P(0)\sim P(\varphi)}(\varphi)$ and the load rotation angle φ for the elastic shaft under no toque $T = 0$ and under the rated motor torque $T = T_m$. In Fig. 3-4(a), regardless of the motor torque condition, the average value increases almost linearly during the initial roll rotation. The average displacement of one roll rotation $u_{\theta,ave.}^{P(0)\sim P(2\pi)}(\varphi)$ when $T = T_m$ is about 5 times larger than that under no torque condition $T = 0$. From Fig. 3-4(a), it should be noted that the average displacement $u_{\theta,\mathrm{ave.}}^{P(0)\sim P(\varphi)}(\varphi)$

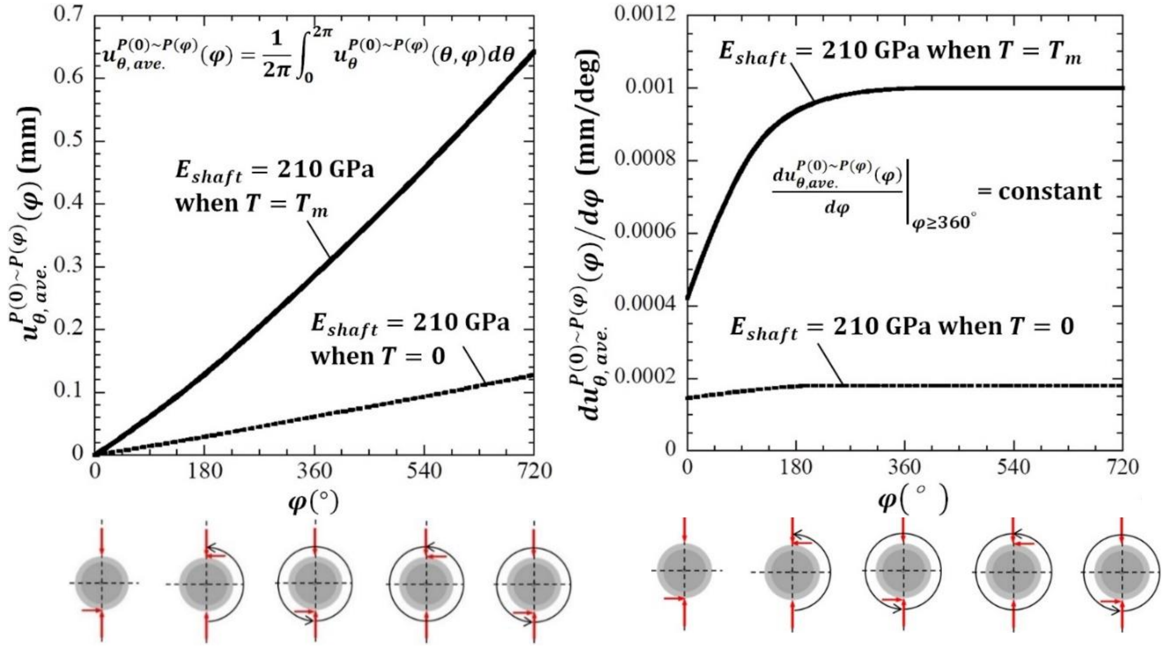

(a) Interfacial displacement

(b) Increase rate of interfacial displacement

Fig. 3-4 Interfacial displacement and increase rate of interfacial displacement for elastic shaft $E_{shaft} = 210$ GPa when $T = 0$ and $T = T_m$.

at $\varphi = 2\pi \times 2$, that is, 2 roll rotations, is about 2 times larger than $u_{\theta,\text{ave.}}^{P(0)\sim P(\varphi)}(\varphi)$ at $\varphi = 2\pi$. Therefore, the slippage increases linearly after the initial roll rotation $\varphi \geq 2\pi$.

Therefore, as shown in Fig. 3-4(b), the interfacial slip is quantitatively evaluated by focusing on the increase rate of interfacial displacement $\mathrm{d}u_\theta^{P(0)\sim P(2\pi)}(\theta,\varphi)/\mathrm{d}\varphi$. In Fig. 3-4(b), the displacement increase rate $\mathrm{d}u_\theta^{P(0)\sim P(2\pi)}(\theta,\varphi)/\mathrm{d}\varphi$ under the rated motor torque $T = T_m$ is nearly 5 times larger than under no toque condition $T = 0$. In addition, regardless of the motor torque condition, before the initial one roll rotation, the interfacial slip is unstable since the displacement increase rate $\mathrm{d}u_\theta^{P(0)\sim P(\varphi)}(\theta,\varphi)/\mathrm{d}\varphi\big|_{\varphi<360°}$ increases gradually. After the initial one roll rotation, however, the interfacial slip becomes stable since $\mathrm{d}u_\theta^{P(0)\sim P(\varphi)}(\theta,\varphi)/\mathrm{d}\varphi\big|_{\varphi\geq 360°}$ is constant. The displacement increase rate

$\mathrm{d}u_{\theta}^{P(0)\sim P(\varphi)}(\theta,\varphi)/\mathrm{d}\varphi$ for more than one roll rotation can be evaluated accurately from the displacement increase rate $\mathrm{d}u_{\theta}^{P(0)\sim P(\varphi)}(\theta,\varphi)/\mathrm{d}\varphi\Big|_{\varphi\geq 360^{\circ}}$ at the initial one roll rotation.

3.3.2 Slippage zone affected by the motor torque

Fig. 3-5 shows the shear stress distribution $\tau_{r\theta}^{P(0)\sim P(2\pi)}$ in comparison with the frictional stress $\mu\sigma_r^{P(0)\sim P(2\pi)}$ along the shrink-fitting surface. Fig. 3-5(a) shows the result of $E_{shaft} = 210$ GPa after the initial one roll rotation $P(0)\sim P(2\pi)$ under free rolling roll condition $T = 0$. Fig. 3-5(b) shows the result of $E_{shaft} = 210$ GPa after the initial one roll rotation $P(0)\sim P(2\pi)$ under rated motor torque $T = T_m$. The notation $P(0)\sim P(2\pi)$ denotes the initial one roll rotation expressed by the load shifting on the fixed roll from $\varphi = 0$ to $\varphi = 2\pi$. Although the displacement increases with increasing φ as shown in Fig. 3-4(a), the preceding paper confirmed that the stress σ_θ change slightly with less than 8% by increasing φ [15]. It has been confirmed that the slippage zone does not change after one rotation of the load.

In the previous experimental studies for sleeve roll [1], the friction coefficient $\mu = 0.2$ was used in an experimental study to discuss the slippage resistance on the interface. For the steel surfaces in general, and $\mu = 0.4$ was often used [38]. Therefore, in this study, the friction coefficient $\mu = 0.3$ is assumed between the sleeve and the shaft. By considering the FEM accuracy, the irreversible relative displacement may appear when $\tau_{r\theta} \cong |\mu\sigma_r|$ within the error ±1 MPa. This region is defined as the slippage zone ℓ_{slip}. In the previous paper [12], the slippage zone ℓ_{slip} was named "quasi-equilibrium stress zone $\tau_{r\theta} \cong |\mu\sigma_r|$". As shown in Fig. 3-5, the slippage zone ℓ_{slip} is much larger under rated motor torque $T = T_m$ (Fig. 3-5(b)) compared with under the free rolling $T = 0$

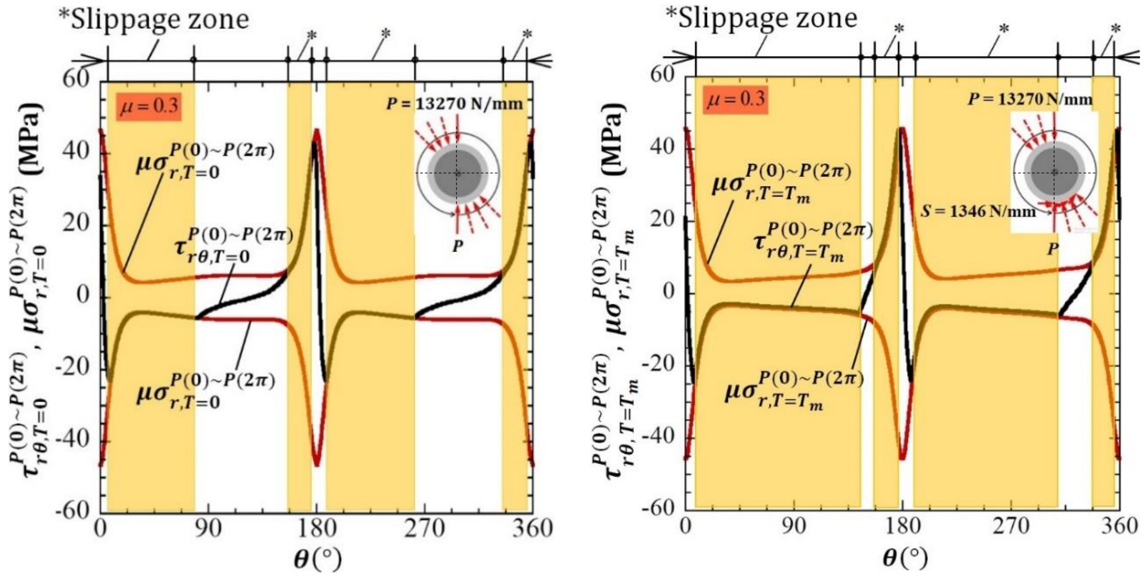

(a) Elastic shaft $E_{shaft} = 210$ GPa after the initial one roll rotation $P(0){\sim}P(2\pi)$ with $T = 0$.

(b)Elastic shaft E_{shaft}=210 GPa after the initial one roll rotation $P(0){\sim}P(2\pi)$ with $T = T_m$.

Fig. 3-5 Comparison of the slippage zone where $\tau_{r\theta} \cong |\mu\sigma_r|$ for (a) the elastic shaft $E_{shaft} = 210$ GPa with $T = 0$ and (b) the elastic shaft $E_{shaft} = 210$ GPa with $T = T_m$, both under the loading shift $P(0){\sim}P(2\pi)$ and $\mu = 0.3$.

(Fig. 3-5(a)). This is the reason why the interfacial displacement increases in Fig. 3-4(a) due to the rated motor torque $T = T_m$.

3.4 Effect of design factors and new design concept based on non-uniform slip

3.4.1 Effect of motor torque T on non-uniform slip

In the above discussion, the rated motor torque T_m has been applied to the roll. In addition to the rated motor torque T_m, sometimes excessively large torque is applied to the shaft of the real roll. This is because even though the roll is driven by a rated motor, several factors affect larger torque such as reduction ratio η, upper and lower roll distribution ratio, over torque, and impact

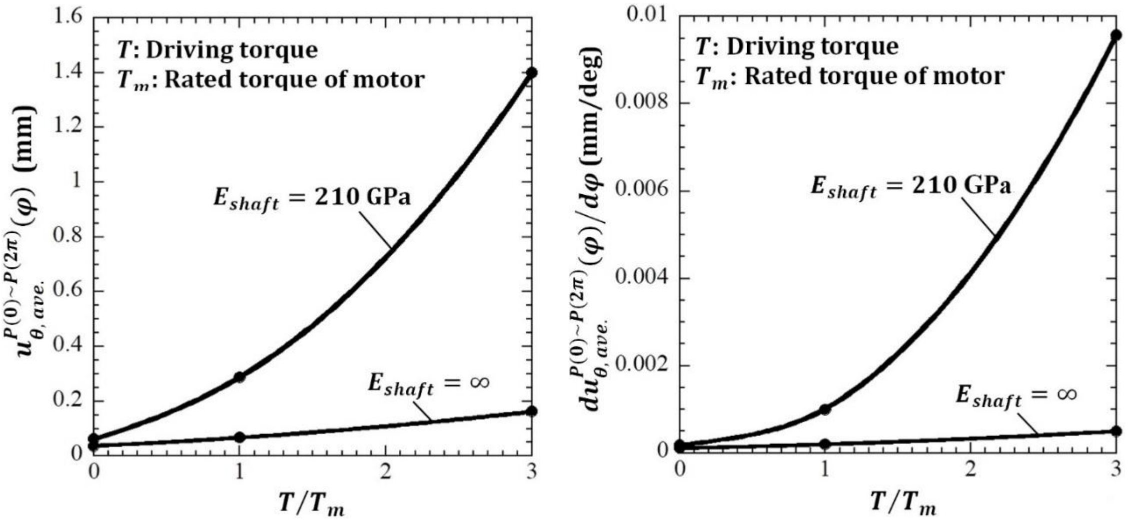

(a) Average displacement vs. T/T_m when $P = P_0$ and $E_{shaft} = 210$ GPa.

(b) Increase rate of interfacial displacement vs. T/T_m when $P = P_0$ and $E_{shaft} = 210$ GPa.

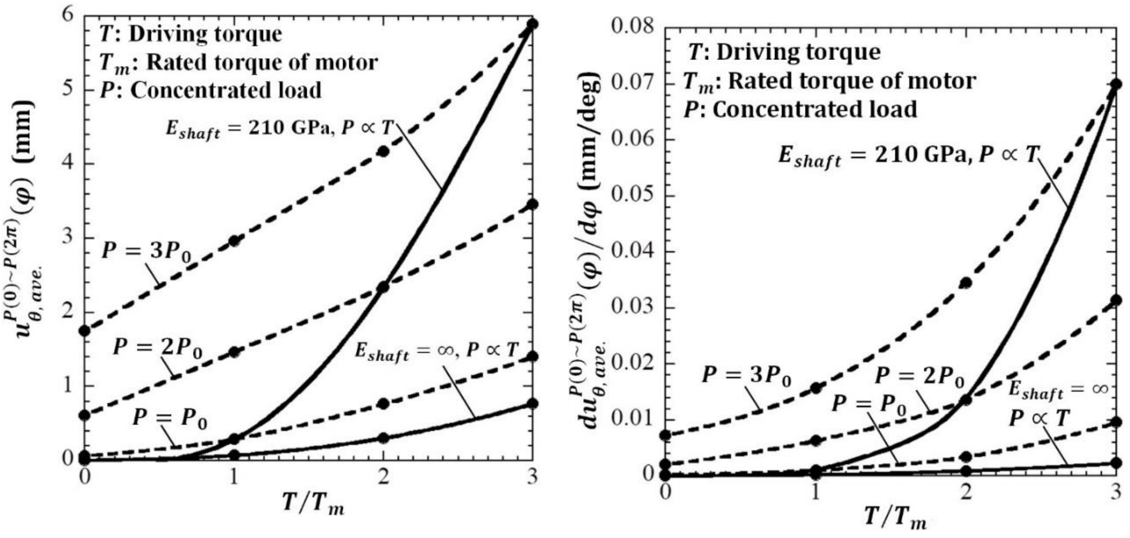

(c) Average displacement vs. T/T_m for $E_{shaft} = 210$ GPa when $P = P_0$, $P = 2P_0$ and $P = 3P_0$.

(d) Increase rate of interfacial displacement vs. T/T_m for $E_{shaft} = 210$ GPa when $P = P_0$, $P = 2P_0$ and $P = 3P_0$.

Fig. 3-6 Average displacement and increase rate of displacement vs. T/T_m when $\varphi = 2\pi$.

coefficient when the rolled material is caught. Therefore, in this study, in addition to the no torque condition $T = 0$ and the rated motor torque $T = T_m$, other torque conditions $T = 2T_m$, $T = 3T_m$ are also applied.

Fig. 3-6(a) shows the effect of torque T normalized by the reference value T/T_m on the average displacement $u_{\theta,ave.T}^{P(0)\sim P(2\pi)}(\varphi)$ under one roll rotation $\varphi = 2\pi$ when the load $P = P_0$ for the elastic shaft $E_{shaft} = 210$ GPa as well as rigid shaft $E_{shaft} = \infty$. With increasing T/T_m, $u_{\theta,ave.T}^{P(0)\sim P(2\pi)}(\varphi)$ increases significantly. The average displacement $u_{\theta,ave.T}^{P(0)\sim P(2\pi)}(\varphi)$ under the rated motor torque $T = T_m$ for the elastic shaft is 4 times larger than that of the rigid shaft, and $u_{\theta,ave.T}^{P(0)\sim P(2\pi)}(\varphi)$ under $T = 3T_m$ for the elastic shaft is 9 times larger than the rigid shaft. As shown in Fig. 3-6(a), at $T = 0$, the average displacement $u_{\theta,ave.T}^{P(0)\sim P(2\pi)}(\varphi) \neq 0$, which means under free rolling, the slippage may happen as discussed in the previous paper [14].

Fig. 3-6(b) shows the effect of T/T_m on the displacement increase rate $\mathrm{d}u_{\theta}^{P(0)\sim P(2\pi)}(\theta,\varphi)/\mathrm{d}\varphi$ at the initial one roll rotation $\varphi = 2\pi$ when the load $P = P_0$ for the elastic shaft $E_{shaft} = 210$ GPa as well as rigid shaft $E_{shaft} = \infty$. With increasing T/T_m, $\mathrm{d}u_{\theta}^{P(0)\sim P(2\pi)}(\theta,\varphi)/\mathrm{d}\varphi$ increases significantly. The displacement increase rate $\mathrm{d}u_{\theta}^{P(0)\sim P(2\pi)}(\theta,\varphi)/\mathrm{d}\varphi$ under the rated motor torque $T = T_m$ for the elastic shaft is 5 times larger than the one of the rigid shaft, and $\mathrm{d}u_{\theta}^{P(0)\sim P(2\pi)}(\theta,\varphi)/\mathrm{d}\varphi$ under $T = 3T_m$ for the elastic shaft is 19 times larger than the one of the rigid shaft. In the early stage of our study, we assumed the rigid shaft modeling by focusing on the sleeve displacement. However, Fig. 3-6(a) and Fig. 3-6(b) show the elastic shaft modeling is necessary. In Fig. 3-4(b) and Fig. 3-6(b), at $T = 0$, the displacement increase rate $\mathrm{d}u_{\theta}^{P(0)\sim P(2\pi)}(\theta,\varphi)/\mathrm{d}\varphi \neq 0$, which may cause the slippage under free rolling $T = 0$ [14].

Next, in addition to the no torque condition $T = 0$ and the standard rolling conditions $P = P_0, T = T_m$, the extreme condition $P = 3P_0, T = 3T_m$ is considered. Here $P = 3P_0, T = 3T_m$ is assumed to be in the state of rolling trouble. In Fig. 3-6(c), the solid line shows the effect of T/T_m on the average displacement $u_{\theta,ave.T}^{P(0)\sim P(2\pi)}(\varphi)$ when both P and T increase proportionally. The average displacement $u_{\theta,ave.T}^{P(0)\sim P(2\pi)}(\varphi)$ for the elastic shaft $E_{shaft} = 210$ GPa under $P = 3P_0, T = 3T_m$ is 20 times larger than that of $P = P_{0,} T = T_m$. In addition, under the rolling trouble state $P = 3P_0, T = 3T_m$, $u_{\theta,ave.T}^{P(0)\sim P(2\pi)}(\varphi)$ for the elastic shaft is 8 times larger than that of the rigid shaft. In Fig. 3-6(c), the dotted line shows the average displacement $u_{\theta,ave.T}^{P(0)\sim P(2\pi)}(\varphi)$ when the load P is fixed as $P = P_0, P = 2P_0$, $P = 3P_0$ by varying the motor torque T. Under fixed $P = P_{0,}$ the average displacement $u_{\theta,ave.T}^{P(0)\sim P(2\pi)}(\varphi)$ at $T = 3T_m$ is 5 times larger than $u_{\theta,ave.T}^{P(0)\sim P(2\pi)}(\varphi)$ at $T = T_m$. However, under fixed $T = T_m$, the average displacement $u_{\theta,ave.T}^{P(0)\sim P(2\pi)}(\varphi)$ at $P = 3P_0$ is 10 times larger than that at $P = P_0$. This observation explained that the effect P on the average displacement $u_{\theta,ave.T}^{P(0)\sim P(2\pi)}(\varphi)$ is larger than the effect T.

In Fig. 3-6(d), the solid line shows the effect of T/T_m on the increase rate of interfacial displacement $\mathrm{d}u_\theta^{P(0)\sim P(2\pi)}(\theta,\varphi)/\mathrm{d}\varphi$ when P and T increase proportionally. The displacement increase rate $\mathrm{d}u_\theta^{P(0)\sim P(2\pi)}(\theta,\varphi)/\mathrm{d}\varphi$ for elastic shaft $E_{shaft} = 210$ GPa under $P = 3P_0, T = 3T_m$ is 70 times larger than that of $P = P_{0,} T = T_m$. In addition, under the rolling trouble state $P = 3P_0, T = 3T_m$, $\mathrm{d}u_\theta^{P(0)\sim P(2\pi)}(\theta,\varphi)/\mathrm{d}\varphi$ for the elastic shaft is 31 times larger than that of the rigid shaft. In Fig. 3-6(d), the dotted line shows the displacement increase rate $\mathrm{d}u_\theta^{P(0)\sim P(2\pi)}(\theta,\varphi)/\mathrm{d}\varphi$ when the load P is fixed as $P = P_0, P = 2P_0$, $P = 3P_0$ by varying the motor torque T. Under fixed $P = P_{0,}$ the displacement increase rate $\mathrm{d}u_\theta^{P(0)\sim P(2\pi)}(\theta,\varphi)/\mathrm{d}\varphi$ at $T = 3T_m$ is 10 times larger than $\mathrm{d}u_\theta^{P(0)\sim P(2\pi)}(\theta,\varphi)/\mathrm{d}\varphi$ at $T = T_m$. However, under fixed $T = T_m$, the displacement increase rate

$\mathrm{d}u_{\theta}^{P(0)\sim P(2\pi)}(\theta, \varphi)/\mathrm{d}\varphi$ at $P = 3P_0$ is 16 times larger than that at $P = P_0$. The larger change can be seen in the displacement increase rate $\mathrm{d}u_{\theta}^{P(0)\sim P(2\pi)}(\theta, \varphi)/\mathrm{d}\varphi$ compared to the average displacement $u_{\theta,ave.T}^{P(0)\sim P(2\pi)}(\varphi)$. If the rolling trouble happens, care should be taken for $\mathrm{d}u_{\theta}^{P(0)\sim P(2\pi)}(\theta, \varphi)/\mathrm{d}\varphi$ increases abruptly.

As shown in Fig. 3-6(c) and 3-6(d), under zero torque $T = 0$, the average displacement $u_{\theta,ave.T}^{P(0)\sim P(2\pi)}(\varphi)$ as well as the displacement increase rate $\mathrm{d}u_{\theta}^{P(0)\sim P(2\pi)}(\theta, \varphi)/\mathrm{d}\varphi$ increases with increasing the loading force P. Therefore, the circumferential slippage under free rolling can be explained from the non-uniform deformation due to the rolling force P. In this way, the reason why there is still resultant circumferential slip in the case of zero torque [14] becomes clearer in this paper.

3.4.2 Effect of shrink-fit ratio δ/d on non-uniform slip

To prevent the overall sleeve slippage in shrink-fitted rolling roll, the slip resistance torque T_r in Eq. (3-1) should be larger than the motor torque as $T_r > T$, but also the non-uniform slip considered in this study may happen. In this section, the shrink-fitting ratio controlling the shrink-fitting pressure $\sigma_{r_{shrink}}$ in Eq. (3-1) is focused. In the above discussion, the shrink-fitting ratio $\delta/d = 0.5 \times 10^{-3}$ is fixed to clarify the effect of the motor torque T on the interface slippage. When $\delta/d = 0.5 \times 10^{-3}$, the slip resistance torque T_r is larger than the rated motor toque T_m as $T_r = 6.77\, T_m$. Generally, in the sleeve assembly type roll, the shrink-fitting ratio is applied in the range $\delta/d = 0.4 \times 10^{-3} \sim 1.0 \times 10^{-3}$. The limitation of δ/d range is based on many years of experience. This is because a smaller value $\delta/d < 0.4 \times 10^{-3}$ may cause an interface to slip easily and a larger value $\delta/d > 1.0 \times 10^{-3}$ may increase the risk of sleeve fracture [6].

Fig. 3-7 indicates the increase rate of interfacial displacement

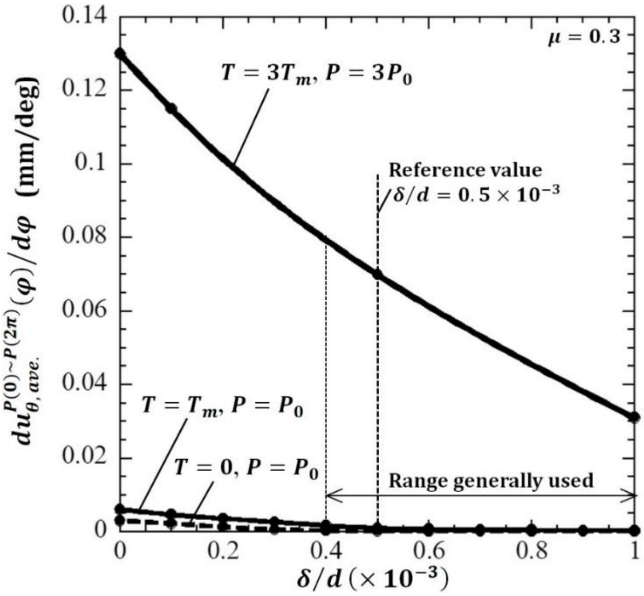

Fig. 3-7 Increase rate of interfacial displacement vs. δ/d when $\varphi = 2\pi$, $T = 0, P = P_0$, $T = T_m, P = P_0$ and $T = 3T_m, P = 3P_0$.

$\mathrm{d}u_\theta^{P(0)\sim P(2\pi)}(\theta,\varphi)/\mathrm{d}\varphi$ by varying the shrink-fitting ratio δ/d in the range $\delta/d = 0\sim 1.0 \times 10^{-3}$. The displacement increase rate $\mathrm{d}u_\theta^{P(0)\sim P(2\pi)}(\theta,\varphi)/\mathrm{d}\varphi$ decreases with increasing shrink-fitting ratio δ/d regardless of the torque condition. This is because with increasing δ/d, the fitting pressure $\sigma_{r_{shrink}}$ increases. Then the slip resistance increases and the displacement increasing rate $u_\theta^{P(0)\sim P(2\pi)}(\theta,\varphi)/\mathrm{d}\varphi$ decrease.

When the shrink-fitting ratio $\delta/d = 0$, the displacement increase rate $du_\theta^{P(0)\sim P(2\pi)}(\theta,\varphi)/d\varphi$ is not infinite because the roll is pressed by a pair of loads P which generate the contact pressure at the interface and causing the slip resistance at the contact portion. On the other hand, when $\delta/d \to \infty$, the sleeve and the shaft are integrated together without slippage and therefore $du_\theta^{P(0)\sim P(2\pi)}(\theta,\varphi)/d\varphi \to 0$.

In addition, under the reference value $\delta/d = 0.5 \times 10^{-3}$, the displacement increasing rate $\mathrm{d}u_\theta^{P(0)\sim P(2\pi)}(\theta,\varphi)/\mathrm{d}\varphi = 7.0 \times 10^{-2}$ mm/deg when $T = 3T_m, P = 3P_0$

which is about 70 times larger than $\mathrm{d}u_\theta^{P(0)\sim P(2\pi)}(\theta,\varphi)/\mathrm{d}\varphi = 0.1 \times 10^{-2}$ mm/deg when $T = T_m, P = P_0$. To prevent inner fracture of the sleeve, by using large δ/d care should be taken for the large circumferential stress σ_θ appearing at the inner surface causing the fracture.

3.4.3 Effect of friction coefficient μ on non-uniform slip

The friction coefficient is the main factor as well as the shrink-fitting ratio to prevent interfacial slip. Therefore, in this section, the friction coefficient is changed in the range $\mu = 0.1 \sim 1.0$ including the reference value $\mu = 0.3$. In the expimental study, $\mu = 0.2$ was used between the sleeve inner surface and the shaft outer surface [1]. In addition, $\mu = 0.4$ was reported as a friction coefficient between steels [38]. In this way, the values around $\mu = 0.2 \sim 0.4$ are often used on the sleeve roll joint surface. It is known that among many metals used in steel industries, pure metals have a higher friction coefficient than other alloys. Therefore, the friction coefficient μ should be considered in combination with Armco iron, which can be regarded to be very close to pure iron [40]. Then, the highest friction coefficient can be $\mu = 0.82$ for Armco iron/aluminum combination, $\mu = 0.58$ for Armco iron/nickel, and $\mu = 0.52$ for Armco iron/iron. Therefore, in this study, $\mu = 1.0$ is used as the upper limit of the friction coefficient in a practical sense.

Fig. 3-8 shows the displacement increase rate $\mathrm{d}u_\theta^{P(0)\sim P(2\pi)}(\theta,\varphi)/\mathrm{d}\varphi$ by varying the friction coefficient μ. It can be seen that the displacement increase rate $\mathrm{d}u_\theta^{P(0)\sim P(2\pi)}(\theta,\varphi)/\mathrm{d}\varphi$ decreases with increasing friction coefficient μ regardless of the torque condition. Large shrink-fitting ratio δ/d and large friction coefficient μ can be used to prevent interfacial slippage, although there is a restriction on the range of use. Although large δ/d and large μ may prevent

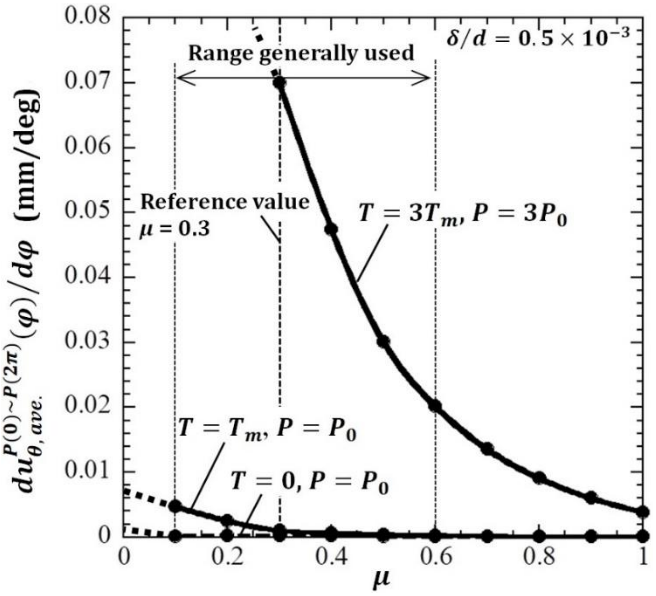

Fig. 3-8 Increase rate of interfacial displacement vs friction coefficient μ when $\varphi = 2\pi$, $T = 0, P = P_0$, $T = T_m, P = P_0$ and $T = 3T_m, P = 3P_0$.

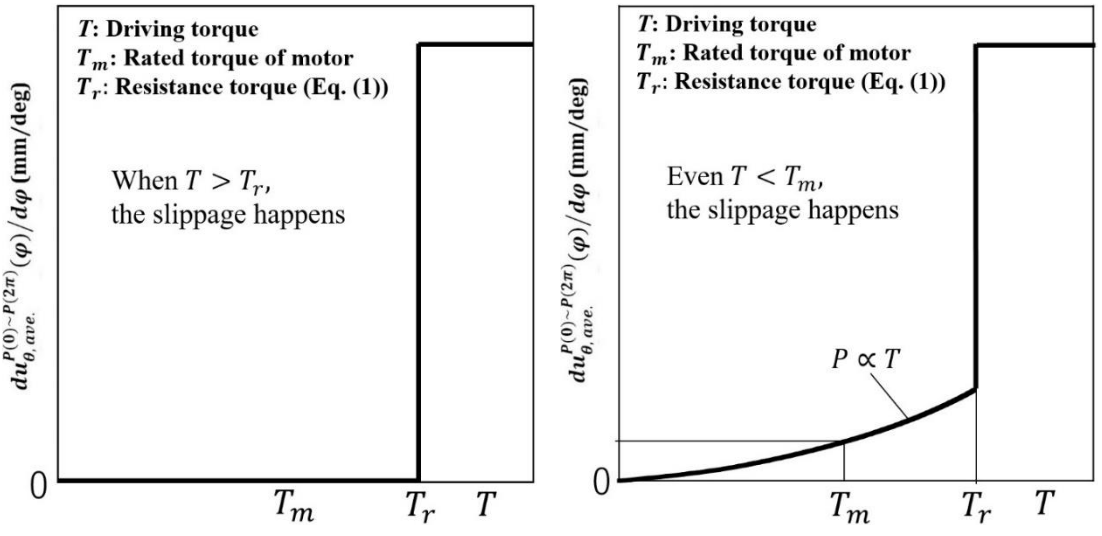

(a) Conventional design concept based on overall slip in sleeve roll.

(b) New design concept based on non-uniform slip in sleeve roll.

Fig. 3-9. Conventional design concept versus new design concept for sleeve roll.

the interfacial slippage, it is difficult to use such δ/d and μ under the rolling trouble $T = 3T_m, P = 3P_0$.

3.4.4 Conventional design concept versus new design concept for sleeve roll

Finally, Fig. 3-9 summarizes the difference between the conventional design concept and the new design concept obtained from the discussion of this paper. As shown in Fig. 3-9(a), the conventional method prescribes $T < T_r$ from Eq. (3-1). Instead, the new method prescribes that the small amount of the interfacial slip may occur even under $T < T_m$. Therefore, based on Fig. 3-9(b), a proper key should be designed to prevent interfacial slip.

3.5 Conclusion for Chapter 3

The shrink-fitted sleeve roll has several advantages. For example, the sleeve wear resistance can be improved independently without loosening the shaft ductility. In addition, the shaft can be reused by replacing the damaged sleeve. In this paper, the FEM simulation was performed to clarify the interfacial slip in real rolling by varying the motor driving torque. To clarify the phenomena, the increase rate of the interfacial displacement was mainly focused. The effects of the shrink-fitting ratio and the effect of the friction coefficient were also considered. The conclusions can be summarized in the following way.

1) The displacement increase rate gradually increases during the initial one rotation and becomes constant after the initial rotation regardless of the amount of motor torque T. In other words, the interfacial slip is unstable during the initial one rotation but becomes stable after that. Therefore, the amount of the interfacial slip can be predicted from the displacement increase

rate because the phenomenon becomes stable after one rotation (see Fig. 3-4).

2) Under the rated motor torque $T = T_m$, the displacement increase rate is about five times larger than the rate under free rolling $T = 0$ (see Fig. 3-4). The acceleration effect of the motor torque T can be explained by the "slippage zone" where the frictional stress and shear stress are equal. The slip zone becomes larger under the rated motor torque $T = T_m$ compared to the one under free rolling $T = 0$ (see Fig. 3-5).

3) With increasing the motor torque T as well as the loading force as $P \propto T$, the displacement increase rate increases significantly (see Fig. 3-6). Under the load conditions T=3T_m and P=3P_0 corresponding to the rolling trouble, the increase rate is 70 times larger than under the standard rolling condition T=T_m and P=P_0 (see Fig. 3-6).

4) The circumferential slippage under free rolling can be explained from the non-uniform deformation due to the loading force P. This is because the displacement increase rate under zero torque increases with increasing the loading force P (see Fig. 3-6(c)).

5) With increasing the shrink fit rate δ/d, the displacement increase rate decreases significantly (see Fig. 3-7). With increasing the friction coefficient μ, the displacement increase rate decreases significantly (see Fig. 3-8). The effect of the motor torque on the elastic shaft is much larger compared to the rigid shaft (see Fig. 3-6(a) and Fig. 3-6(b)).

6) Since the conventional design concept is based on the total slip, a novel design concept based on the non-uniform slip was proposed (see Fig. 3-9(a) and Fig. 3-9(b)).

References for Chapter 3

[1] Shimoda H, Onodera S, Hori K (1966) Study on the residual deflection of large sleeved back-up rolls: 4th Report, Residual stresses of sleeved rolls. Trans. Jpn. Soc. Mech. Eng. 32:689-694.
[2] Tutumi S, Hara S, Yoshi S (1971) The residual deflection of sleeved backup-up rolls. Tetsu-to-Hagane 57(5):818-822.
[3] Noda NA, Sano Y, Takase Y, Shimoda Y, Zhang G (2017) Residual deflection mechanism for back-up roll consisting of shrink-fitted sleeve and arbor. J. JSTP 58:66.
[4] Irie T, Takaki K, Tsutsunaga I, Sano Y (1979) Steel strip and section steel and thick rolling, processing. Tetsu-to-Hagane 65:293.
[5] Takigawa H, Hashimoto K, Konno G, Uchida S (2003) Development of forged high-speed-steel roll for shaped steel. CAMP-ISIJ 16:1150-1153.
[6] Sano Y (1993) Recent advances in rolling rolls. Proc of the No. 148-149 Nishiyama Memorial Technology Course, Tokyo, Japan, 193-226.
[7] Sano Y (1999) Fatigue failure problem in the inside of roll body for hot strip rolling- Crack initiation problem and its estimation in the actual plant. The 245th JSMS Committee on Fatigue of Materials and The 36th JSMS Committee on Strength Design, Safety Evaluation, 40.
[8] Matsunaga E, Tsuyuki T, Sano Y (1998) Optimum shrink fitting ratio of sleeve roll (Strength design of shrink fitted sleeve roll for hot strip mill-1). CAMP-ISIJ, 11:362. https://ci.nii.ac.jp/naid/10002551803.
[9] Spuzic S, Strafford KN, Subramanian C, Savage G (1994) Wear of hot rolling mill rolls: an overview. Wear 176(2):261-271. https://doi.org/10.1016/0043-1648(94)90155-4.
[10] Noda NA, Hu K, Sano Y, Ono K, Hosokawa Y (2016) Residual stress simulation for hot strip bimetallic roll during quenching. Steel Res. Int. 87(11):1478-1488. https://doi.org/10.1002/srin.201500430.
[11] Hu K, Xia Y, Zhu F, Noda NA (2017) Evaluation of thermal breakage in bimetallic work roll considering heat treated residual stress combined with thermal stress during hot rolling. Steel Res. Int. 89(4):1700368. https://doi.org/10.1002/srin.201700368.
[12] Noda NA, Sakai H, Sano Y, Takase Y, Shimoda Y (2018) Quasi-equilibrium stress zone with residual displacement causing permanent slippage in shrink-fitted sleeve rolls. Metals 8(12):998. https://doi.org/10.3390/met8120998.
[13] Sakai H, Noda NA, Sano Y, Zhang G, Takase Y (2019) Numerical simulation on interfacial creep generation for shrink-fitted bimetallic roll. ISIJ Int. 59(5):889-894. https://doi.org/10.2355/isijinternational.ISIJINT-2018-749.
[14] Noda NA, Rafar RA, Sakai H, Zheng X, Tsurumaru H, Sano Y, Takase Y (2021) Irreversible Interfacial Slip in Shrink-Fitted Bimetallic Work Roll Promoted by Roll Deformation. Eng. Fail. Anal. 126:105465. https://doi.org/10.1016/j.engfailanal.2021.105465
[15] Noda NA, Rafar RA, Sano Y (2021) Stress due to interfacial slip causing sleeve fracture in shrink-fitted work roll. International Journal of Modern Physics B, pp 2140020. https://doi.org/10.1142/S0217979221400208
[16] Soda N (1964) Bearing. Iwanami Shoten, Tokyo, pp 196-203.
[17] Imai M (1959) Creep of the roller bearing. Lubrication: Journal of Japan Society of Lubrication Engineers 4(6):307-312.
[18] Murata J, Onizuka T (2005) Generation mechanism of inner ring creep. Koyo Eng. J. 166:41-47.
[19] Niwa T (2013) A creep mechanism of rolling bearings. NTN Tech. Rev. 81:100-103.
[20] Ten, Sakajiri, Takemura, Yukawa (2006) NSK Tech. J. 680:13.

[21] New Bearing Doctor: Diagnosis of bearing problems. Objective: Smooth & reliable operation. NSK (1997). https://www.nsk.com/common/data/ctrgPdf/e7005c.pdf.

[22] Zhan J, Takemura H, Yukawa K (2007) A study on bearing creep mechanism with FEM simulation. Proceedings of IMECE2007, 2007 Seattle, Washington, USA. https://doi.org/10.1115/IMECE2007-41366.

[23] Zhan J, Yukawa K, Takemura H (2009) Analysis of bearing outer ring creep with FEM. Advanced Tribology, 2009, Springer, Berlin, Heidelberg. https://doi.org/10.1007/978-3-642-03653-8_74.

[24] Noguchi S, Ichikawa K (2010) A study about creep between inner ring of ball bearing and shaft. Proceeding of Academic Lectures of the Japan Society for Precision Engineering, 2010, Japan. https://doi.org/10.11522/pscjspe.2010A.0.565.0.

[25] Teramoto T, Sato Y (2015) Prediction method of outer ring creep phenomenon of ball bearing under bearing load. Trans. Of Society of Automotive Eng. of Japan, 46:355-360. https://doi.org/10.11351/jsaeronbun.46.355.

[26] Bovet C, Zamponi L (2016) An approach for predicting the internal behaviour of ball bearings under high moment load. Mech. Mach. Theory 101:1-22. https://doi.org/10.1016/j.mechmachtheory.2016.03.002.

[27] Miyazaki T, Noda NA, Ren F, Wang Z, Sano Y, Iida K (2017) Analysis of intensity of singular stress field for bonded cylinder and bonded pipe in comparison with bonded plate. Int. J. Adhes. Adhes. 77:118-137. https://doi.org/10.1016/j.ijadhadh.2017.03.019.

[28] Noda NA, Miyazaki T, Li R, Uchikoba T, Sano Y, Takase Y (2015) Debonding strength evaluation in terms of the intensity of singular stress at the interface corner with and without fictitious crack. Int. J. Adhes. Adhes. 61:46-64. https://doi.org/10.1016/j.ijadhadh.2015.04.005.

[29] Noda NA, Uchikoba T, Ueno M, Sano Y, Iida K, Wang Z, Wang G (2015) Convenient debonding strength evaluation for spray coating based on intensity of singular stress. ISIJ Int. 55(12):2624-2630. https://doi.org/10.2355/isijinternational.ISIJINT-2015-458.

[30] Wang Z, Noda NA, Ueno M, Sano Y (2016) Optimum design of ceramic spray coating evaluated in terms of intensity of singular stress field. Steel Res. Int. 88:1-9. https://doi.org/10.1002/srin.201600353.

[31] Noda NA, Chen X, Sano Y, Wahab MA, Maruyama H, Fujisawa R, Takase Y (2016) Effect of pitch difference between the bolt-nut connections upon the anti-loosening performance and fatigue life. Mater. Des. 96:476-489. https://doi.org/10.1016/j.matdes.2016.01.128.

[32] Noda NA, Takaki R, Shen Y, Inoue A, Sano Y, Akagi D, Takase Y, Galvez P (2019) Strain rate concentration factor for flat notched specimen to predict impact strength for polymeric materials. Mech. Mater. 131:141-157. https://doi.org/10.1016/j.mechmat.2019.01.011.

[33] Matsuda S, Suryadi D, Noda NA, Sano Y, Takase Y, Harada S (2013) Structural design for ceramics rollers used in the heating furnace. Trans. JSME Ser. A 79(803):989-999.

[34] Noda NA, Suryadi D, Kumasaki S, Sano Y, Takase Y (2015) Failure analysis for coming out of shaft from shrink-fitted ceramics sleeve. Eng. Fail. Anal. 57:219-235. https://doi.org/10.1016/j.engfailanal.2015.07.016.

[35] Noda NA, Xu Y, Suryadi D, Sano Y, Takase Y (2016) Coming out mechanism of steel shaft from ceramic sleeve. ISIJ Int. 56(2):303-310. https://doi.org/10.2355/isijinternational.ISIJINT-2015-558.

[36] Zhang G, Sakai H, Noda NA, Sano Y, Oshiro S (2019) Generation mechanism of driving out force of the shaft from the shrink fitted ceramic roll by introducing newly designed stopper. ISIJ Int. 59(2):293-299.

https://doi.org/10.2355/isijinternational.ISIJINT-2018-615.

[37] Marc Mentat team (2008) Theory and User Information, Vol. A, MSC, Software, Tokyo, 713.

[38] Misumi-vona Top, Technical information, Dry coefficient of friction. https://jp.misumi-ec.com/tech-info/categories/plastic_mold_design/pl07/c0874.html Accessed 20 July 2020

[39] Hot Strip Subcommittee of Joint Study Group of Steel Sheet Subcommittee in The Iron and Steel Institute of Japan: Recent hot strip manufacturing technology in Japan (Report of Hot Strip Subcommittee of Joint Study Group of Steel Sheet Subcommittee), Ibaraki Print (1987), 255.

[40] JSME (2004) Mechanical Engineering Handbook a2 Mechanical Mechanics, JSME, pp27.

4 Experimental study to verify the interfacial slip

4.1 Introduction

In steel manufacturing industries, rolling process produces more tonnage than any other metalworking processes [1-20]. Among the rolls used in steel rolling, instead of a solid roll, is a sleeve assembly type roll which was developed by shrink-fitting the shaft into the sleeve. Some of them are successfully and practically used as a back-up rolls with a large body diameter exceeding 1000 mm and large H-shaped steel rolling rolls [1-3]. The sleeve assembly roll has several advantages, where the shaft can be reused by replacing the worn sleeve and; next generation rolls such as a super cermet roll can be manufactured only as a sleeve roll. Several peculiar problems have been solved through previous studies such as residual roll bending and sleeve cracking due to the circumferential sleeve slip [4-8]. Among them, the circumferential sleeve slip is a very severe one. This is because a “non-uniform sleeve slip” still occurs even when the rolling is designed in a condition that “the overall slip” does not happen as the motor torque is applied to the roll [7, 8]. There are only a few studies that treated the interfacial slip quantitatively for the non-uniform slip behavior in the sleeve roll. This research highlights a similar slip phenomenon which is known to exist in ball/roller bearing named “an interface creep phenomenon”, where the slip occurs between the shaft and the inner race as well as between the housing and the outer race [21-33].

In a previous study, a numerical simulation was performed for the interfacial slip under free rolling conditions while considering the work roll of 4-high rolling mill (see Fig. 4-1(a)) [16]. Consequently, it was found that an interfacial slip can be expressed from the accumulation of a non-uniform slip in the circumferential direction. After confirming the interfacial slip under free

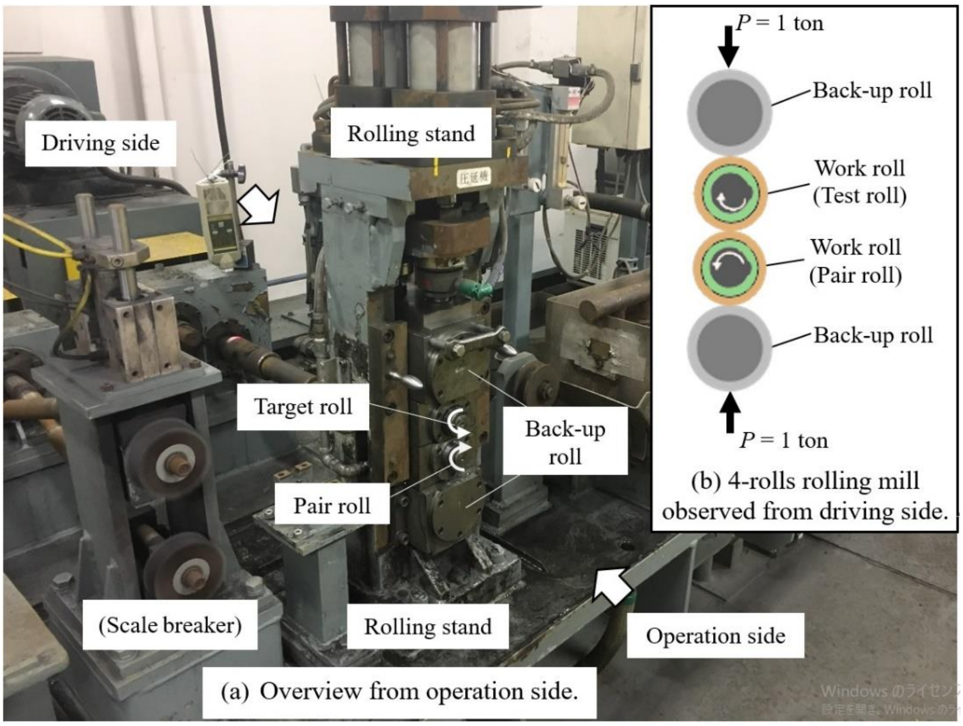

Fig. 4-1 Miniature rolling mill whose size is about 1/10 of the real rolling mill.

rolling, the effect of the motor torque on the slip was investigated. It was found that the slip was accelerated largely by the motor torque [17]. On top of this, the effects of elastic shaft deformation, shrink-fitting ratio and friction coefficient were also studied [18, 19]. In those studies, the slip acceleration was explained from the slip region and the low stress region at the interface although a detailed experimental verification has not been performed yet for the interfacial slip in rolling roll [16-19].

In this paper, a rolling experiment was conducted to confirm the circumferential slip experimentally. Fig. 4-1 illustrates a miniature rolling mill with a size of approximately 1/10 from the real rolling mill. Since a similar phenomenon is known as an interface creep in ball/roller bearing, the slip will be verified under free rolling. Note that, even when there is no shrink-fitting of δ/d =0, the sleeve and the shaft managed to be in contact with each other due to the load P in Fig. 4-1. Hence, the shrink-fitting ratios of $\delta/d = 0$ and

$\delta/d = 0.21 \times 10^{-3}$ are considered in this study.

4.2 Experimental verification of interface slips by using a miniature rolling mill

4.2.1 Experimental conditions and methods

Table 4-1

Specifications of the miniature roll testing machine.

Roll size	
Buck-up roll size (Body diameter $D_B \times$ Body length) (mm)	120×40
Buck-up roll material	SCM440 Quenched and tempered
Work roll size (Body diameter $D_B \times$ Body length) (mm)	60×40
Specification	
Load P (ton)	~10
Rotating speed (rpm)	1150
Driving system	Work roll drive (Two rolls / One motor)
Driving motor	Speed 3-phase induction motor
Power (kW), Pulse speed (Hz)	55, 59.2
Voltage (V), Current (A)	180, 225
Coil tension force (MPa)	100~1000
Coolant: Front (L/min), Back	~1.0, ~4.5
Rolled coil size (mm), Material	$1 \times 15 \times (250 \times 10^3)$ (Thickness×Width×Length), Steel

Fig. 4-1(a) shows a hot rolling mill testing machine that was developed by Hitachi Metals. Table 4-1 shows the specifications of the miniature roll testing machine [34]. This testing machine is used to evaluate surface roughness and weariness of the work roll by passing the hot coil between the upper and lower work rolls. However, in this research, a pair of the work rolls are driven by a direct contact without the passing of hot coil to realize the slip under free rolling. Fig. 4-1(b)

Table 4-2
Test work roll specifications (see Fig. 4-3(b)).

Specifications	
Size $D,\ d,\ d_1$ (mm)	60, 48, 35
Material	SCM440 Quenched and tempered
Tensile strength σ_B (N/mm^2)	980
Hardness HB	Sleeve: 280~300 Shaft: 305~330

Table 4-3
Experimental conditions.

Test roll		
Shrink fitting ratio δ/d	Roll A	0
	Roll B	0.21×10^{-3}
Driving condition		
Test roll		Free rolling.
Pair roll		Driven by the torque 457 Nm.
Load P (ton)		1.0
Rotating speed (rpm)		106~212
Roll cooling: Front side (L/min), Back side		Water 0.25, 2.0
Roll temperature (℃): $\delta/d = 0.21 \times 10^{-3}$, 0		16.0~21.0
Number of rotation, n		Rotations until sleeve slip

illustrates the roll configuration and the position of the test roll in the rolling stand from the driving side. In this experiment, the upper work roll is the target roll without any driven state. The target work roll is driven by the contact force from the lower pair roll and also in touch with the upper back-up roll, which is supported by a roller bearing. Note that, the contact effect of the back-up roll is small and negligible. The target roll has a double shaft structure whereby the inner and the outer shafts are fixed with a key to realize the circumferential slip at the shrink-fitting interface between the sleeve and the outer shaft (see Fig. 4-3(c)). SCM440 material was used for both the sleeve as well as the shaft.

Table 4-2 shows the specifications of the test work roll. The diameter of

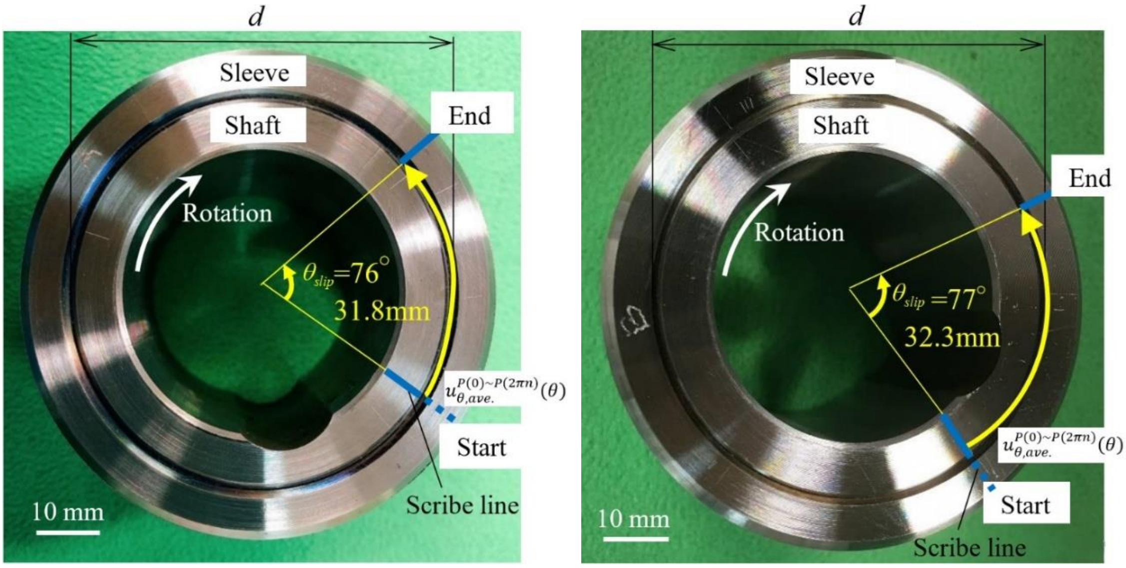

(a) Roll A of $\delta/d = 0$ at $\mathrm{n} = 1 \times 10^4$.

(b) Roll B of $\delta/d = 0.21 \times 10^{-3}$ at $\mathrm{n} = 3 \times 10^4$.

Fig. 4-2 Slipped target roll in miniature rolling mill in Fig. 4-1 observed from driving side ($u_{\theta,ave.}^{P(0)\sim P(2n\pi)}(\theta) = u_{\theta,Sleeve}^{P(0)\sim P(2n\pi)}(\theta) - u_{\theta,Shaft}^{P(0)\sim P(2n\pi)}(\theta)$, n = number of rotation).

the test roll is about 1/10 of the diameter of the real roll. Table 4-3 displays the experimental conditions. Roll A denotes the roll without the shrink-fitting ratio of $\delta/d = 0$ and roll B denotes the roll with the shrink-fitting ratio of $\delta/d = 0.21 \times 10^{-3}$. In the experiment, the work roll was cooled down by water at room temperature to prevent the changing of the shrink-fitting ratio due to a rising temperature. When the steady rotation speed reached 106 rpm or 212 rpm, a load of 1 ton was applied to ensure that the temperature change of the roll surface was within 5℃ or less during the experiment by a contact thermometer.

4.2.2 Experimental results for interface slip

Fig. 4-2(a) illustrates the slip status of roll A specimen with no shrink-fitting of $\delta/d = 0$. The slip distance $\ell_s = \pi d\theta_{slip}/360$ can be obtained as

Table 4-4
Experimental results of relative slip distance.

Shrink-fitting ratio δ/d	Relative slip distance $\ell_s = \frac{\pi d\theta_{slip}}{360}$ (mm)	Number of rotation $n_t - n_0$	Relative displacement $\frac{\pi d\theta_{slip}}{360(n_t-n_0)}$ (mm/rev.)	Displacement increase rate $\frac{\pi d\theta_{slip}}{360^2(n_t-n_0)}$ (mm/deg.)
Roll A $\delta/d = 0$	31.8	1×10^4	3.18×10^{-3}	8.84×10^{-6}
Roll B $\delta/d = 0.21 \times 10^{-3}$	32.3	3×10^4	1.08×10^{-3}	2.99×10^{-6}

relative circumferential movement from the scribed lines as shown in Fig. 4-2(a), before and after the experiment. The slip angle $\theta_{slip} = 76°$ specifying the slip distance $\ell_s = \pi d\theta_{slip}/360 = 31.8$ mm which occurs after the number of the roll rotation $\mathrm{n} = 1 \times 10^4$. Fig. 4-2(b) illustrates the slip status of roll B specimen of $\delta/d = 0.21 \times 10^{-3}$. Fig. 4-2(b) shows the slip angle $\theta_{slip} = 77°$ specifying the slip distance $\ell_s = \pi d\theta_{slip}/360 = 32.3$ mm which occurs after the number of the roll rotation $\mathrm{n} = 3 \times 10^4$.

In the previous study, the numerical simulation was performed to realize the circumferential slip in shrink-fitting sleeve roll (see Appendix A.1). The rotation of the roll was replaced by load shifting $P(0){\sim}P(\varphi)$ with load shift angle φ on a fixed roll surface. Afterwards, the interfacial displacement $u_\theta^{P(0)\sim P(\varphi)}(\theta)$ in the θ-direction was obtained [16-19]. In the next section, the notation $u_\theta^{P(0)\sim P(\varphi)}(\theta)$ is illustrated as shown in Fig. 4-4. For instance, when the number of roll rotation is n, the non-uniform slip can be expressed as $u_\theta^{P(0)\sim P(2n\pi)}(\theta)$ by putting $\varphi = 2n\pi$. Since $u_\theta^{P(0)\sim P(\varphi)}(\theta)$ slightly varies depending on θ, the average value $u_{\theta,ave.}^{P(0)\sim P(2n\pi)}$ was defined in the previous paper as shown in Eq. (4-1) (see

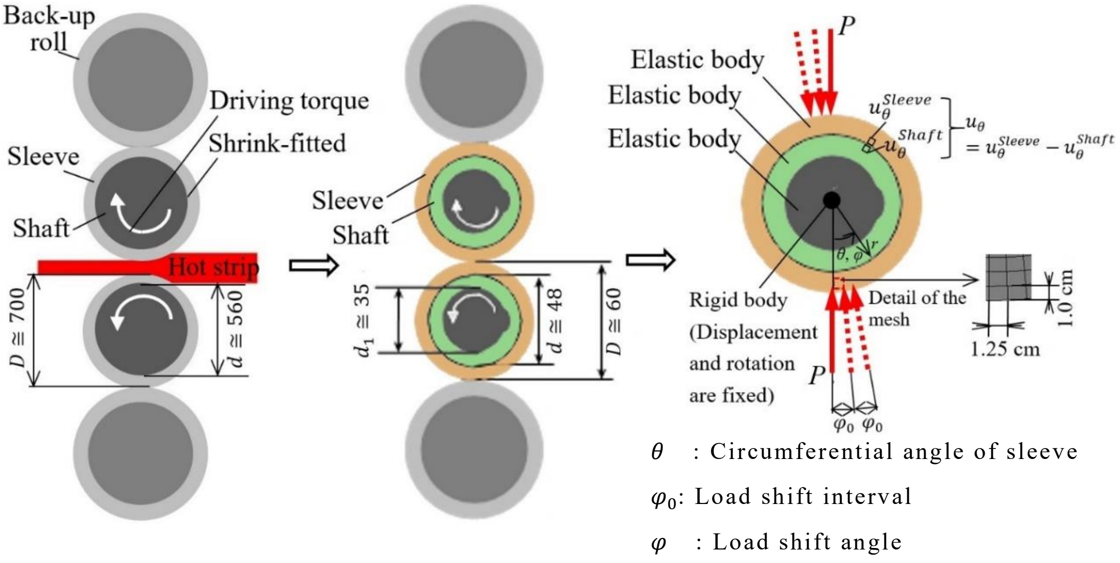

(a) Real roll at the central cross-section (b) Miniature roll (c) Work roll modeling

Fig. 4-3 Schematic illustration for (a) Real roll at the central cross-section, (b) Miniature roll and (c) Work roll modeling.

Fig. A-2).

$$u_{\theta,ave.}^{P(0)\sim P(\varphi)} = \frac{1}{2\pi}\int_0^{2\pi} u_\theta^{P(0)\sim P(\varphi)}(\theta)d\theta \tag{4-1}$$

This average displacement is corresponding to the slip distance per rotation $\pi d\theta_{slip}/(360 \cdot n)$ as shown in Eq. (4-2). The average displacement per rotation $u_{\theta,ave.}^{P(0)\sim P(2n\pi)}/n$ is corresponding to the experimental value $\pi d\theta_{slip}/(360 \cdot n)$ as shown in Eq. (4-2).

$$u_{\theta,ave.}^{P(0)\sim P(2n\pi)}/n = \frac{\theta_{slip}\pi d}{360 \cdot n} \tag{4-2}$$

In the numerical simulation, the displacement increase rate $du_{\theta,ave}^{P(0)\sim P(2n\pi)}/d\varphi$ was highlighted as well. In particular, it was found that $du_{\theta,ave}^{P(0)\sim P(2n\pi)}/d\varphi$ becomes almost constant after one rotation of the roll. The displacement increase rate $du_{\theta,ave}^{P(0)\sim P(2n\pi)}/d\varphi$ can be expressed experimentally as similar as the slip distance

Table 4-5

Analytical condition in the miniature roll

	Property	
Sleeve	Young's modulus of steel sleeve E (GPa)	210
	Poisson's ratio of steel sleeve v	0.28
Shaft	Young's modulus of shaft E_s (GPa)	210
	Roll size	
Outer diameter of sleeve D (mm)		60
Inner diameter sleeve d (mm)		48
	Shrink-fitting	
Shrink-fitting ratio δ/d		0.21×10^{-3}
Friction coefficient between sleeve and outer shaft μ		0.3
	External force	
Concentrated load per unit width P (N/mm)		245 (Total: 1 ton, Rolled width: 40 mm)
Frictional force per unit width S (N/mm)		0
Bending force from bearing P_b (Nm/mm)		0

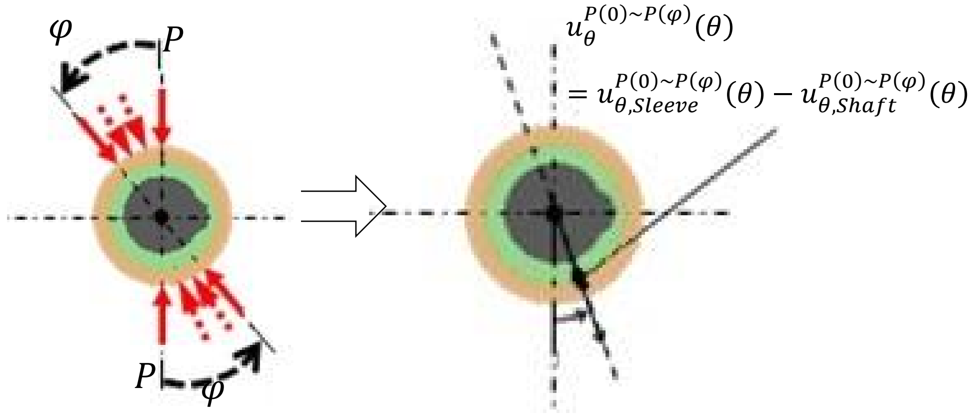

(a) Define the pair of the loads shift from $\varphi = 0$ to φ, and $\varphi = \pi$ to $(\pi + \varphi)$ as $P(0) \sim P(\varphi)$.

(b) Define the displacement $u_\theta(\theta)$ due to $P(0) \sim P(\varphi)$ as $u_\theta^{P(0)\sim P(\varphi)}(\theta)$.

Fig. 4-4 Definition of the relative displacement $u_\theta^{P(0)\sim P(\varphi)}(\theta)$ due to the shifted load $P(0)\sim P(\varphi)$ for the miniature roll specimen in Fig. 3.

per degree shown in Eq. (4-3).

$$du_{\theta,ave.}^{P(0)\sim P(2n\pi)}/d\varphi = \frac{\theta_{slip}\pi d}{360\cdot 360n} \tag{4-3}$$

Note that Eqs. (4-2) and (4-3) are assumed under the condition where the slip occurs consistently during the roll rotation. Table 4-4 shows the slip distance per rotation $\pi d\theta_{slip}/(360\cdot(n_t-n_0))$ (mm/rev.) and the slip distance per degree $\pi d\theta_{slip}/(360^2\cdot(n_t-n_0))$ (mm/deg.). Here, the slip angle after the experiment is represented by θ_{slip}, the roll diameter is represented by d, and the number of rotations is represented by n. From Table 4-4, it is found that both of the slip distance $\pi d\theta_{slip}/(360\cdot(n_t-n_0))$ and $\pi d\theta_{slip}/(360^2\cdot(n_t-n_0))$ of roll A are nearly three times larger than the ones of roll B.

4.3 Numerical simulation for an interfacial slip in the miniature roll

4.3.1 Outline of numerical simulation of numerical simulations

Figs. 4-3(a) and 4-3(b) illustrate the central cross-section of the real roll in comparison with the central cross-section of the miniature roll. Fig. 4-3(c) shows the load shifting method to realize the slip. In the miniature sleeve roll in Fig. 4-3(b), the inner shaft and the outer shaft are fixed by using a key so that the slip does not occur at the interface. Instead, the outer shaft and the sleeve are assembled by shrink-fitting so that the interfacial slip may be realized. In a real roll, in order to meet the demand for the high wear resistance and high toughness, bimetallic sleeve is commonly used for the rolling roll. Therefore, wear-resistant material such as high-speed steel or high-chrome steel is used for the outer layer, and alloy steel is used for the inner layer. In the miniature roll experiment, however, a steel sleeve and a steel shaft are used. Table 4-5 shows the detail of the sleeve properties, inner and outer shafts, as well as the keys. As shown in Fig.

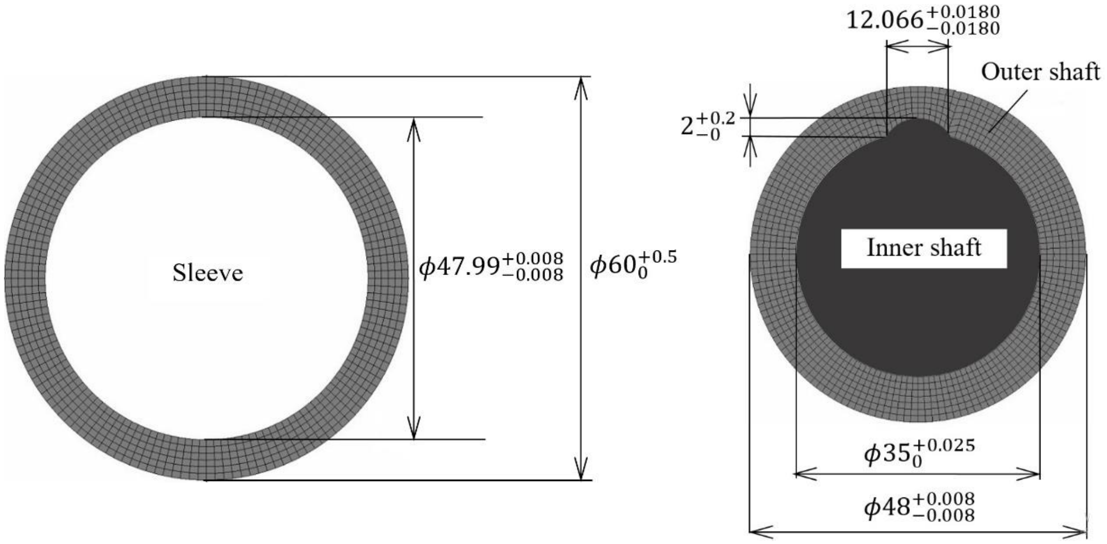

(a) Sleeve (b) Shaft

Fig. 4-5 Test specimen when $\delta/d = 0.21 \times 10^{-3}$.

4-3(c), the roll rotation is fixed by introducing a rigid body at the roll center.

Fig. 4-4 illustrates the relative displacement $u_\theta^{P(0)\sim P(\varphi)}(\theta)$ due to the shifted load $P(0)\sim P(\varphi)$ in Fig. 4-3. As shown in Appendix A.1 [16-19], the load shifting method is applied to investigate the non-uniform slip for the miniature roll specimen. In this study, to clarify the interfacial slip generation, free rolling is applied to both work roll and back-up roll. Presumably, the shaft rotation torque $T = 0$ and the frictional force which is due to the rolled material $S = 0$. Fig. 4-5 shows the FEM mesh with the dimension for the target roll having a double shaft structure whereby the inner shaft and the outer shafts are fixed with a key so that the slip may appear only at the shrink-fitted interface between the sleeve and the outer shaft. SCM440 material is used for both of the sleeve and the shaft. In this analysis, similar to the miniature roll experiment, the load $P =$ 245 N/mm is applied from the back-up roll to the sleeve as well as the reaction force from the rolled plate to the sleeve [18]. The shrink-fitting ratio is defined as δ/d which is composed from the shrink-fitting allowance δ and the inner diameter d. Here, $\delta/d = 0.21 \times 10^{-3}$ is used in the miniature roll analysis. The friction coefficient between the sleeve and the outer shaft is $\mu = 0.3$. In the manufacturing procedure, firstly, the inner diameter of the sleeve is machined, and the shaft is shrink-fitted into the sleeve. Secondly, the inner diameter of the shaft is machined including the keyway. Finally, the inner shaft is fixed into the inner diameter by the key. The tightening allowance is $\delta = 0\,\text{mm}$ for roll A and $\delta = 0.01\,\text{mm}$ for roll B. The shrink-fitting ratios are $\delta/d = 0$ and $\delta/d = 0.21 \times 10^{-3}$ for roll A and roll B respectively.

4.3.2 Comparison of slip distance obtained by the analysis and the experiment

Table 4-6 summarizes the average value of the displacement $u_{\theta,ave.}^{P(0)\sim P(2n\pi)}$ which is the slip distance in the experiment, as well as the displacement increase rate $du_{\theta,ave.}^{P(0)\sim P(2n\pi)}/d\varphi$ that was obtained by several simulations and experiments. The simulation results in Table 4-6 are based on the results where the slip appears at the same time when the roll rotation starts, and consistently appears throughout the roll rotation without causing the slip defect. From Table 4-6, it is seen that the simulation results are 3.6~4.3 times larger than the experimental results. This gap is due to a constant friction coefficient $\mu = 0.3$ that was assumed in the simulation, even though the friction coefficient is kept changing with $\mu = 0.3\sim\infty$ throughout the experiment because of the growth of the slip defect. Although the results are comparatively larger, the current simulation can still be used for comparative purposes. For example, both experiment and numerical simulation showed that the results under no shrink-fitting of $\delta/d = 0$ is 2.79~3.53 times larger than the results of $\delta/d = 0.21 \times 10^{-3}$. The following section explains the slip defect observed in the sleeve and shaft surfaces that are studied

Table 4-6

Comparison of displacement increase rate and relative displacement between experiment and simulation.

Shrink-fitting ratio δ/d	Displacement increase rate $\frac{du_{\theta,ave.}^{P(0)\sim P(2n\pi)}}{d\varphi} = \frac{\pi d\theta_{slip}}{360^2(n_t - n_0)}$ (mm/deg.)		Relative displacement $u_{\theta,ave.}^{P(0)\sim P(2n\pi)} = \frac{\pi d\theta_{slip}}{360(n_t - n_0)}$ (mm/rev.)	
	Experiment (mm/deg.)	Simulation (mm/deg.)	Experiment (mm)	Simulation (mm)
Roll A $\delta/d = 0$	0.884×10^{-5}	3.074×10^{-5}	0.318×10^{-2}	1.356×10^{-2}
Roll B $\delta/d = 0.21 \times 10^{-3}$	0.299×10^{-5}	1.103×10^{-5}	0.108×10^{-2}	0.384×10^{-2}

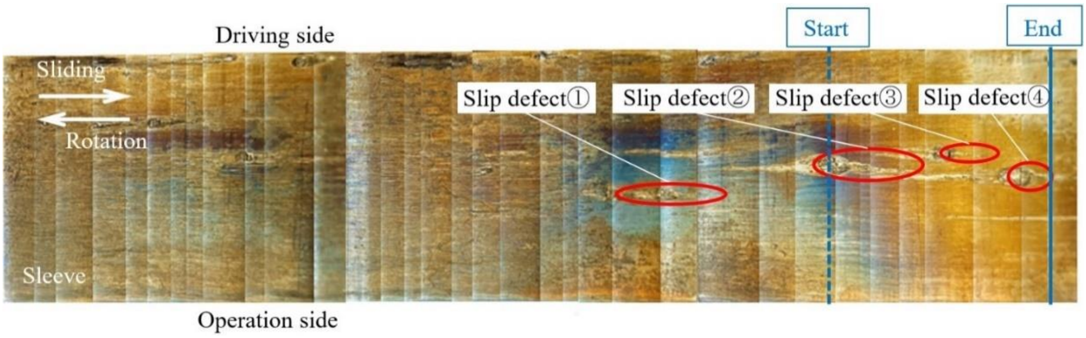

(a) Sleeve surface of roll B, $\delta/d = 0.21 \times 10^{-3}$.

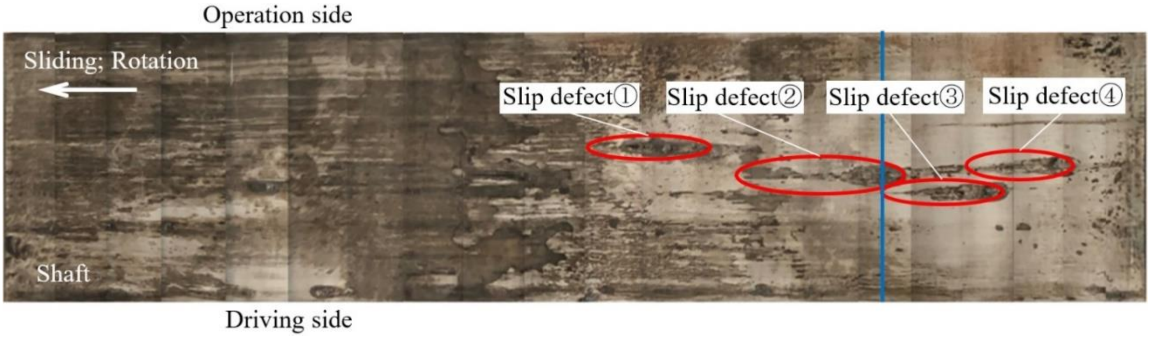

(b) Shaft surface of roll B, $\delta/d = 0.21 \times 10^{-3}$.

Fig. 4-6 Slip defects denoted by ①, ②, ③, ④ observed on the (a) sleeve surface and (b) shaft surface.

comprehensively.

4.4 Slip defects caused by an interfacial slip in miniature roll

4.4.1 Observation on the sleeve surface

A detailed observation was performed for the damaged surface of roll B with $\delta/d = 0.21 \times 10^{-3}$ since the real sleeve roll is shrink-fitted. Fig. 4-6 shows the entire circumferential surfaces of (a) the inner surface of the sleeve and (b) the outer surface of the outer shaft (hereinafter referred to as the shaft). Four slip defects are denoted by ①, ②, ③, ④. Here, the slip defect ② is focused since the defect size ② is relatively larger.

Fig. 4-7 illustrates the enlarged views of the slip defect ② in Fig. 4-6(a). As indicated in Fig. 4-7(a), the entire defect can be classified into several regions. To express the characteristic of those regions, the term “slip defect” is used for the entire region. On the other hand, the term “scratch” is used only at the earliest region. Moreover, the term “an ellipsoidal defect” is used at the end of the region. At the starting point of the defect in Fig. 4-7(a), some scratches with intermittent white lines are seen along with a pitch corresponding to the feed amount of the tool. Then, the slip defect is developed by erosion wear and cohesive wear during the rolling. Finally, the slip defect forms a comparatively larger ellipsoidal defect at the end of the defect since the slip is stopped.

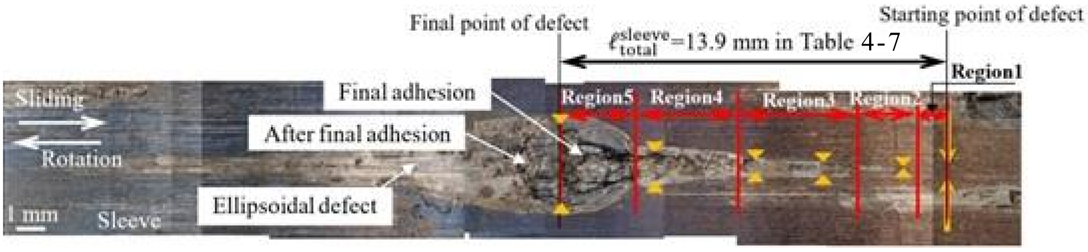

(a) Slip defect ② which can be classified into Region 1~Region 5 on the sleeve surface.

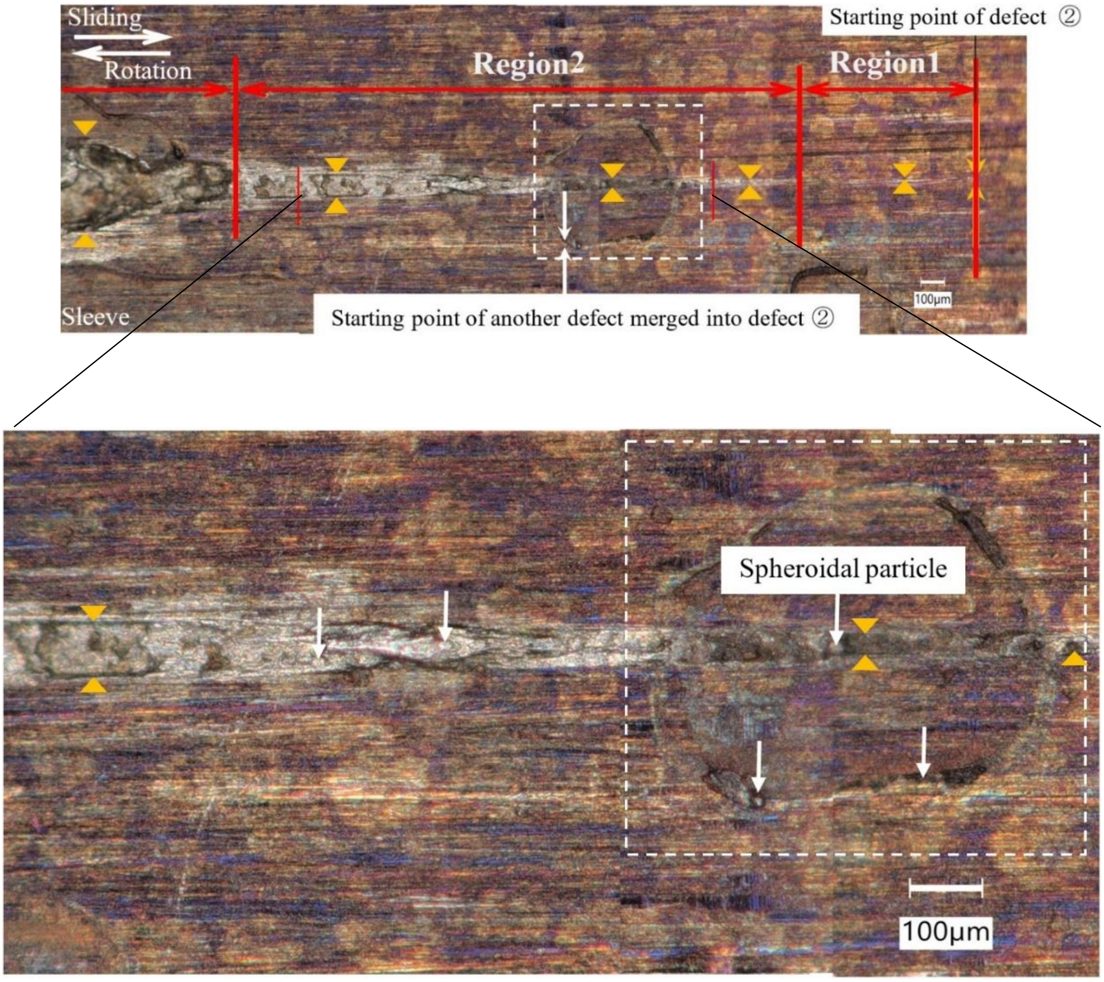

(b) Enlarged view of Region 2 of slip defect ② on the sleeve surface.

In this way, the defect growing process can be classified into Region 1 ~ Region 5. Firstly, as shown in Fig. 4-7(b), Region 1 includes intermittent white lines caused by scratch wear. Due to the high-pressure contact at the top of the machined surface, the slip defect starts with the scratch at the top of roughness as arcuate protrusions. Secondly, in Region 2 in Fig. 4-7(b), those grooves between the white lines merge into a thick linear defect repetitively and gradually become thicker and glossy blackish grooves. From the analysis, this linear groove is formed due to the combined actions of the scratch wear, the adhesive wear, and the erosive wear. As shown in the enlarged view in Fig. 4-7(b), spheroidal

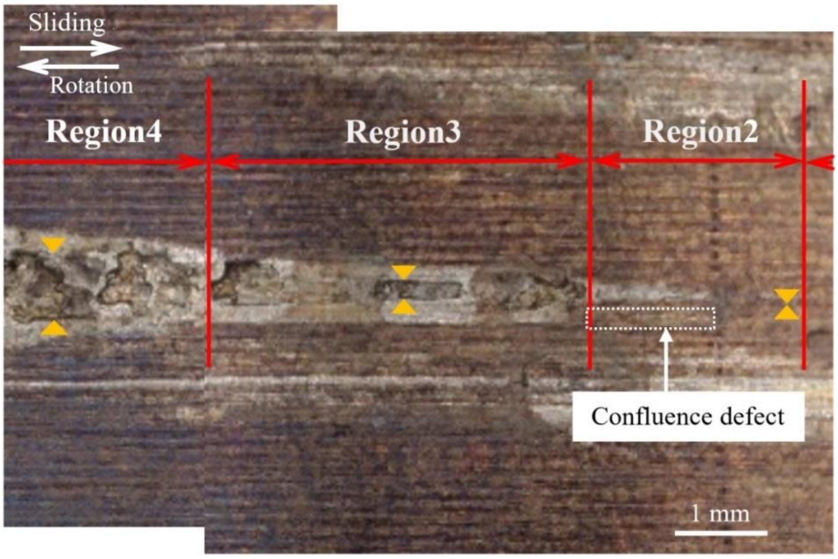

(c) Enlarged view of Region 3 of slip defect ② on the sleeve surface.
(Another slip defect to be united can be seen in Region 2.)

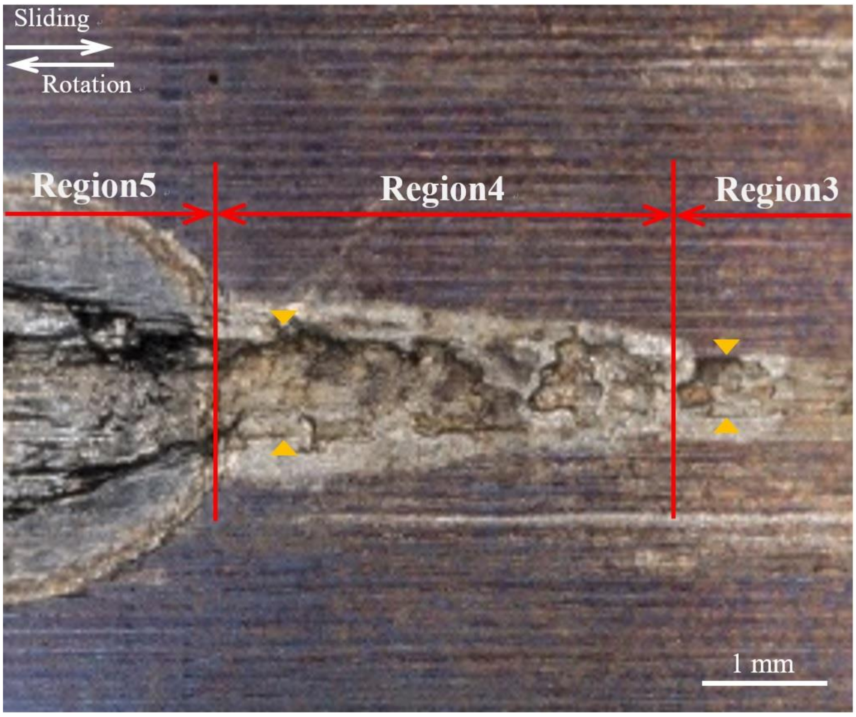

(d) Enlarged view of Region 4 of slip defect ② on the sleeve surface.

particles can be seen in the grooves. This is a characteristic phenomenon that occurs when a slip is repeatedly applied under high-pressure, and is also a

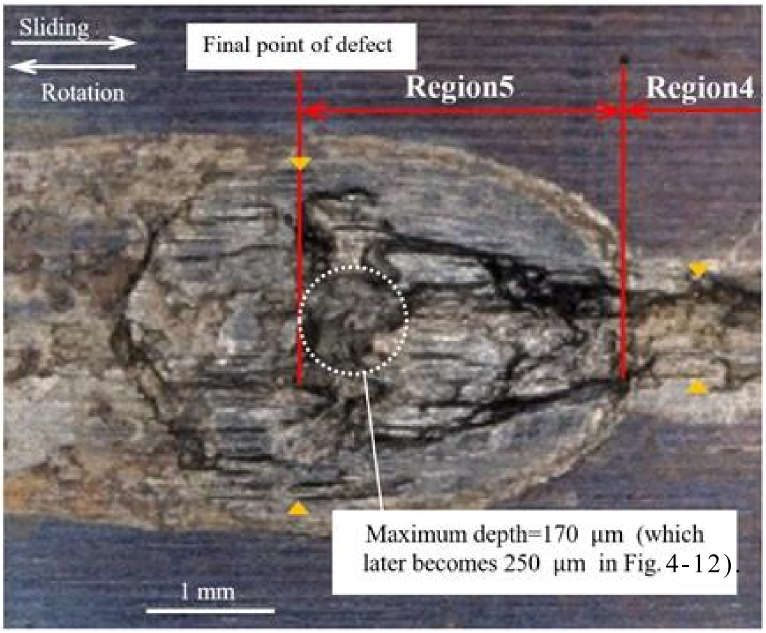

(e) Enlarged view of Region 5 of slip defect ② with the maximum depth 250 μm on the sleeve surface. (The semicircular region at the left front of Region 5 was originally a normal wear surface and changed to the slip defect like surface after a certain period of non-slip).

Fig. 4-7 Slip defect ② whose whole region can be classified into Region 1~Region 5 on the sleeve surface.

characteristic of the adhesion wear phenomenon [37]. The spherical particles are in a strong bonded state because the wear debris sticks and adheres to each other by reciprocating motion under high-pressure. In the middle of Region 2, an elliptical shaped defect with black fragmentary grooves surrounded by white dashed line frame can be seen in Fig. 4-7(b). This is a trace formed during the period when the slip was stopped for a relatively long time. More details will be shown in the upcoming Region 5 since a similar elliptical defect is seen in Region 5. In Region 3, Fig. 4-7(c) portrays the width of the defect that becomes larger. This width extension is caused by the coalescence of another slip defects as shown in Fig. 4-7(c). Fig. 4-7(d) shows that, Region 4 includes irregular shaped grooves during the defect’s width growth, unlike from other regions previously described. It may be conjectured that those irregular shaped grooves were caused by an erosive wear affected by the loss of the slip direction as the slip speed becomes slower. Note that there are signs of erosive wear existed even before Region 3.

Fig. 4-7(e) shows the Region 5 part where the slip eventually remained. It is seen that the defect has reached the maximum depth, which will be further described later in Fig. 4-12. This state including the maximum depth can be regarded as the final point of the defect. At this position, due to the stopping of the slip, cohesive wear occurs throughout the entire Region 5. Therefore, in Region 5, the cohesive particles are less likely to be discharged. Furthermore, due to the repetition of the compressive force acting at each rotation, the adhesion of wear products progresses mainly inside the groove. At the same time, the slippage stops due to an increase in slip resistance which is caused by the widening of the groove. A slope is observed at the final position of Region 5. After a certain period of non-slip phenomenon, an elliptical trace of the entire Region 5 is formed in a similar way as the ellipse generation in Region 2. The reason behind the forming of this trace can be explained in the following way. The cooling water drawn into the widened black groove is diffused to the surroundings during compression, and the cooling water is drawn in after decompression. This action is repeated for each roll rotation. Due to the repeated compressive force, the inside surface of the black groove began to crush. On top of that, the cohesive wear of the crushed particles inside of the black groove occurs in the depth direction and progresses to the deepest direction. Several irregular shapes which were formed due to the crush led to the increase in generating a gap between the sleeve and shaft, and preventing the contact by the apparent volume of the cohesive particles. With the increase in the distance from the groove, the gap becomes smaller, and a contact condition is formed where the short radius is 1.7 mm from the elliptical trace (on the outer circumference of the elliptical trace). Eventually, the elliptical erosive groove is formed at the contact portion due to the inflow and outflow of high-pressure and high-speed water.

In Fig. 4-7(e), the semicircular area at the left front of Region 5 was originally a normal wear surface with no defect when the slippage stopped. However, it was then changed to the slip defect like surface after a certain period of non-slip. The surface change is caused by an accumulation of the erosive wear and adhesion wear due to the drawing in and out of the cooling water under repeated compressive force. A similar pattern can be seen in Region 5 on the shaft surface.

4.4.2 Observation on the shaft surface

Fig. 4-8(a) illustrates the enlarged views of slip defect ② in Fig. 4-6(b) on the shaft surface. As indicated in Fig. 4-8(a), the entire defect on the shaft is classified into Region 1 ~ Region 5, which is similar to Fig. 4-7(a) on the sleeve. From Fig. 4-8(a), it can be seen that Region 1 contains worm-eaten like erosive wear and intermittent white lines indicating scratch wear. In addition, the discoloration range that looks like an oxide film is partially widened. In Region 2, although it is quite unclear, a series of continuous grooves can be seen and the width is gradually increasing. The groove is shallow, and white flakes are scattered on the bottom of the groove, and the boundary of the grooves is also unclear. In Region 3, the groove width is further widened, and no difference can be seen between the state where white flakes are scattered and its surroundings. In Region 4, as shown in Fig. 4-8(b), the groove width suddenly expands. The inner

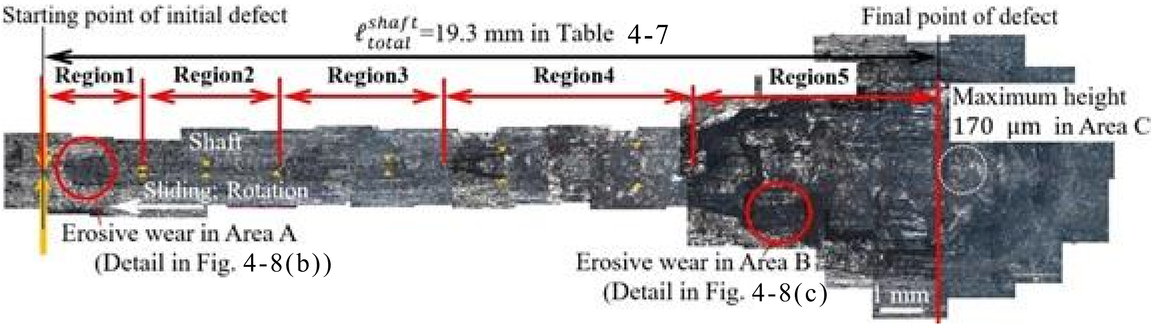

(a) Slip defect ② on the shaft surface consisting of Region 1~Region 5.

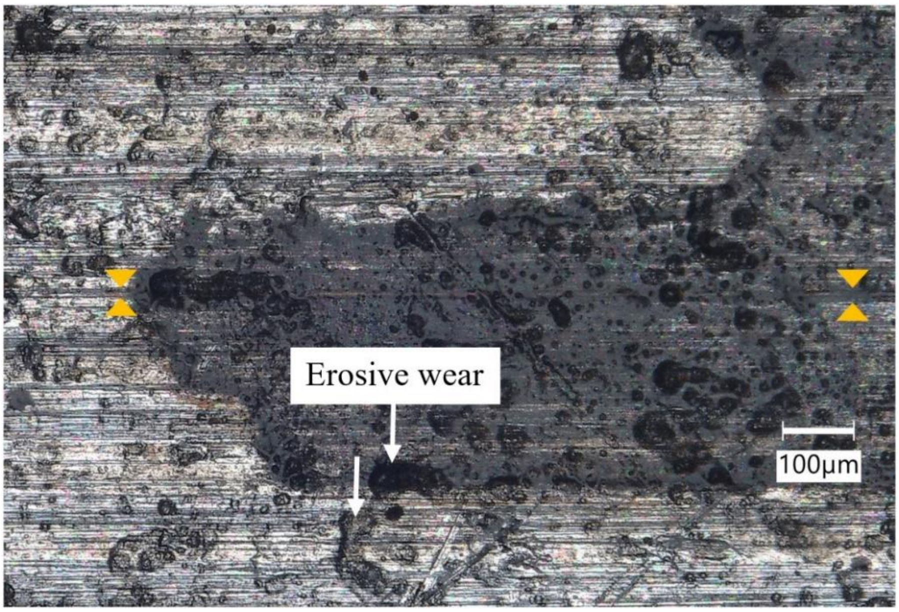

(b) Erosive wear in Area A in Region 1 of slip defect ②.

surface is blackish and glossy, and the partial boundary becomes clear. Nonetheless, glossy grooves with worm-eaten like erosive wear can also be seen irregularly, and the partial groove boundary is unclear. Region 5 is where the slip eventually stopped, and the position of the stop end coincides with the sleeve. Similar to the sleeve, an elliptical shape trace can be seen around the boundary (see Figs. 4-8(a) and 4-8(b)). During non-slip, due to the repeated contact, worm-eaten like erosive wear spreads further as shown in Fig. 4-8(c). Compared to Region 3, white flakes in Region 5 are also observed. Although they are not

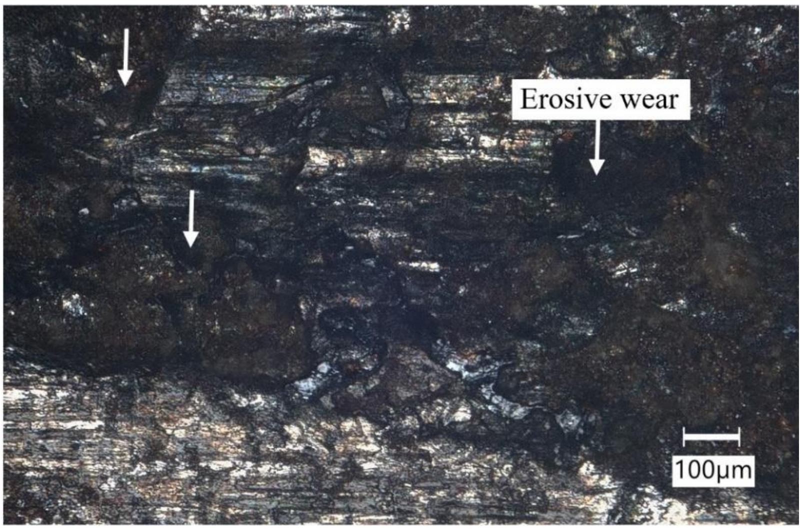

(c) Erosive wear in Area B in Region 5 of slip defect ②.

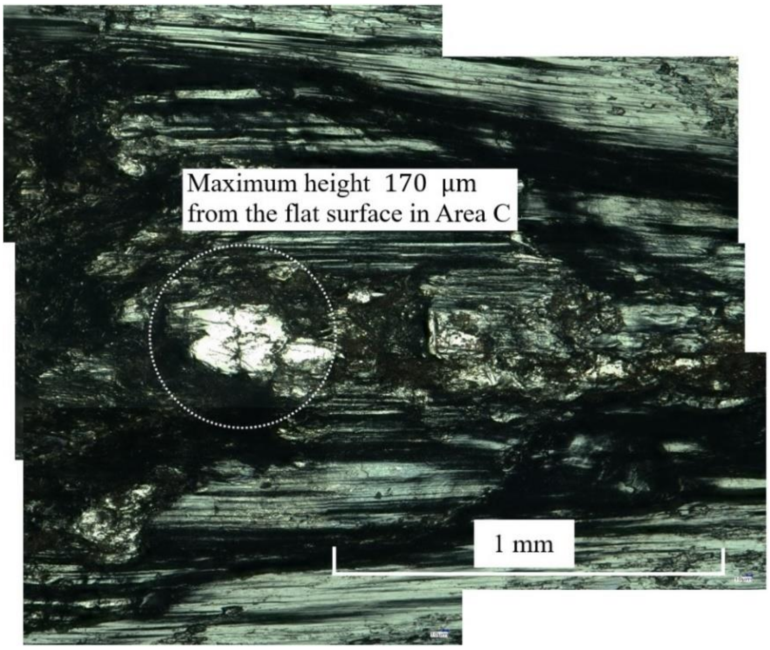

(d) Maximum height 170 μm in Area C in the right front of Region 5 of slip defect ②.

Fig. 4-8 Slip defect ② whose whole region can be classified into Region 1~Region 5 on the shaft surface.

uniformly dispersed as in Region 3 but are unevenly distributed under the influence of adhesive wear. In the semicircular region situated at the right front of

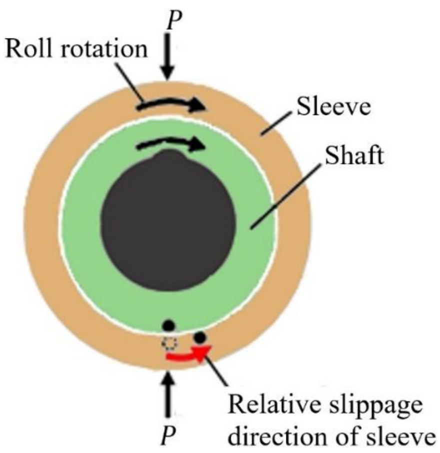

(a) 4-rolls rolling mill

(i) Contact

(ii) Generation of transfer element

(iii) Accumulation of transfer element

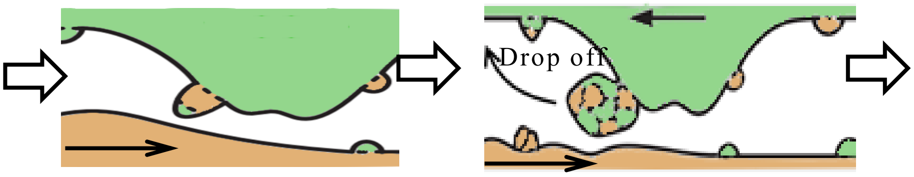

(iv) Formation of accumulated small lump

(v) Growth of transfer cohesive ball

(b) Detail of transfer particles formation process of Area C from Fig. 4-8(a).

Fig. 4-9 Sasada's model of transfer particles and growth during sliding to explain the change from Region 1 to Region 2.

Region 5 in Fig. 4-8(a), the maximum height of 170 μm can be seen as shown in Fig. 4-8(d). It should be noted, the maximum depth of the defect on the sleeve discovered is 170 μm, which later becomes 250 μm around the same area (see Fig. 4-7(e) and Fig. 4-12). The cohesive mass is generated on the sleeve side, which has lower hardness, sticks to the shaft side, and swells to reach the maximum height. It is conjectured that the cohesive mass is formed by applying a repeated compression load to the wear debris which was generated on the sleeve side after the slip stops.

In Sections 4.4.1 and 4.4.2, the slip defect ② was observed on the sleeve and the shaft were classified into Region 1 ~ Region 5. From there, the characteristics and changes of those regions were described, leading to the clarification of the defect formation and growth. Similarly, slip defect ④ can be classified into Region 1 ~ Region 5 and its growth process can be traced as discussed for Figs. 4-7 and 4-8.

4.4.3 Adhesive wear model for Region 1 and Region 2

The adhesion wear generation for Region 1 and Region 2 can be explained by using a model proposed by Sasada as shown in Fig. 4-9 [35]. Fig. 4-9 illustrates the growth and detachment process of the transferred particles when two opposite surfaces move relatively. In Fig. 4-10, the particles before falling off are illustrated as the wear particles at friction interface. The process can be summarized in the following way.

(1) The real contact portions, which are the protrusions on the surface, come into contact and deform to form junctions.

(2) The formed junctions are sheared and broke out from the inside of the material.

(3) The broken part adheres to the contact surface and generates a transfer element, which is an elementary particle that forms a wear particle.

(4) Adhesive particles which are generated on a mutual friction surface aggregate, merge at the friction interface, and grow to form transferred particles.

(5) Finally, wear occurs when the transferred particles are fallen off and released from the friction surface as wear particles.

According to this model, the transferred particles are crushed and spread by frictional force while supporting the load at the friction interface. In this way, the defect caused by interfacial slip begins with a scratch wear at the top of the finishing process. In regard to this, the starting point of the adhesive defect of the sleeve shown will be identified accurately to determine the defect length in the next Section 4.4.4.

4.4.4 Defect length in relation to the slip distance

In this section, the defect length on the sleeve and shaft surface are considered. The slip starts with the roll rotation, and the starting point corresponds to the scribe line on the miniature roll specimen in Fig. 4-2. Due to the relative slip between the sleeve and shaft, the sleeve slip of the length ℓ_{total}^{sleeve} occurs in the direction which is opposite to the rotation with respect to the shaft. Instead, the shaft slip of the length ℓ_{total}^{shaft} occurs in the same direction as the rotation direction. The sum $\ell_{total}^{sleeve}+\ell_{total}^{shaft}$ is compared with the slip amount $\ell_s = \pi d\theta_{slip}/360$ in Fig. 4-2 that is obtained from the scribe line in the miniature roll specimen. The relationship between the slip distance ℓ_s and the slip defect length in Fig. 4-6 is discussed by observing the slip defects ② and ④ in detail since the defect size ② and ④ are relatively largest.

Fig. 4-10 shows the slip defects ② and ④ on the sleeve and shaft were observed at 50× magnification. As shown in Figs. 4-10(a) and 4-10(b), the slip defect ② has ℓ_{total}^{sleeve} = 13.9 mm on the sleeve, ℓ_{total}^{shaft} = 19.3 mm on the shaft and the total length is 13.9 + 19.3 = 33.2 mm. As shown in Figs. 4-10(c) and 4-10(d), the slip defect ④ has ℓ_{total}^{sleeve} = 14.3 mm on the sleeve, ℓ_{total}^{shaft} = 18.4

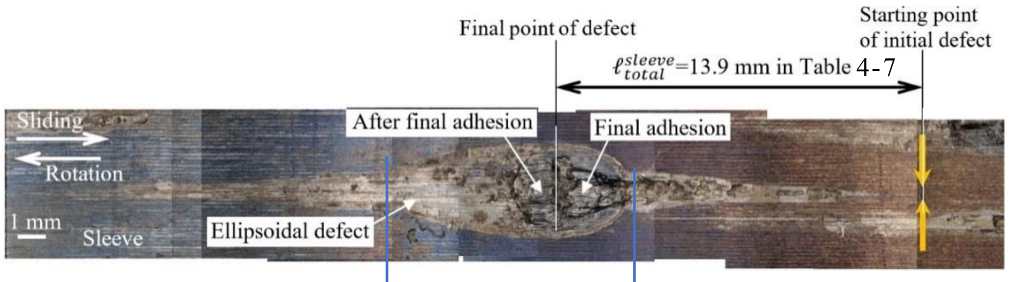

(a) Slip defect ② on the sleeve.

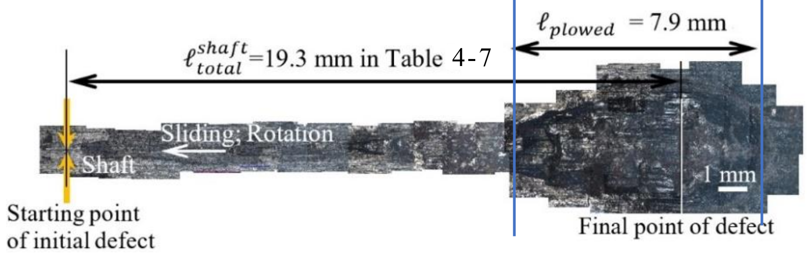

(b) Slip defect ② on the shaft.

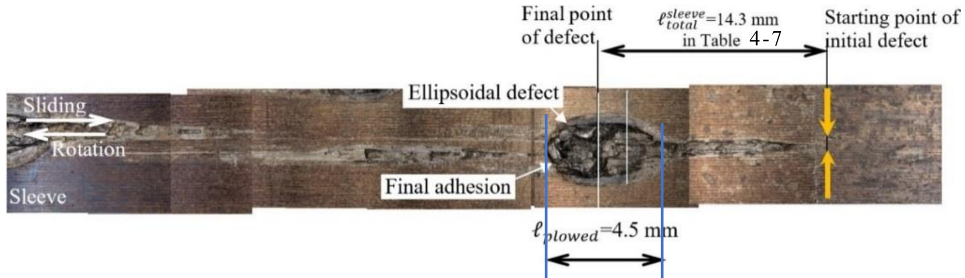

(c) Slip defect ④ on the sleeve.

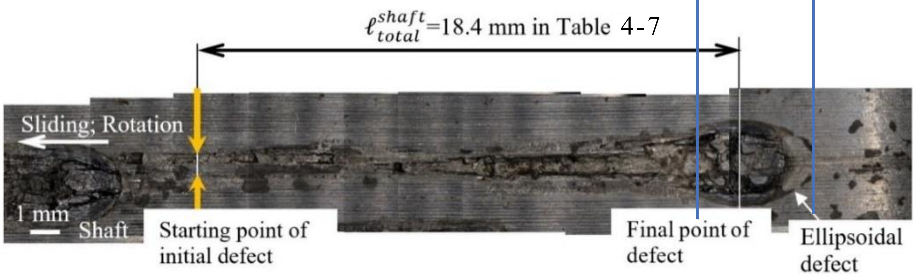

(d) Slip defect ④ on the shaft.

Fig. 4-10 Slip defects ② and ④ on the sleeve and shaft.

mm on the shaft and the total length is 14.3 + 18.4 = 32.7 mm. Table 4-7 summarizes those values. In Table 4-7, the total length for the defect ② and ④ are almost the same as the relative slip length of $\ell_s =$ 32.3 mm that is obtained from the slip specimen in Fig. 4-2. That being the case, it can be concluded that the starting point, as well as the ending point of the defects, can be evaluated

Table 4-7
Slip defect length observed on roll B in comparison with the slip length $\ell_s = \pi d\theta_{slip}/360 = 32.3$ mm in miniature roll specimen in Fig. 4-2.

	ℓ_{total}^{sleeve}: Slip defect length on the sleeve (mm)	ℓ_{total}^{shaft}: Slip defect length on the shaft (mm)	$\ell_{total}^{sleeve}+\ell_{total}^{shaft}$: Total length (mm)
Slip defect ②	13.9	19.3	33.2
Slip defect ④	14.3	18.4	32.7

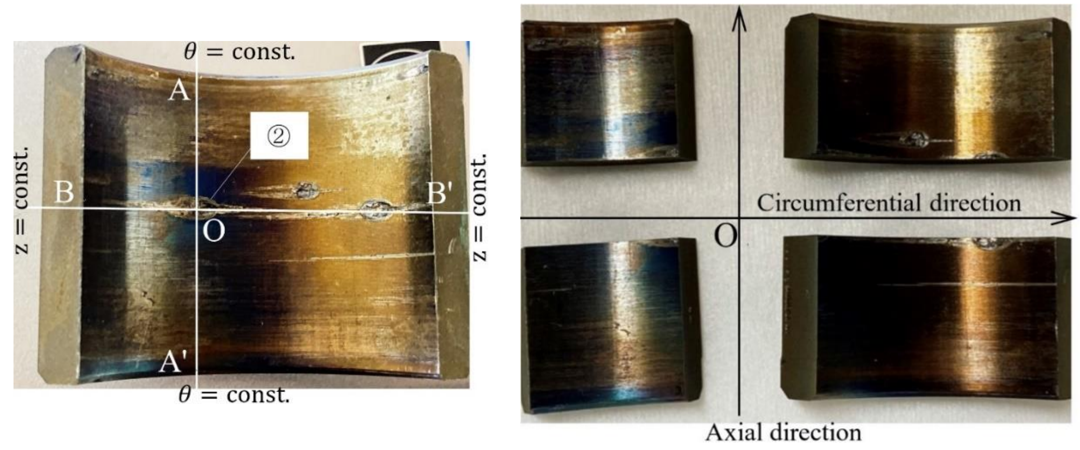

(a) Sleeve before cutting. (b) Sleeve after cutting.

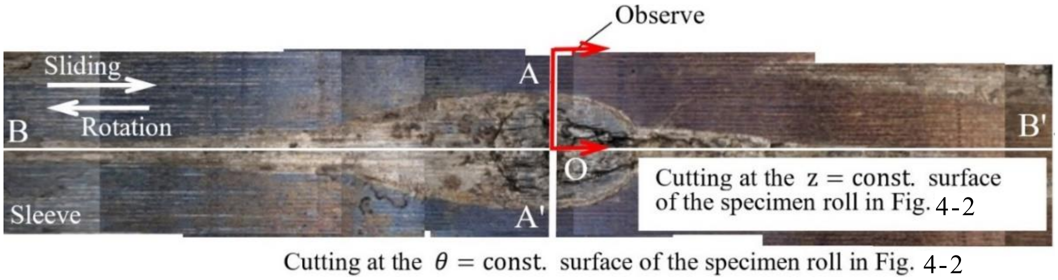

(c) Slip defect ② on the sleeve.

Fig. 4-11 Slip defect ② on the sleeve to identify defect dimension.

accurately reflecting the real slip.

4.5 Fatigue strength evaluation of the real roll considering the slip and the defect

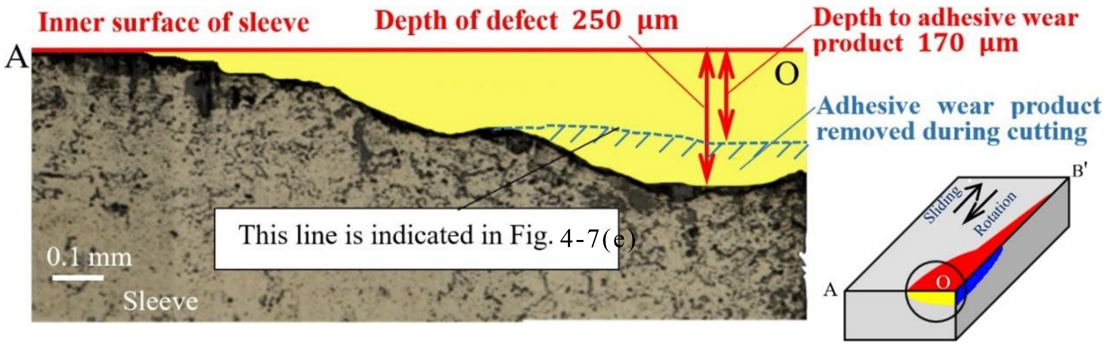

Fig. 4-12 Cross sectional observation of adhesive defect ② at the θ =const. surface of the sleeve in Fig. 4-11.

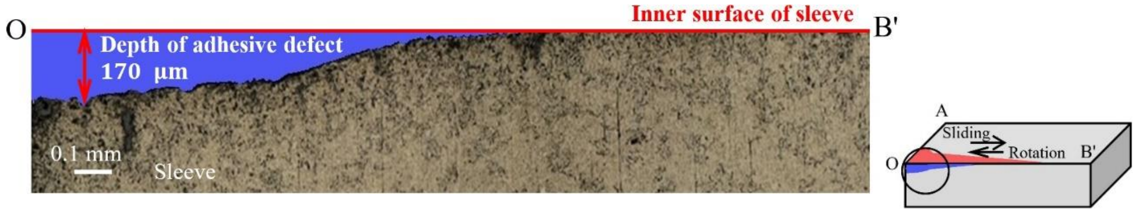

Fig. 4-13 Cross sectional observation of adhesive defect ② at the z = const. surface of the sleeve in Fig. 4-11.

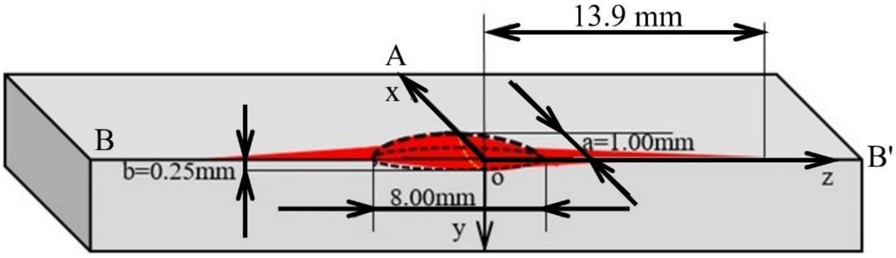

Fig. 4-14 Ellipsoidal plow defect ② geometry on the sleeve approximated by $(x/a)^2 + (y/b)^2 + (z/c)^2 = 1,\ a = 1,\ b = 0.25,\ c = 4.0,\ K_t \cong 1.14$.

4.5.1 Three-dimensional defect geometry in miniature roll specimen

In this section, the geometry of the slip defect ② is identified. Then, the stress concentration factor of the ellipsoidal part is estimated, and finally, fatigue strength of the real roll is investigated considering the slip as well as the slip defect. For roll B, the geometry of the slip defect ② on the sleeve surface is identified by cutting the sleeve. Fig. 4-11 illustrates (a) the sleeve before cutting,

(b) the sleeve after cutting, and (c) the enlarged view of the defect ② on the sleeve before cutting. A detailed identification of the defect depth geometry is carried out by observing the cross sections of AO and OB'.

Fig. 4-12 shows the AO cross section in Fig. 4-11. On the other hand, Fig. 4-13 shows the OB' cross section in Fig. 4-11. Fig. 4-12 and Fig. 4-13 portray the depth of 0.25 mm on AO cross section side and the depth of 0.17 mm on OB' cross section. Fig. 4-14 illustrates a three-dimensional shape of the defect. This elliptical part can be approximately assessed as $(x/a)^2 + (y/b)^2 + (z/c)^2 = 1$, $(a = 1,\ b = 0.25,\ c = 4.0)$. Henceforth, the stress concentration factor of K_t ≅1.14 can be estimated [36].

4.5.2 Stress amplitude and mean stress in real roll

In the previous paper as well as in Section 4-3, the interfacial slip was realized in the numerical simulation by applying the load shifting on the fixed roll surface to express the roll rotation [16-19]. In this section, the simulation can be applied to the real roll to evaluate the interfacial stress. Fig. 4- 15 shows the dimensions of the real roll where fatigue strength should be evaluated. A standard load of $P = P_0 = 13270$ N/mm was applied to the real rolls that was used in the hot rolling [10, 11]. In this section, fatigue strength is evaluated under a severe load of $P = 1.5P_0$, which considers the impact force during the plate biting as well as load variations due to the roll temperature change and setting error. Here, it is assumed that the shrink-fitting ratio is $\delta/d = 0.5 \times 10^{-3}$ and the friction coefficient between the sleeve and the shaft is $\mu = 0.3$ (see Sections 3.4.2 and 3.4.3) [16-19].

Fig. 4-16 shows an interface stress variation in the θ-direction due to two rotations of the load shifting on a fixed roll. It is confirmed that one rotation and

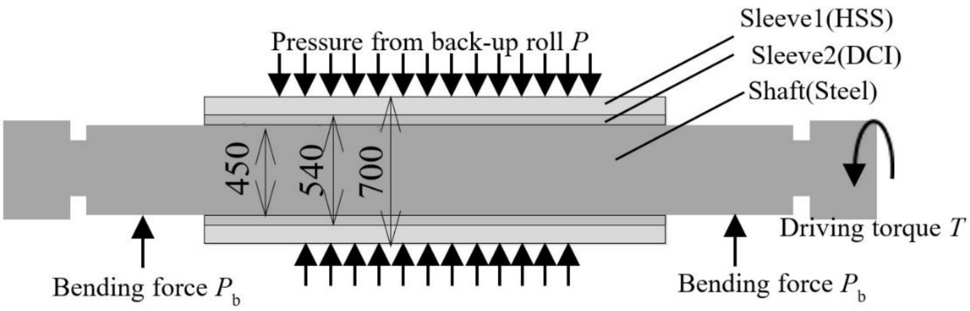

Fig. 4-15 Real sleeve roll geometry used in hot strip rolling to evaluate fatigue strength assuming the shrink-fitting ratio of $\delta/d = 0.5 \times 10^{-3}$ and the friction coefficient of $\mu = 0.3$ between the sleeve and the shaft.

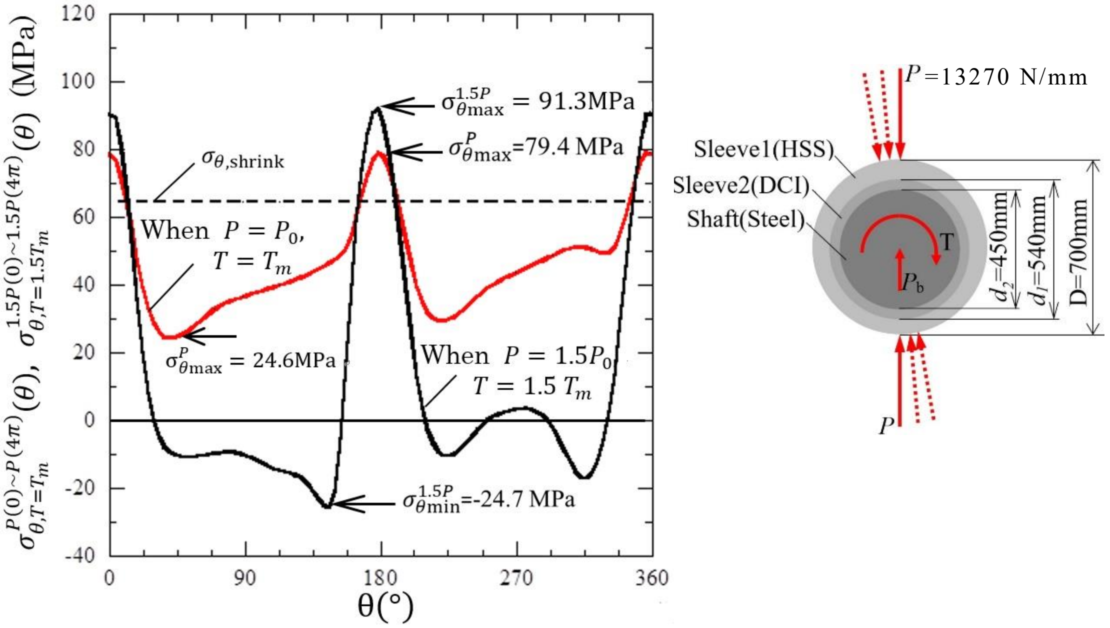

Fig. 4-16 Interface stress variation $\sigma_{\theta,T=T_m}^{P(0)\sim P(4\pi)}(\theta)$ due to the standard load of $P = P_0$ shifting in comparison with $\sigma_{\theta,T=1.5T_m}^{1.5P(0)\sim 1.5P(4\pi)}(\theta)$ due to the severe load of $P = 1.5P_0$ shifting in Fig. 4-15.

two rotations create almost the same stress variation in the θ-direction. Therefore, this section highlights the use of the stress obtained after two rotations to evaluate fatigue strength because of the high stability of the variation. In Fig. 4-16, the interface stress variation $\sigma_{\theta}^{P(0)\sim P(4\pi)}(\theta)$ due to the two rotations of the standard load of $P = P_0$ shifting is compared with the $\sigma_{\theta}^{1.5P(0)\sim 1.5P(4\pi)}(\theta)$ due to the two rotations of the severe load of $P = 1.5P_0$ shifting. The stress $\sigma_\theta^{P(0)\sim P(4\pi)}(\theta)$ due to $P = P_0$ has maximum stress of $\sigma_{\theta max} = 79.4$ MPa and the minimum stress of $\sigma_{\theta min} = 24.6$MPa. Instead, the stress $\sigma_\theta^{1.5P(0)\sim 1.5P(4\pi)}(\theta)$ due to $P = 1.5P_0$ has the maximum stress of $\sigma_{\theta max} = 91.3$ MPa and minimum stress of $\sigma_{\theta min} = -24.7$ MPa. Here, σ_a which denotes the stress amplitude and σ_m which denotes the average stress are expressed in Eq. (4-4) and Eq. (4-5).

$$\sigma_a = (\sigma_{\theta max} - \sigma_{\theta min})/2 \tag{4-4}$$

$$\sigma_m = (\sigma_{\theta max} + \sigma_{\theta min})/2 \tag{4-5}$$

Under the standard loading of $P = P_0$, the stress amplitude of $\sigma_a = 27.4$ MPa and the average stress of $\sigma_m = 51.9$ MPa are obtained. Instead, under the severe loading of $P = 1.5P_0$, the stress amplitude of $\sigma_a = 58.1$ MPa and the average stress of $\sigma_m = 33.3$ MPa are obtained. With an increasing the load of 1.5 times larger, the stress amplitude σ_a increases by about 2.1 times larger and the average stress σ_m increases by about 0.6 times larger.

4.5.3 Fatigue strength evaluation of the real sleeve roll on the stress amplitude versus mean stress diagram

In this section, the fatigue strength of the real sleeve roll is evaluated by considering the circumferential slip. A similar defect identified in Section 4.5.1 that occurs in the real roll due to the slip is assumed. If the defect geometry is similar to the one observed in the miniature roll, the fatigue strength of the sleeve can be examined by using a stress concentration factor of $K_t \cong 1.14$ which was obtained for the slip defect ② in Fig. 4-14. Fig. 4-17 shows the stress amplitude versus the mean stress diagram (σ_a - σ_m diagram) for the stress σ_θ which appears at the inside of the sleeve. In this diagram, a tensile strength of σ_B = 415 MPa for the inner layer material DCI is applied and a fatigue limit of σ_w = 166

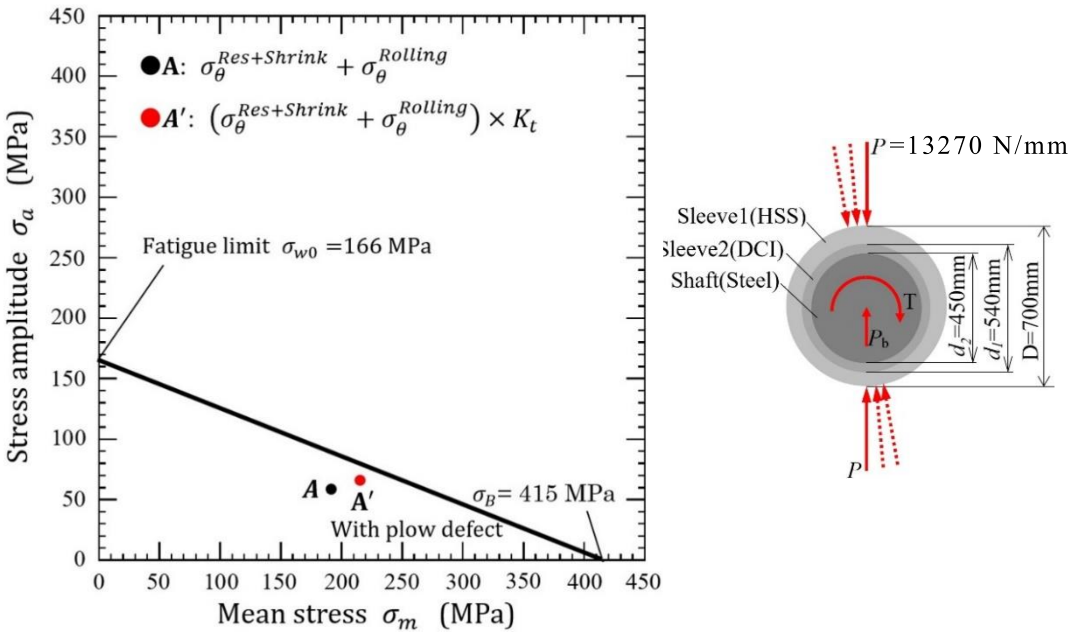

Fig. 4-17 Stress amplitude versus mean stress diagram ($\sigma_a - \sigma_m$ diagram) to evaluate the real sleeve roll fatigue strength based on the DCI tensile strength of $\sigma_B = 415$ MPa and DCI alternate fatigue strength of $\sigma_{w0} = 166$ MPa.

MPa with the durability ratio of 0.4 is used. Point A in Fig. 4-17 shows the results σ_a = 58.1 MPa and σ_m = 33.3 MPa under a load of $P = 1.5P_0$, while considering the impact force explained in Section 4.5.2 as well as superposing the residual stress of 156 MPa as the mean stress. To evaluate the fatigue risk on the safe side, the stress concentration factor of $K_t \cong 1.14$ is multiplies to the results of Point A, thus, Point A' is shown. As shown in Fig. 4-17, even by using a severe loading of $P = 1.5P_0$, Point A is still located inside the endurance limit line. In addition, by considering the stress concentration of the defect, Point A' is also located inside the endurance line.

4.6 Conclusion for Chapter 4

Shrink-fitted sleeve rolls have several advantages and one of them is the possibility of reusing shaft by replacing the sleeve after consumed due to the abrasion or the surface roughening. In the sleeve roll, however, an interfacial slip may occur between the shaft and the shrink-fitting sleeve which sometimes causes a sleeve fracture. In this paper, the interfacial slip was experimentally verified by using a miniature rolling mill through numerical simulation that have been discussed in previous studies. Consequently, the slip was confirmed, and the slip damage was identified. The conclusions can be summarized as follows:

1) Regarding the relative slip distance, the numerical simulation results are approximately 3.6~4.3 times larger than the experimental results for both shrink-fitting ratio of $\delta/d = 0$ and $\delta/d = 0.21 \times 10^{-3}$. The comparison of the experimental results with the numerical simulation confirms the usefulness of the previous numerical simulation by Noda et al. [18, 19].
2) The experiment and numerical simulation showed that under no shrink-fitting of $\delta/d = 0$, the slip distance becomes 2.79~3.53 times larger than the slip distance for $\delta/d = 0.21 \times 10^{-3}$.
3) The slip defect can be formed in the following way. Firstly, the slip defect starts with the contact of the surface roughness where the width is about to coincide with the pitch of the machining feed. Secondly, the slip defect is developed by the erosion and cohesive wear during the rolling. Finally, the slip defect forms a large oval-shaped erosion groove at the end of the scratch.
4) The defects observed on the sleeve and the shaft can be classified into Region 1 ~ Region 5. The characteristics along with the changes of the regions are described, and the defect formation as well as growth were clarified.
5) For the shrink-fitting ratio of $\delta/d = 0.21 \times 10^{-3}$ from the miniature roll experiment, the slip distance of $\pi d\theta_{slip} = 32.3$ mm which is obtained from the marked line coincides with the sum of defect that is observed on the sleeve and the shaft, for defect ②: 33.2 mm and for defect ④: 32.7 mm. This coincidence

showed that the start and the end points of the defects were clearly identified.

6) The three-dimensional defect geometry was identified. The total length of the slip defect is 13.9 mm, and the maximum depth is 0.25 mm. The stress concentration factor can be estimated as $K_t \cong 1.14$ by using the assumption of ellipsoidal shape approximation. The fatigue risk of the sleeve roll was estimated by using the dimensions and results obtained by numerical simulation while considering the slip.

References for Chapter 4

[1] H. Shimoda, S. Onodera, K. Hori, Study on the residual deflection of large sleeved back-up rolls: 4th Report, Residual stresses of sleeved rolls, Trans. Jpn. Soc. Mech. Eng. 32 (1966) 689-694.
[2] H. Takigawa, K. Hashimoto, G. Konno, S. Uchida, Development of forged high-speed-steel roll for shaped steel, CAMP-ISIJ 16 (2003) 1150-1153.
[3] T. Irie, K. Takaki, I. Tsutsunaga, Y. Sano, Steel strip and section steel and thick rolling processing, Tetsu-to-Hagane 65 (1979) 293.
[4] T. Hattori, Y. Kamitani, K. Sugino, H. Tomita, Y. Sano, Super cermet rolls for manufacturing ultra-fine-grained steel, International Conference on Tribology in Manufacturing Processes ICTMP 2007 International Conference 24-26 September 2007, Yokohama.
[5] N.A. Noda, Y. Sano, Y. Takase, Y. Shimoda, G. Zhang, Residual deflection mechanism for back-up roll consisting of shrink-fitted sleeve and arbor, J. Jpn. Soc. Technol. Plast. 58 (2017) 66.
[6] N.A. Noda, H. Sakai, Y. Sano, Y. Takase, Y. Shimoda, Quasi-equilibrium stress zone with residual displacement causing permanent slippage in shrink-fitted sleeve rolls, Metals 8 (12) (2018) 998, https://doi.org/10.3390/met8120998.
[7] E. Matsunaga, Y. Sano, S. Nishida, Measurement of residual stress in high speed steel roll (Residual stress measuring of rolling roll by X-ray method-2), CAMP-ISIJ 10 (1997) 1078.
[8] E. Matsunaga, T. Tsuyuki, Y. Sano, Optimum shrink fitting ratio of sleeve roll (Strength design of shrink fitted sleeve roll for hot strip mill-1), CAMP-ISIJ 11 (1998) 362. https://ci.nii.ac.jp/naid/10002551803.
[9] S. Tutumi, S. Hara, S. Yoshi, The residual deflection of sleeved back-up rolls, Tetsu-to-Hagane 57 (5) (1971) 818-822.
[10]Y. Sano, Recent advances in rolling rolls, Proc of the No. 148-149 Nishiyama Memorial Technology Course, Tokyo, Japan (1993) 193-226.
[11]Y. Sano, Fatigue failure problem in the inside of roll body for hot strip rolling- Crack initiation problem and its estimation in the actual plant, The 245th JSMS Committee on Fatigue of Materials and The 36th JSMS Committee on Strength Design, Safety Evaluation (1999) 40.
[12]E. Matsunaga, T. Tsuyuki, Y. Sano, Optimum shrink fitting ratio of sleeve roll (Strength design of shrink fitted sleeve roll for hot strip mill-1), CAMP-ISIJ 11 (1998) 362, https://ci.nii.ac.jp/naid/10002551803.
[13]S. Spuzic, K.N. Strafford, C. Subramanian, G. Savage, Wear of hot rolling mill rolls: an overview, Wear 176 (2) (1994) 261-271,

https://doi.org/10.1016/0043-1648(94)90155-4.
[14]N.A. Noda, K. Hu, Y. Sano, K. Ono, Y. Hosokawa, Residual stress simulation for hot strip bimetallic roll during quenching, Steel Res. Int. 87 (11) (2016) 1478-1488, https://doi.org/10.1002/srin.201500430.
[15]K. Hu, Y. Xia, F. Zhu, N.A. Noda, Evaluation of thermal breakage in bimetallic work roll considering heat treated residual stress combined with thermal stress during hot rolling. Steel Res. Int. 89(4) (2017) 1700368. https://doi.org/10.1002/srin.201700368.
[16]H. Sakai, N.A. Noda, Y. Sano, G. Zhang, Y. Takase, Numerical simulation on interfacial creep generation for shrink-fitted bimetallic roll, ISIJ Int. 59 (5) (2019) 889-894, https://doi.org/10.2355/isijinternational.ISIJINT-2018-749.
[17]H. Sakai, N.A. Noda, Y. Sano, G. Zhang, Y. Takase, Effect of driving torque on the interfacial creep for shrink-fitted bimetallic work roll, Tetsu-to-Hagane 105 (12) (2019) 1126-1134. https://doi.org/10.2355/tetsutohagane.TETSU-2019-048.
[18]N.A. Noda, R.A. Rafar, H. Sakai, X. Zheng, H. Tsurumaru, Y. Sano, Y. Takase Irreversible Interfacial Slip in Shrink-Fitted Bimetallic Work Roll Promoted by Roll Deformation. Eng. Fail. Anal. 126 (2021) 105465, https://doi.org/10.1016/j.engfailanal.2021.105465.
[19]R.A. Rafar, N.A. Noda, H. Tsurumaru, Y. Sano, Y. Takase, Novel design concept for shrink-fitted bimetallic sleeve roll in hot rolling mill, Int. J. Adv. Manuf. Technol. (2022) 1-14, 10.1007/s00170-022-08954-2
[20]N.A. Noda, R.A. Rafar, Y. Sano, Stress due to interfacial slip causing sleeve fracture in shrink-fitted work roll, Int. J. Mod. Phys. B (2021) pp 2140020. https://doi.org/10.1142/S0217979221400208.
[21]N. Soda, Bearing. Iwanami Shoten, Tokyo (1964) 196-203.
[22]M. Imai, Creep of the roller bearing, Lubrication: J. Jpn. Soc. Lubr. Eng. 4 (6) (1959) 307-312.
[23]J. Murata, T. Onizuka, Generation mechanism of inner ring creep, Koyo Eng. J. 166 (2005) 41-47.
[24]T. Niwa, A creep mechanism of rolling bearings, NTN Tech. Rev. 81 (2013) 100-103.
[25]Ten, Sakajiri, Takemura, Yukawa, NSK Tech. J. 680 (2006) 13.
[26]New Bearing Doctor: Diagnosis of bearing problems. Objective: Smooth & reliable operation. NSK, https://www.nsk.com/common/data/ctrgPdf/e7005c.pdf. (1997) [accessed 28 June 2020], https://www.nsk.com/common/data/ctrgPdf/e7005c.pdf.
[27]J. Zhan, H. Takemura, K. Yukawa, A study on bearing creep mechanism with FEM simulation, Proceedings of IMECE2007, 2007 Seattle, Washington, USA. https://doi.org/10.1115/IMECE2007-41366.
[28]J. Zhan, K. Yukawa, H. Takemura, Analysis of bearing outer ring creep with FEM, Advanced Tribology, 2009, Springer, Berlin, Heidelberg. https://doi.org/10.1007/978-3-642-03653-8_74.
[29]S. Noguchi, K. Ichikawa, A study about creep between inner ring of ball bearing and shaft, Proceeding of Academic Lectures of the Japan Society for Precision Engineering, 2010, Japan. https://doi.org/10.11522/pscjspe.2010A.0.565.0.
[30]T. Teramoto, Y. Sato, Prediction method of outer ring creep phenomenon of ball bearing under bearing load, Trans. Of Society of Automotive Eng. of Japan, 46 (2015) 355-360. https://doi.org/10.11351/jsaeronbun.46.355.
[31]C. Bovet, L. Zamponi, An approach for predicting the internal behaviour of ball bearings under high moment load, Mech. Mach. Theory 101 (2016) 1-22, https://doi.org/10.1016/j.mechmachtheory.2016.03.002.
[32]A. Maiwald, E. Leidich, FE simulations of irreversible relative movements

(creeping) in rolling bearing seats –Influential parameters and remedies, World Congress on Engineering and Computer Science 2013 Vol II, San Francisco, USA, http://www.iaeng.org/publication/WCECS2013/WCECS2013_pp1030-1035.pdf.

[33]T. Schiemann, S. Porsch, E. Leidich, B. Sauer, Intermediate layer as measure against rolling bearing creep, Wind Energy 21 (2018) 426-440, https://doi.org/10.1002/we.2170.

[34]Y. Sano, Ph.D. thesis, Kyushu University (1995).

[35]A. Hase, Research cases and trends of wear mechanism, J. Surf. Finish. Soc. Jpn. 65 (2014) 556-561, https://doi.org/10.4139/sfj.65.556.

[36]Y. Murakami, The idea of stress concentration, Yokendo Publishing Co. Ltd. Tokyo (2005) 47.

[37]T. Sawamoto, Precision machinery, 30 (1964) 8.

[38]Misumi-vona Top, Technical information, Dry coefficient of friction. https://jp.misumi-ec.com/tech-info/categories/plastic_mold_design/pl07/c0874.html.

[39]JSME mechanical engineers' handbook α2, The Japan society of mechanical engineers, Tokyo, (2004) 27.

[40]Marc Mentat team: Theory and User Information, Vol. A, MSC, Software, Tokyo (2008) p.713.

5 The inner surface stress and fatigue fracture analysis of shrink-fitted bimetallic sleeve roll

5.1 Bimetallic work roll

5.1.1 Introduction

Rolling rolls are essential to the iron and steel industries, and therefore lots of efforts have been done to improve their mechanical properties. Fig. 5-1 illustrates the rolling roll in roughing stands of hot rolling stand mills. The rolls are classified into two types; one is a single-solid type, and the other is a shrink-fitted assembled type consisting of a sleeve and a shaft. In shrink-fitted sleeve roll, although the wear and surface roughness soon appear on the roll body, the shaft can be reused. However, it is clarified in the previous study that this shrink-fitted structure has generated the interfacial slip between the sleeve and the shaft [18, 49, 50]. Furthermore, in order to consider the roll breakage caused by the stress due to the interfacial slip, the stress state in the shrink-fitted surface will be focused in this paper.

5.1.2 Numerical simulation method on interface slip under the action of shaft drive torque

Fig. 5-1 illustrates two-dimensional modeling in numerical simulation. Fig. 5-1(a) illustrates the central cross-section of real roll and Fig. 5-1(b) illustrates the real roll by shifting the load on the roll surface with the roll center fixed. Here, the motor torque T is balanced with the frictional moment S as $T = SD/2$ where D is the sleeve outer diameter. Fig. 5-1(c) shows the analysis roll model that is used in the study. In Fig. 5-1, the roll is subjected to compressive force P from the back-up roll, the rolling reaction force P_h, the frictional force S from the strip, the bending force P_b from the bearing and torque T from the motor.

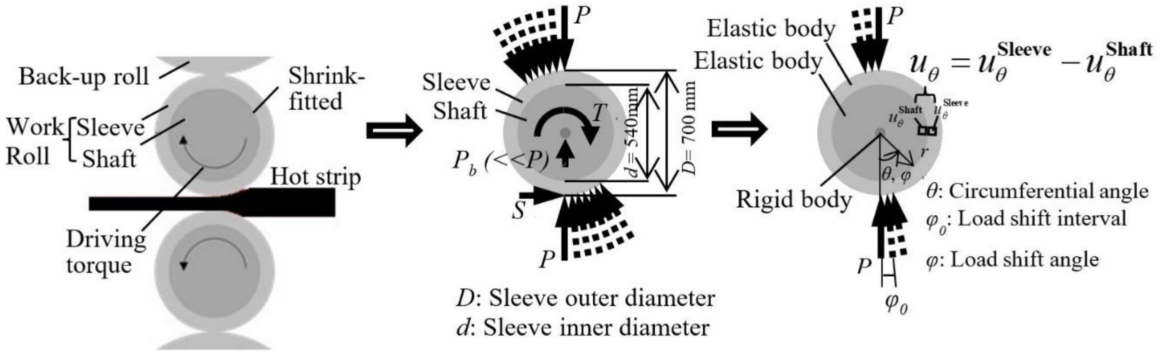

(a) Central cross-section view of real roll. (b) Real roll. (c) Analysis roll model.

Fig. 5-1 Modeling and simulation for interfacial slip when *P* is the load from back-up roll and hot-strip, *S* is the frictional force, P_b is the bending force from bearing, *T* is the driving torque.

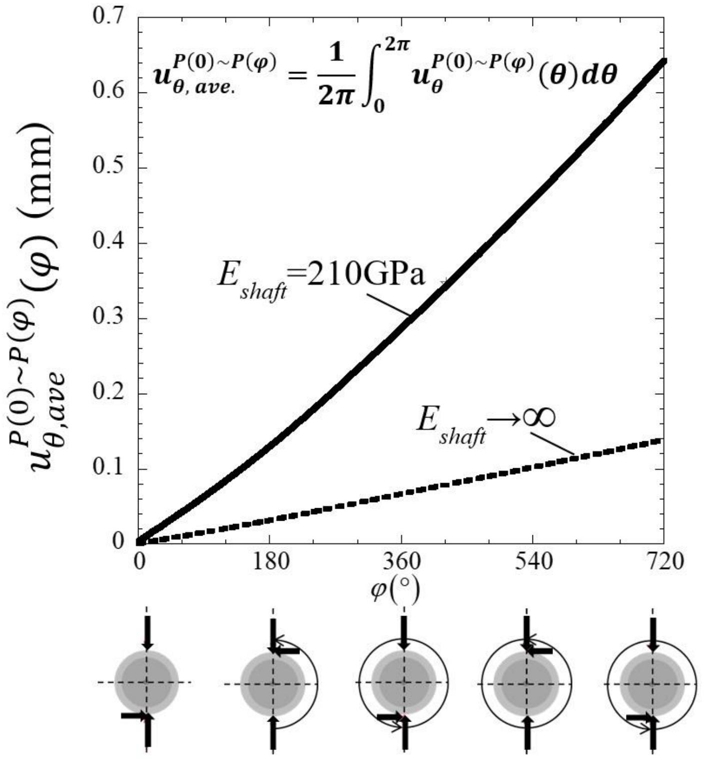

Fig. 5-2 Interfacial displacement for shaft Young's modulus E_{shaft}= 210 GPa in comparison with $E_{shaft} \rightarrow \infty$.

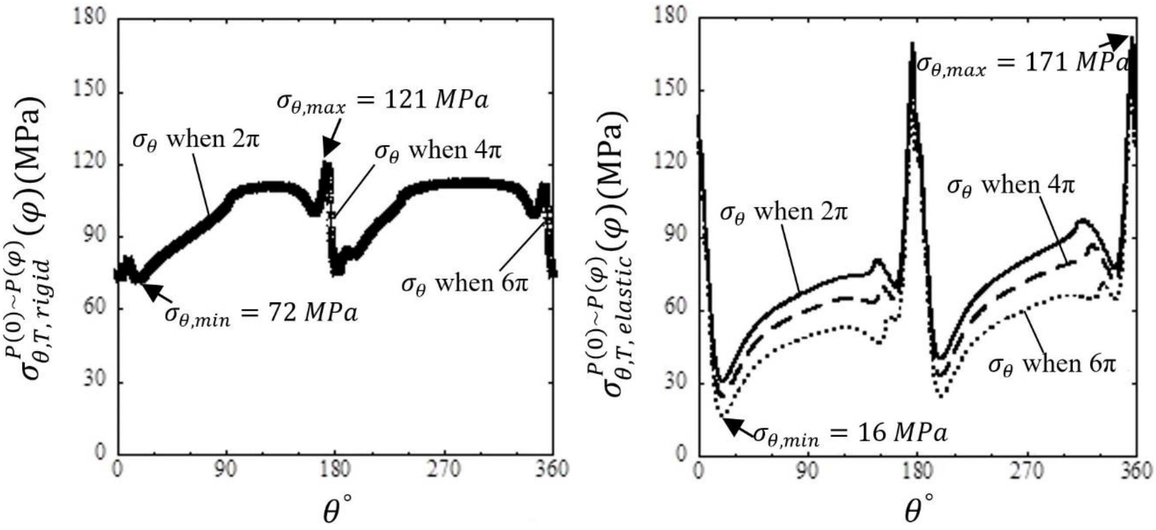

(a) $\sigma_{\theta,T}^{P(0)\sim P(2\pi)}$, $\sigma_{\theta,T}^{P(0)\sim P(4\pi)}$ and $\sigma_{\theta,T}^{P(0)\sim P(6\pi)}$ for $E_{shaft} \to \infty$.

(b) $\sigma_{\theta,T}^{P(0)\sim P(2\pi)}$, $\sigma_{\theta,T}^{P(0)\sim P(4\pi)}$ and $\sigma_{\theta,T}^{P(0)\sim P(6\pi)}$ for E_{shaft}= 210 GPa.

Fig. 5-3 $\sigma_{\theta,T}^{P(0)\sim P(2\pi)}$, $\sigma_{\theta,T}^{P(0)\sim P(4\pi)}$ and $\sigma_{\theta,T}^{P(0)\sim P(6\pi)}$ when number of rotations n = 1, 2 and 3 of $E_{shaft} \to \infty$ and E_{shaft}=210 GPa.

Since two-dimensional model is applied, the external force per unit length should be considered. The loading condition used in this study is the concentrated loading P from the back-up roll and the reaction P from the strip with P=13270 N/mm. Here, when the rated torque of the motor is T_m = 471Nm/mm, the frictional force can be calculated as S=1346Nm/mm. The shrink-fitting ratio is defined as δ/d, where δ is the diameter difference between the inner diameter of the sleeve and d is the sleeve inner diameter. In this study, $\delta/d = 0.5\times10^{-3}$ is used with the friction coefficient $\mu = 0.3$ between the sleeve and the shaft.

In this analysis, the circumferential relative displacement at the interface between the sleeve and shaft when load move from the angle $\varphi = 0^{o}$ to $\varphi = \varphi$ is defined as $u_{\theta}^{P(0)\sim P(\varphi)}$. Here, notation φ denotes the load shifting angle and θ denotes the position where the displacement is evaluated. Thus, the accumulation of the displacement is given by the Eq. (5-1).

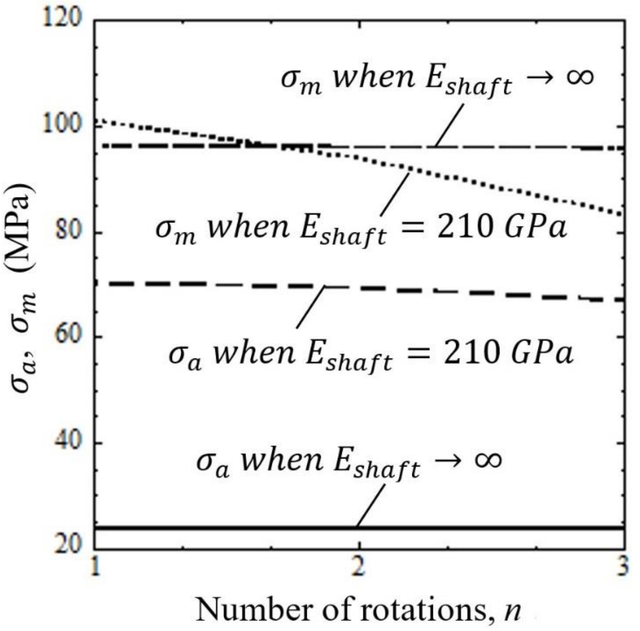

Fig. 5-4 Stress amplitude σ_a and mean stress σ_m for E_{shaft}=210 GPa in comparison with $E_{shaft} \to \infty$.

$$u_{\theta,ave.}^{P(0)\sim P(\varphi)} = \frac{1}{2\pi}\int_0^{2\pi} u_\theta^{P(0)\sim P(\varphi)}(\theta)d\theta \tag{5-1}$$

Fig. 5-2 shows the interfacial displacement $u_{\theta,ave.}^{P(0)\sim P(\varphi)}$ by rotating the load twice for shaft Young's modulus $E_{shaft} \to \infty$ and E_{shaft}= 210GPa. From the figure, the amount of interfacial slip $u_{\theta,ave.}^{P(0)\sim P(\varphi)}$ increases almost linearly with increasing the load shift angle φ. The interface slip may occur as soon as the load shifting starts.

5.1.3 Stress on the inner surface of the sleeve

In the sleeve assembly type roll, it should be noted that the circumferential slippage sometimes occurs even though the resistance torque at the interface is larger than the motor torque. Due to this slip, a localized adhesion occurs and causes a crack initiation. Then, the crack propagates and form a groove-like flaw. The repeated stress concentration at this flaw increases the flaw dimension and finally cause sleeve fracture [6]. In this way, the stress σ_θ appearing at the shrink-fitted surface should be estimated since σ_θ is the largest stress component and causes such damage.

Fig. 5-3 shows the stress distribution $\sigma_{\theta,T}^{P(0)\sim P(2\pi)}$, $\sigma_{\theta,T}^{P(0)\sim P(4\pi)}$ and $\sigma_{\theta,T}^{P(0)\sim P(6\pi)}$ when the number of rotations n= 1, 2 and 3, respectively, for (a) $E_{shaft} \to \infty$ and (b) E_{shaft}= 210GPa. In Fig. 5-3(a), there is almost no difference in the stress distribution σ_θ when n= 1, 2 and 3. From Fig. 5-3(a), the maximum stress is $\sigma_{\theta,max}$= 121MPa and the minimum stress is $\sigma_{\theta,min}$= 72MPa. In Fig. 5-3(b), the interfacial stress obtained shows differences in the stress distribution when n= 1, 2 and 3. From Fig. 5-3(b), the maximum stress is $\sigma_{\theta,max}$= 171MPa and the minimum stress is $\sigma_{\theta,min}$= 16MPa. Regarding the possibility of fatigue fracture from the inner surface of the sleeve due to these stresses, it is known that the inevitable tensile residual stress has a large effect on the inner surface of the sleeve.

The stress amplitude at which failure occurs for a given number of rotations is simplified in Fig. 5-4. In Fig. 5-4, stress amplitude σ_a and mean stress σ_m for $E_{shaft} \to \infty$ shows almost constant values as n increases. As for E_{shaft}= 210GPa, the fatigue strength shows the safety variation because stress amplitude σ_a and mean stress σ_m decreasing as the number of rotations increases.

5.1.4 Conclusion

In this paper, the stress due to the interfacial slip is studied because the stress may cause the sleeve fracture. In this study, the circumferential stress σ_θ should be estimated since σ_θ is the largest stress component and may cause sleeve damage. From the analysis, it was found that the stress in the shrink-fitted surface for $E_{shaft} \to \infty$ shows almost constant values as the number of rotations n increases. As for E_{shaft}= 210GPa, the stress in the shrink-fitted surface is slightly decreased with increasing n. Therefore, the stress obtained by simulation at n= 2 can be used to estimate the fatigue strength.

5.2 Bimetallic sleeve roll

5.2.1 Introduction

The rolling process is the most common metalworking process in the steel industries [1-22]. In steel industries, sleeve assembly types of rolling roll whose shaft is shrink-fitted into a hollow cylinder have been tried to be used. There have been successful applications of those sleeve rolls as work rolls for large steel H-sections and also as back-up rolls having large body diameters of more than 1000 mm. Fig. 5-5 shows an example of the sleeve roll used as a real hot strip rolling roll. Many technical terms including composite, compound and bimetallic are often used to describe the ductile casting iron (DCI) and high-speed steel (HSS) rolls. Similar to our previous papers, the term "bimetallic" is used in this article [18-19]. With improved heat crack as well as wear resistance, bimetallic work rolls are developed as an alternative to the conventional single-material rolls [12–14]. These sleeve rolls have some advantages such as after consumption, by replacing only a worn-out and abraded sleeve, the shaft can be reused. Moreover, the wear resistance of the sleeve can be improved separately while maintaining the shaft ductility. It should be noted that next generation rolls such as the super-cermet roll [15] and all ceramic roll [16] can be manufactured only as a sleeve roll. This is the reason why we have to develop sleeve roll technologies.

Several particular problems must be resolved to develop this shrink-fitted sleeve roll. They are referred to as residual roll deflection, fretting fatigue cracks

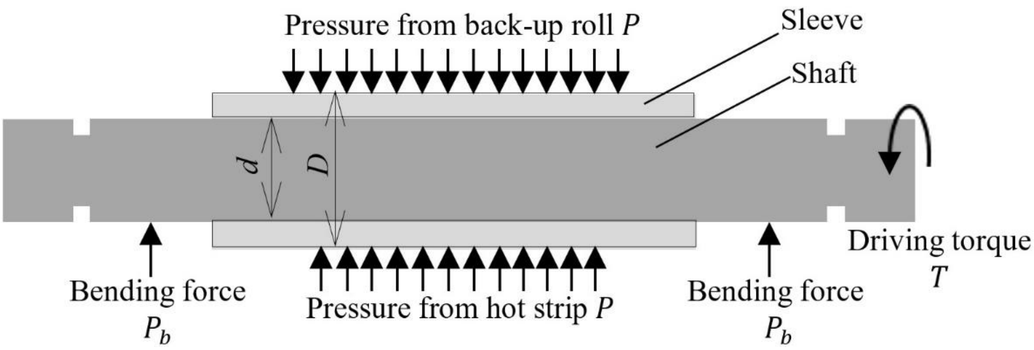

(a) Single material sleeve roll.

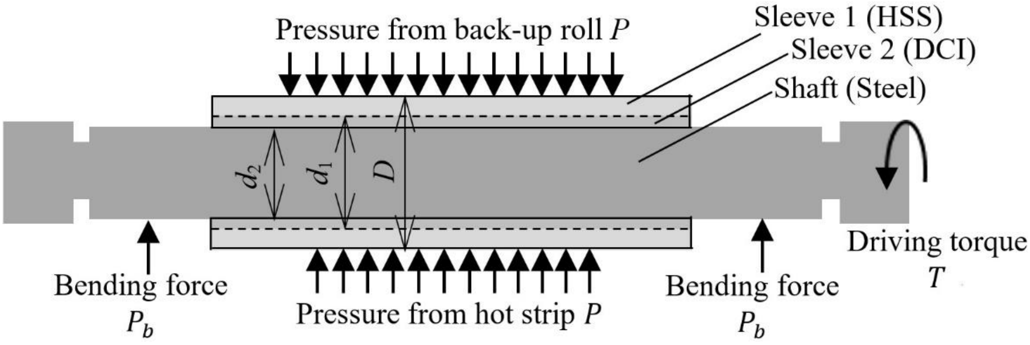

(b) Bimetallic sleeve roll.

Fig. 5-5 Schematic illustration for real hot strip rolling roll.

that grow at the endmost of the sleeve, and sleeve breakage that results from circumferential sleeve slippage [5–11]. From those problems, zero detailed studies have been carried out on circumferential slippage in the rolling roll. The same slippage that occurs in ball bearing as well is known as "interfacial creep" has been reported although no quantitative analysis can be found [23-35]. Considering those situations, in the authors' previous studies, numerical simulation was carried out to clarify the slippage by assuming a single material sleeve roll in Fig. 5-5(a) [17-21]. It is noteworthy that although the resistance torque near the interface is set to be greater than the motor torque, the circumferential slippage still occurs oftentimes. This is because non-uniform slip is caused by the loading although the conventional design only considers overall slip. The non-uniform slip often causes the fatal sleeve fracture in the following way [5, 6]. First, several scratches and partial seizures happen at the sleeve shrink-fitting surface. Second, the seizure growth causes surface roughness with a few millimeter depths. Third, due to the roughness, fatigue crack initiates and propagates at the sleeve inner surface causing the final fracture. In this way, the fatigue strength evaluation is necessary for sleeve rolls as well as clarifying the mechanism of interface slip.

Hence, this paper highlights the fatigue risk evaluation for the HSS bimetallic sleeve roll which is an extension of the numerical simulation for interfacial slip. Then, the stress variation due to the interfacial slip will be focused on instead of the relative slip displacement in the previous paper. The damage which is created by the slip will be considered as a defect reported in the previous studies. The fatigue limit will be evaluated by applying the $\sqrt{\text{area}}$ parameter model to create a fatigue limit diagram and to evaluate the safety zone for the sleeve roll defects.

5.2.2 Interfacial slip simulation on the interface stress σ_θ

In the previous studies [17-21], numerical simulations were performed to clarify the slippage by using a simplified rigid/elastic shaft in a single material sleeve roll as shown in Fig. 5-5(a). Then, the amount of the slip was investigated by varying several design factors such as shaft deformation, shrink-fitting ratio and motor torque condition. The outline for the load shifting method [17-21] is indicated in Appendix A.1, replacing the real roll rotation by the load shifting on the fixed roll.

Fig. 5-5 illustrates a sleeve roll considered for the fatigue risk evaluation when it is used in the 4-stage rolling mill. In the sleeve roll shown in Fig. 5-5(a), a steel shaft is shrink-fitted to a steel sleeve. Since it is necessary to have different properties of the sleeve, the bimetallic sleeve is used as the outer and inner layers. Fig. 5-5(b) shows an example of the bimetallic sleeve roll commonly used in metalworking which is built by the centrifugal casting process. In Fig. 5-5(b), a steel shaft is shrink-fitted to a sleeve roll that consists of a bimetallic sleeve. Here, there is a two-layer sleeve, which is an inner layer that is made of high ductility material known as ductile casting iron (DCI), and an outer layer that is made of high wear resistance and toughness material known as high-speed steel (HSS).

As shown in Fig. 5-5, the frictional force S from the hot strip, the rolling force P_h, as well as compressive force P from the back-up roll are applied on the roll. The two-dimensional modelling is used to simulate the interfacial slippage in rolling roll; and thus the external force per unit length and the motor torque T must be taken into consideration. From Fig. 5-5, it is known that length difference between the width of the hot strip and the back-up roll leads to the acting bending force P_b near the bearing. In the rolling process, these three forces which are the bending force P_b, the rolling reaction force P_h, as well as the rolling force P must be approximately the same. However, the bending force $P_b = 0$ is assumed in this study since P_b is evaluated to be <10% of P and P_h [5]. Therefore, equivalent forces of the rolling force from the back-up roll ($= {\sim}P \times$ length of back-up roll) and the rolling reaction force from the strip ($= {\sim}P_h \times$ width of the hot strip) can be achieved as $\mathrm{P} \simeq P_h$. The condition $\mathrm{P} \simeq P_h$ as considered in this study is referred to the loading conditions at the fifth stage of hot strip mill finishing train [5].

Fig. 5-6 shows the implementation of the two-dimensional modelling that is used in the numerical simulation. In Fig. 5-6(a), the real roll rotation is defined

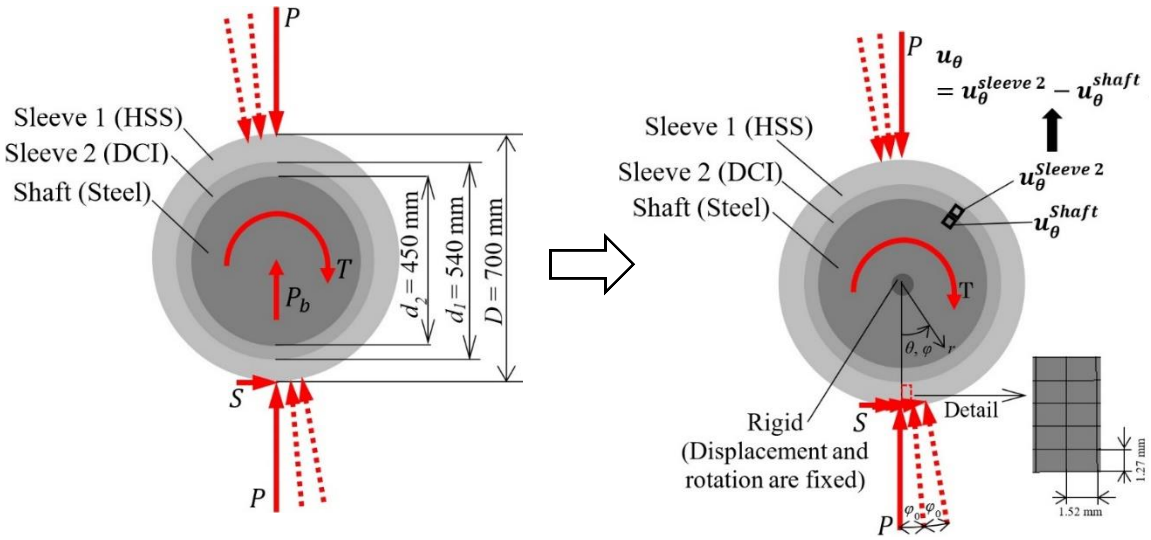

P: Load form back-up roll and hot strip (N)

S: Frictional force (N)

P_b: Bending force from bearing (N)

T: Driving torque (N m), T = SD/2

T_m: Rated torque of motor (N m)

T_r: Slippage resistance torque (N m)

θ: Circumferential angle of sleeve

φ_0: Load shift interval

φ: Load shift angle

(a) Real roll. (b) Analysis roll model.

Fig. 5-6 Modeling for bimetallic sleeve roll.

by the load shifting method where the load is shifted on the fixed roll surface [17–22]. In this study, the concentrated rolling load P is applied on the roll. During the rolling process, friction S and the driving torque T from the motor to the shaft are used to compress the hot strip between the rolls. Fig. 5-6(b) is a model in which the sleeve is a two-layer sleeve made of high-speed material and ductile material, and steel shaft is used in this study. In the simulation, it is necessary to introduce a rigid body at the center of the shaft in order to prevent the roll's center from rotating and to restrain the displacement. It is confirmed that the rigid body size at the center does not affect the result, and a diameter of 8 mm is used. The divided mesh for the finite element method (FEM) analysis is also shown in Fig. 5-6(b).

In Fig. 5-6, a numerical analysis of the sleeve assembly type roll is conducted using the finite element method (hereafter referred to as FEM). FEM simulation must be well performed to realize the interface slippage according to experience and skills offered for engineering applications. A mesh-independent technique was presented in the previous studies for bonded problems which demonstrated the insensitivity of the displacement boundary condition to the FEM mesh error [36-39]. The contact status changes when tightened the pitch-difference nut was clarified [40] and by using consecutive quasi-static analyses, dynamic deformation was investigated [41]. Based on these skills, the axial movement of the shaft during rotation of a ceramic roll was studied by transferring the load on the fixed shaft [42-45]. This paper emphasizes that by using the above technique for the elastic contact quasi-static study of rolling rolls, the circumferential sleeve slippage is analyzed with the use of FEM code Marc/Mentat 2012. Direct constraint method and complete Newton-Raphson method are applied for the contact study. Figure 2B illustrates a 4-node quadrilateral plane strain, with a mesh of 3. × 10^5 elements, which indicates that the mesh does not affect the results [46].

Table 5-1 portrays the boundary conditions, roll model dimensions, as well as mechanical properties which are used in the analysis. This section highlights the standard compressive force P is $P = P_0$ and the standard drive torque is $T = T_m$. In this study, the loading condition corresponds to the data obtained from the No. 5 stand of a hot strip finishing rolling mill [4, 5]. The conditions are assumed to be equivalent to hot rolling of ordinary steel sheets when a standard load $P = P_0 = 13270$ N/mm per 1 mm of the roll is applied. By applying the concentrated force P on the roll surface to replace the Hertzian contact stress, a small effect regarding the interfacial slippage can be confirmed.

Table 5-1

Dimensions, mechanical properties and boundary conditions of roll model

Mechanical properties	Sleeve	Shell E_{sleeve}	233 GPa
		v_{sleeve}	0.3
		Core E_{sleeve}	173 GPa
		v_{sleeve}	0.3
	Shaft	E_{shaft}	210 GPa
		v_{shaft}	0.28
Roll size		Outer diameter of sleeve	700 mm
		Inner diameter sleeve d_1	540 mm
		Inner diameter sleeve d_2	450 mm
Shrink fitting		Shrink fitting ratio δ/d	0.5×10^{-3}
		Friction coefficient between sleeve and shaft μ	0.3
External force		Concentrated load per unit width $P = P_0$	13270 N/mm Total: 1.327×10^{7} N Rolled width: 1000mm
		Frictional force per unit width S^*	1346 N/mm
		Motor torque per unit width $T_m{}^*$	471 N/mm
		Resistance torque per unit width $T_r{}^*$	3193 N m/mm
		Bending force from bearing P_b	0 N/mm

Instead of the standard force $P = P_0$ with the standard drive torque $T = T_m$, this study focuses on the rolling load $P = 1.5P_0$ with the drive torque $T = 1.5T_m$, which is corresponding to the impact load when the rolled plate biting trouble occurs.

Here, δ/d is the shrink-fitting ratio, in which δ represents the diameter difference of the shaft outer diameter and the sleeve inner diameter. In accordance with many years of experience, sleeve rolls usually have a shrink-fitting ratio $\delta/d = 0.4\times10^{-3}{\sim}1.0\times10^{-3}$. This phenomenon, which is due to small value of approximately $\delta/d < 0.4 \times 10^{-3}$ could make the interface prone to slippage, while large value of approximately $\delta/d > 1.0 \times 10^{-3}$ could lead to the sleeve fracture [6]. In this paper, $\delta/d = 0.5 \times 10^{-3}$ is used to study the interfacial slippage between sleeve and shaft. A study has been conducted by considering the shrink-fitting ratio effect on the interfacial slippage [18]. Friction coefficient μ controls the slippage resistance at the interface, whereby $\mu = 0.2$ was applied in experimental study and $\mu = 0.4$ was applied previously for surfaces of steel [1, 47]. This research uses a friction coefficient of $\mu = 0.3$ since a friction coefficient in the range of $\mu = 0.2$~0.4 are commonly used for the sleeve assembly type rolls.

5.2.3 Simulation results of rolling stress generated on the inner surface of the sleeve

5.2.3.1 Rolling stress σ_θ on the inner surface of the sleeve

The circumferential slippage sometimes occurs in the sleeve roll even though the resistance torque at the interface is set to be larger than the motor torque. In the previous studies, the interfacial slip was realized by the load shifting method described in Appendix A.1.

Fig. 5-7(a) shows the interfacial slip $u_{\theta,T=T_m}^{P(0)}(\theta)$, which is the relative displacement u_θ at $\theta = \theta$ when the standard drive torque is $T = T_m$ and the initial load $P = P_0$ is applied at $\varphi = 0$ as $P(0)$. Fig. 5-7(a) also shows $u_{\theta,T=T_m}^{P(0)\sim P(2\pi)}(\theta)$, which is the circumferential displacement u_θ when the standard rolling condition $P = P_0, T = T_m$ moves from $\varphi = 0$ to $\varphi = 2\pi$ as P(0)~P(2π). Fig. 5-‘(a) also shows $u_{\theta,T=T_m}^{P(0)\sim P(4\pi)}(\theta)$ when the standard rolling condition $P = P_0, T = T_m$ moves two rotations as P(0)~P(4π). As shown in Fig. 5-7(a), the displacement $u_{\theta,T=T_m}^{P(0)\sim P(\varphi)}(\theta)$ increases with increasing φ. Since the displacement

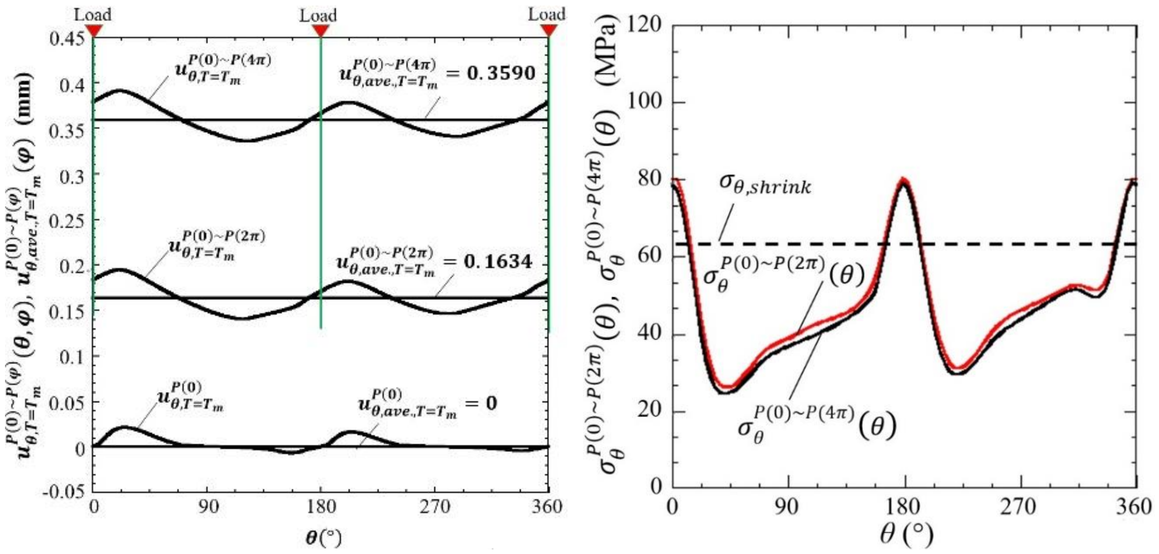

(a) Displacement distribution $u_{\theta,T=T_m}^{P(0)}$, $u_{\theta,T=T_m}^{P(0)\sim P(\pi)}$ and $u_{\theta,T=T_m}^{P(0)\sim P(2\pi)}$.

(b) Comparison of $\sigma_\theta^{P(0)\sim P(2\pi)}(\theta)$ and $\sigma_\theta^{P(0)\sim P(4\pi)}(\theta)$.

Fig. 5-7 Comparison of the displacement and stress distribution.

$u_{\theta,T=T_m}^{P(0)\sim P(\varphi)}(\theta)$ varies depending on θ, the average displacement is defined as in Eq. (5-2).

$$u_{\theta,ave.,T=T_m}^{P(0)\sim P(\varphi)} = \frac{1}{2\pi}\int_0^{2\pi} u_{\theta,T=T_m}^{P(0)\sim P(\varphi)}(\theta)d\theta \qquad (5-2)$$

As shown in Fig. 5-7(a), more clearly, the average displacement $u_{\theta,ave.,T=T_m}^{P(0)\sim P(\varphi)}$ increases due to the load shifting from $\varphi = 0$ to $\varphi = 4\pi$.

If such circumferential slip $u_{\theta,T=T_m}^{P(0)\sim P(\varphi)}(\theta)$ occurs in a real rolling roll, several scratches and partial seizures happen at the sleeve shrink-fitting surface. Then, the seizure growth with the roll rotation causes the surface roughness with a few millmeter depths. Due to the roughness, fatigue crack initiates and propagates at the sleeve inner surface causing the final fracture [6].

Since σ_θ is the dominant stress component and leads to such failure, the shrink-fitted surface stress σ_θ is emphasized in this paper. The stress

$\sigma_{\theta}^{P(0)\sim P(\varphi)}(\theta)$ is defined as the interface stress σ_{θ} due to the load shifting $P(0)\sim P(\varphi)$ from the angle $\varphi = 0$ $(\varphi = \pi)$ to $\varphi = \varphi$ $(\varphi = \varphi + \pi)$. As shown here, notation φ indicates the angle at which the load is shifting, and notation θ represents the position where the stress is evaluated.

Fig. 5-7(b) shows the stress distribution, $\sigma_{\theta,T=T_m}^{P(0)\sim P(2\pi)}(\theta)$, which is the stress σ_{θ} when the load $P = P_0$ moves one rotation as $\mathrm{P(0)\sim P(2\pi)}$. Fig. 5-7(b) also shows $\sigma_{\theta,T=T_m}^{P(0)\sim P(4\pi)}(\theta)$ when the load $P = P_0$ moves two rotations as $\mathrm{P(0)\sim P(4\pi)}$. As shown in Fig. 5-7(b), no large difference between σ_{θ} after one rotation and σ_{θ} after two rotations of the load P. In other words, the accumulation phenomenon observed in the displacement is not seen in the stress. For the fatigue risk evaluation, therefore, the stress obtained after two rotations can be always used irrespective of the number of the roll rotation.

Fig. 5-8 shows the stress distribution along the interface $\sigma_{\theta,T=T_m}^{P(0)\sim P(4\pi)}(\theta)$ when the load $P = P_0$ moves two rotations as $\mathrm{P(0)\sim P(4\pi)}$ in comparison with the stress distribution $\sigma_{\theta,T=1.5T_m,}^{1.5P(0)\sim 1.5P(4\pi)}(\theta)$ when the load $P = 1.5P_0$ moves as $\mathrm{P(0)\sim P(4\pi)}$. Under the load $P = P_0$, the maximum stress is $\sigma_{\theta max}^{P_0} = 79.4$ MPa and the minimum stress is $\sigma_{\theta,min}^{P_0} = 24.6$ MPa. On the other hand, under the load $P = 1.5P_0$, which is corresponding to the impact load when the rolled plate biting trouble occurs, the maximum stress is $\sigma_{\theta,max}^{1.5P_0} = 91.3$ MPa and the minimum stress is $\sigma_{\theta\ min}^{1.5P_0} = -24.7$ MPa. Here, the stress amplitude σ_a and the mean stress σ_m are expressed in Eq. (5-3) and Eq. (5-4).

$$\sigma_a = (\sigma_{\theta max} - \sigma_{\theta min})/2 \tag{5-3}$$

$$\sigma_m = (\sigma_{\theta max} + \sigma_{\theta min})/2 \tag{5-4}$$

For the stress σ_{θ} under the load $P = P_0$, the stress amplitude is $\sigma_a = 27.4$ MPa and mean stress is $\sigma_m = 52.0$ MPa. On the other hand, under the load $P = 1.5P_0$, the stress amplitude is $\sigma_a = 58.0$ MPa and mean stress is $\sigma_m = 33.3$ MPa. This

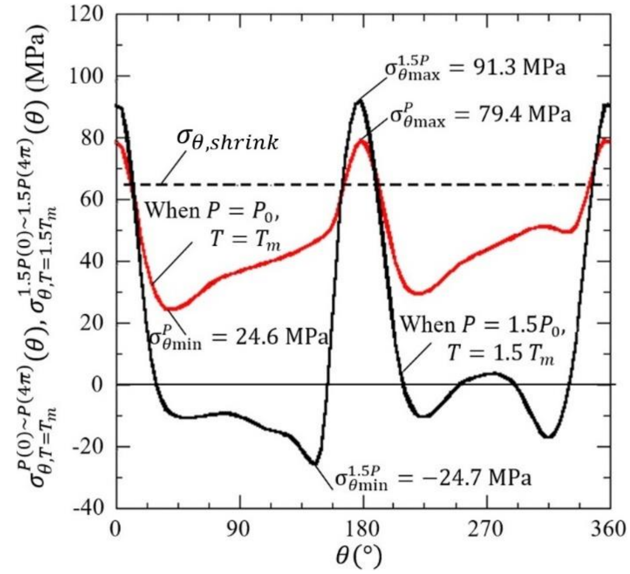

Fig. 5-8 Comparison of $\sigma_{\theta,T=T_m}^{P(0)\sim P(4\pi)}(\theta)$ and $\sigma_{\theta,T=1.5T_m}^{1.5P(0)\sim 1.5P(4\pi)}(\theta)$.

observation shows that by considering the impact force $P = 1.5P_0$, the stress amplitude σ_a is about 2.1 times and the mean stress σ_m is about 0.6 times from the stress under the standard condition $P = P_0$.

5.2.3.2 Contact stress σ_r on the inner surface of the sleeve

Previously the authors found the smaller contact stress region where the slip is promoted [19]. The region where the contact stress $\sigma_{r,T=T_m}^{P(0)\sim P(\varphi)}$ becomes smaller than the original shrink-fitted stress $\sigma_{r_{shrink}}$ as $\sigma_r^{P(0)\sim P(4\pi)} \leqq \sigma_{r_{shrink}}$ is characterized by a smaller contact stress region ℓ_{small}. Here, the shrink-fitting stress is the stress at the shrink-fitted surface without applying the load P which denotes as $\sigma_{r_{shrink}}$.

Fig. 5-9 shows the stress distribution $\sigma_{r,T=T_m}^{P(0)\sim P(4\pi)}(\theta)$ when the load $P = P_0$ moves as P(0)~P(4π) in comparison with the stress distribution $\sigma_{r,T=1.5T_m}^{1.5P(0)\sim 1.5P(4\pi)}(\theta)$ when the load $P = 1.5P_0$ moves as P(0)~P(4π). As shown in Fig. 5-9, the smaller contact stress region ℓ_{small} can be confirmed under the standard condition $P = P_0, T = T_m$ and also under the impact force condition $P =$

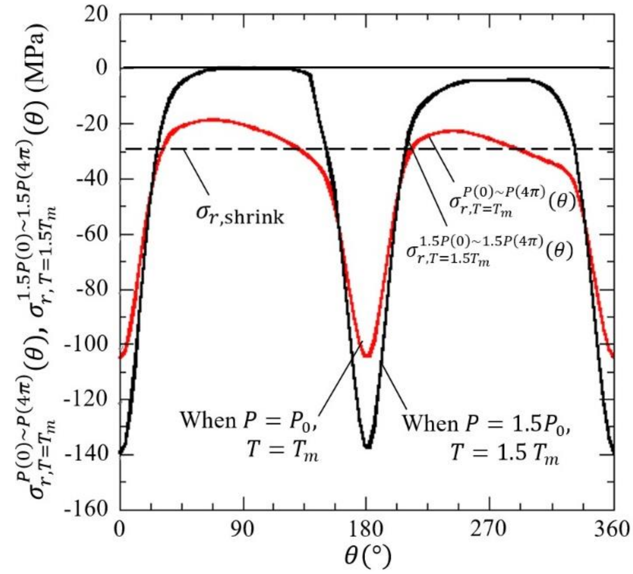

Fig. 5-9 Comparison of $\sigma_{r,T=T_m}^{P(0)\sim P(4\pi)}(\theta)$ and $\sigma_{r,T=1.5T_m}^{1.5P(0)\sim 1.5P(4\pi)}(\theta)$.

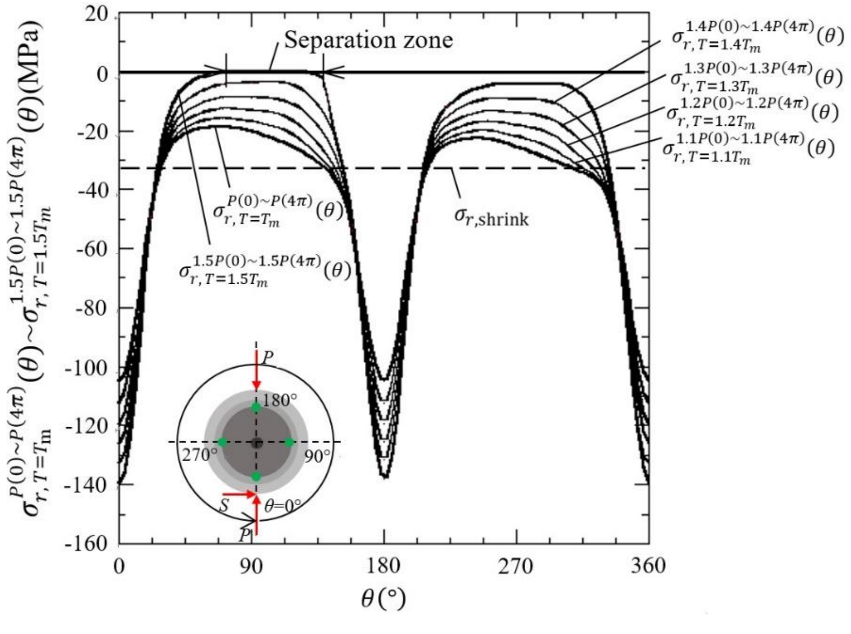

Fig. 5-10 Comparison of $\sigma_{r,T=T_\mathrm{m}}^{P(0)\sim P(4\pi)}(\theta)$ when P, T=P_0, T_m ~ 1.5P_0, 1.5T_m.

$1.5P_0, T = 1.5T_m$. In addition, with increasing the load from $P = P_0, T = T_m$ to $P = 1.5P_0, T = 1.5T_m$, the smaller contact stress region ℓ_{small} increases. It should be noted that under the condition of $P = 1.5P_0, T = 1.5T_m$, the zero contact stress region appears as $\sigma_{r,T=1.5T_m}^{1.5P(0)\sim 1.5P(4\pi)} \cong 0$ around $\theta = 90^o$where the sleeve and the shaft is separated. This region can be named the non-contact region. It may be concluded that under high load conditions, the non-contact region appears and accelerates the slippage.

To clarify the separation condition, Fig. 5-10 shows $\sigma_{r,T=T_{\mathrm{m}}}^{P(0)\sim P(4\pi)}(\theta)$ by varying the load from the standard condition $P = P_0, T = T_m$ to the impact force condition $P = 1.5P_0, T = 1.5T_m$. It was found that the separation occurs when $P/P_0 \geq 1.5$ and $T/T_m \geq 1.5$. Under the larger load $P/P_0 \geq 1.5$ and $T/T_m \geq 1.5$, the stress amplitude becomes much larger.

5.2.3.3 Residual stress and shrink-fitting stress

Based on the rolling stress $\sigma_\theta^{Rolling}$ obtained in the above discussion, the fatigue failure risk can be evaluated considering the crack initiation from the inner surface of the sleeve. In the real roll, however, when the sleeve roll is manufactured, the residual stress due to heat treatment is introduced. In the previous study [22], the residual simulation was performed during quenching and tempering for the conventional bimetallic solid rolls. In a similar way, the residual simulation is performed for the sleeve roll to obtain the residual stress in Fig. 5-5(b).

Fig. 5-11(a) shows the residual stress distribution σ_θ^{Res} at the central cross section z=0 after the quenching and tempering before the shrink-fitting. This is the results obtained from heat treatment analysis as shown in the previous study [22]. Fig.5-11(b) shows the stress distribution obtained by superposing the residual stress and the shrink-fitting stress as $\sigma_\theta^{Res+Shrink}$ at z=0 after the shrink-fitting.

As shown in Fig.5-11(b), the residual stress distribution after shrink-fitting the shaft has the maximum tensile stress $\sigma_\theta^{Res+Shrink} = 156$ MPa at

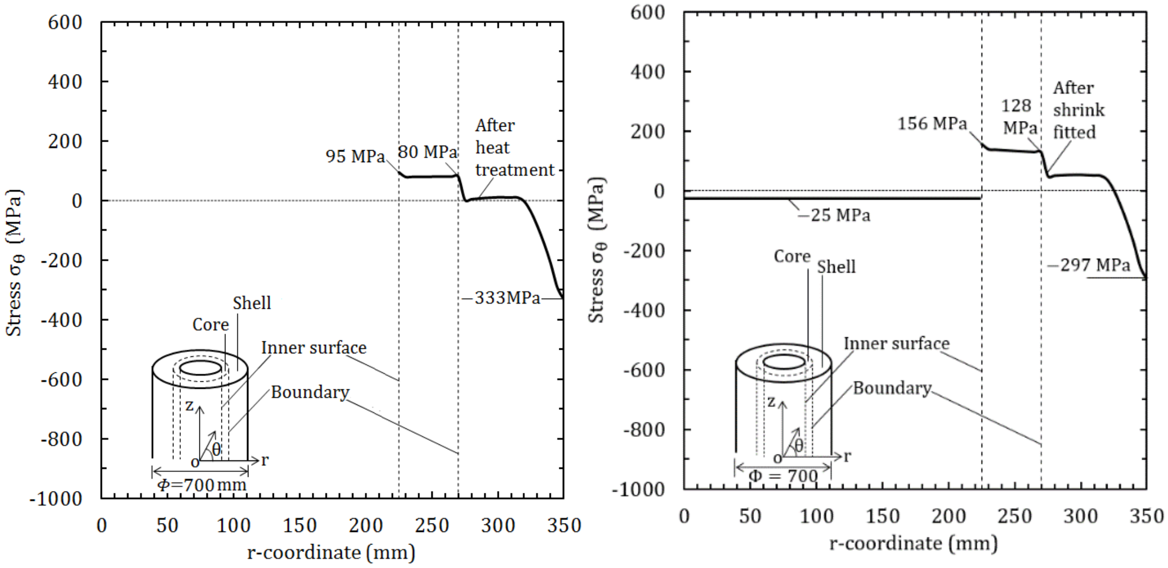

(a) Residual stress σ_θ distribution before shrink-fitting.

(b) Residual and shrink-fitting stress σ_θ after shrink-fitting.

Fig. 5-11 Stress distribution σ_θ obtained through sleeve heat treatment at $z = 0$; (a) Residual stress σ_θ before shrink-fitting, (b) Residual and shrink-fitting stress σ_θ after shrink-fitting.

$r = 225$ mm of the sleeve. In the next section, the fatigue strength will be discussed by considering the superposition of residual stress and the shrink-fitting stress as $\sigma_\theta^{Res+Shrink}$ [22] and the rolling stress $\sigma_\theta^{Rolling} = \sigma_{\theta,T=1.5T_m}^{1.5P(0)\sim1.5P(4\pi)}(\theta)$ at the inner surface of the sleeve in Fig. 5-8. In this evaluation, the stress σ_θ at the sleeve interface is focused since the stress σ_θ mainly controls the crack initiation.

5.2.4 Fatigue risk evaluation of the sleeve roll on the stress amplitude versus mean stress diagram ($\sigma_a - \sigma_m$ diagram) for the material having defect

In this section, the fatigue strength at the sleeve inner surface is evaluated in terms of the numerical simulation for the rolling stress $\sigma_\theta^{Rolling}$ in Section 5.2.3.1. In the authors' previous study, the numerical simulation of the

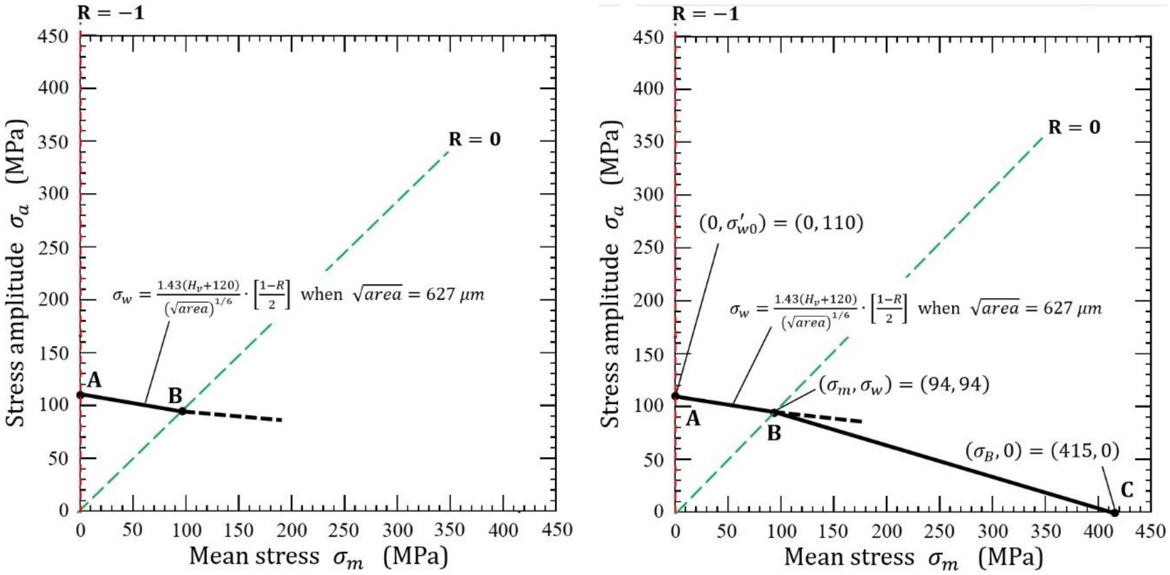

(a) Fatigue limit prediction at the defect size $\sqrt{area}$=627 μ m.

(b) Fatigue limit line for material with defect.

Fig. 5-12 Estimation of the fatigue limit of DCI including defects by using $\sqrt{area} = 627\ \mu\text{m}$

slippage was verified through the experiment by using a miniature roll. In this experiment [48], due to the slippage, the defect was observed and the dimensions are identified as shown in Fig. 4-14. Therefore, the fatigue risk should be evaluated by considering the rolling stress $\sigma_\theta^{Rolling}$ as well as the defect observed.

Regarding the fatigue limit for the engineering material having some defects, Equation (4) was proposed for the stress ratio range $-1 \leq \text{R} \leq 0$ [49].

$$\sigma_w = \frac{1.43(H_V+120)}{(\sqrt{area})^{1/6}} \left[\frac{1-R}{2}\right]^\alpha \text{ , } R = \frac{\sigma_{\theta min}}{\sigma_{\theta max}} \tag{5-5}$$

where H_V (kgf/mm^2) is the Vickers hardness of DCI and $area$ is the projected area of the defect.

Fig. 5-12(a) illustrates the fatigue limit curve for the DCI inner layer obtained from Eq. (5-5) as curve AB considering the defect whose defect size is characterized by $\sqrt{area} = 627$ μm (see Fig. 4-14). Since Eq. (5-5) is proposed in the range $-1 \leq \mathrm{R} \leq 0$, the curve AB is indicated in Fig. 5-12(a). Here, point B is the intersection of the curve obtained from Eq. (5-5) and the line $\mathrm{R} = (\sigma_m/\sigma_a - 1)/(\sigma_m/\sigma_a + 1) = -1$.

In Fig. 5-12(b), point C denotes the tensile strength of the DCI $\sigma_B = 415$ MPa. Recently, Ikeda et al. clarified that the strength of the circumferential notched specimen is larger than the strength of the plain specimen for the wide range of tensile speed and temperature [53]. Therefore, the static strength of DCI including some defects can be the same as the tensile strength of the DCI without defects $\sigma_B = 415$ MPa. In this way, in the range $\mathrm{R} \geq 0$, the straight line BC can be used as the fatigue limit line.

By considering the defect size $\sqrt{area} = 627$ μm observed in the miniature roll of the experimental study, Fig. 5-13(a) illustrates the fatige failure risk due to rolling stress $\sigma_\theta^{Rolling}$ as point E under the load $\mathrm{P} = 1.5P_0$ corresponding to the impact force during rolling. Point F in Fig. 5-13(a) also illustrates the fatige failure risk evaluated by superposing the shrink-fitting stress σ_θ^{Shrink} and the residual stress σ_θ^{Res} to the rolling stress $\sigma_\theta^{Rolling}$ as $\sigma_\theta^{Res+Shrink} + \sigma_\theta^{Rolling} = 189.3$ MPa.

Since the real roll diameter is about 10 times larger than the miniature roll, instead of the defect size $\sqrt{area} = 627$ μm, the double sizes of the defect with $\sqrt{area} = \sqrt{\pi(2a)(2b)/2}$=$627 \times 2 = 1254$ μm is considered and points A' and B' are plotted. Fig. 5-13(b) illustrates the fatigue failure risk due to rolling stress $\sigma_\theta^{Rolling}$ as point E under the load $\mathrm{P} = 1.5P_0$ corresponding to the impact force during rolling. Point F in Fig. 5-13(b) also illustrates the fatigue failure risk evaluated by superposing the shrink-fitting stress σ_θ^{Shrink} and the residual stress

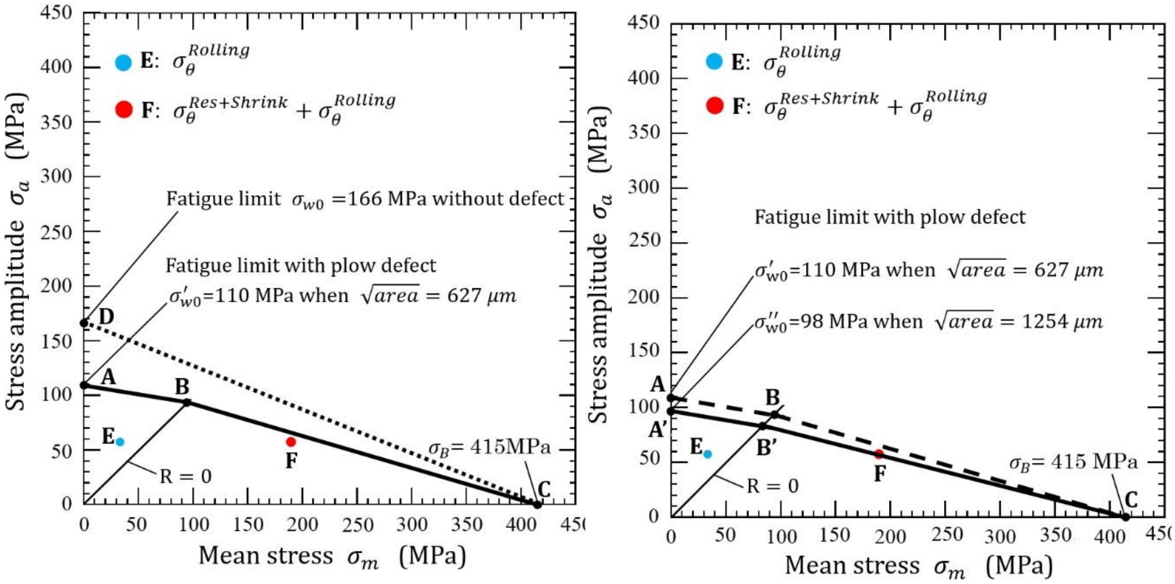

(a) Fatigue limit diagram to evaluate two critical points.

(b) Fatigue limit diagram by considering real roll defect.

Fig. 5-13 Stress amplitude σ_a vs. mean stress σ_m diagram for σ_B = 415 MPa, σ'_{w0} =110 MPa when $\sqrt{area}$=627 μm and σ''_{w0} =98 MPa when $\sqrt{area}$=1254 μm.

σ_θ^{Res} to the rolling stress $\sigma_\theta^{Rolling}$ as $\sigma_\theta^{Res+Shrink} + \sigma_\theta^{Rolling} = 189.3$ MPa. Point F is located on the slightly dangerous side.

The fatigue failure risk of the bimetallic solid roll studied in the recent paper is indicated in Appendix A.3 [50,51]. In the solid bimetallic roll, since the failures happened as the debonding at HSS/DCI boundary [5, 52], the risk of fatigue failure was evaluated focusing on the stress σ_r. The results show that if there is no slip damage, the fatigue strength of the sleeve roll is not very smaller compared to the fatigue strength of the solid roll with no shrink-fitting (see Fig. 5-13). If the interfacial slip can be prevented by providing a key between the sleeve and the shaft for example, the risk of fatigue can be the same of the solid bimetallic roll.

5.2.5 Conclusion

To develop next generation rolls, the fatigue strength of the sleeve roll is considered in this paper. The stress variation is focused during the roll rotation considering the sleeve slippage. The effect of the slip damage on the fatigue strength is discussed by considering the defect dimensions observed at the shrink-fitted surface previously reported. Then, the fatigue risk of the sleeve roll is evaluated by applying the projected area $\sqrt{area}$ of the defect. The conclusions can be summarized in the following way.

1. During the roll rotation, the maximum stress, the minimum stress, and stress amplitude at the interface were clarified when the slip occurs at the shrink-fitted interface (see Figure 5-7). No large difference can be seen between the stress after one rotation and the stress after two rotations. Although the interfacial displacement expressing the slippage increases with increasing the roll rotation, such an accumulation phenomenon cannot be seen in the stress.
2. Under the impact loading conditions when the rolled plate biting trouble occurs, the stress amplitude becomes about twice of the stress under the standard loading conditions (see Figure 5-8).
3. The fatigue failure risk of the bimetallic sleeve assembly type roll was evaluated considering the defect dimensions observed in the previous studies under impact loading condition. The results show that if there is no slip damage, the fatigue strength of the sleeve roll is not very smaller compared to the fatigue strength of the solid roll with no shrink-fitting (see Figure 5-13(a)).

References for Chapter 5

[1] Shimoda H, Onodera S, Hori K. Study on the residual deflection of large sleeved back-up rolls: 4th Report, Residual stresses of sleeved rolls. Trans Jpn Soc Mech Eng 1966;32:689-94.

[2] Irie T, Takaki K, Tsutsunaga I, Sano Y. Steel strip and section steel and thick rolling, processing. Tetsu-to-Hagane 1979;65:293.

[3] Takigawa H, Hashimoto K, Konno G, Uchida S. Development of forged high-speed-steel roll for shaped steel. CAMP-ISIJ 2003;16:1150-3.

[4] Sano Y. Recent advances in rolling rolls. Proc of the No. 148-149 Nishiyama Memorial Technology Course, Tokyo, Japan; 1993, p. 193-226.

[5] Sano Y. Fatigue failure problem in the inside of roll body for hot strip rolling-Crack initiation problem and its estimation in the actual plant. The 245th JSMS Committee on Fatigue of Materials and The 36th JSMS Committee on Strength Design, Safety Evaluation; 1999, p. 40.

[6] Matsunaga E, Tsuyuki T, Sano Y. Optimum shrink fitting ratio of sleeve roll (Strength design of shrink fitted sleeve roll for hot strip mill-1). CAMP-ISIJ 1998;11:362. https://ci.nii.ac.jp/naid/10002551803.

[7] Tutumi S, Hara S, Yoshi S. The residual deflection of sleeved backup-up rolls. Tetsu-to-Hagane 1971;57(5):818-22.

[8] Spuzic S, Strafford KN, Subramanian C, Savage G. Wear of hot rolling mill rolls: an overview. Wear 1994;176(2):261-71. https://doi.org/10.1016/0043-1648(94)90155-4.

[9] Noda NA, Hu K, Sano Y, Ono K, Hosokawa Y. Residual stress simulation for hot strip bimetallic roll during quenching. Steel Res Int 2016;87(11):1478-88. https://doi.org/10.1002/srin.201500430.

[10]Noda NA, Sano Y, Takase Y, Shimoda Y, Zhang G. Residual deflection mechanism for back-up roll consisting of shrink-fitted sleeve and arbor. J JSTP 2017;58:66.

[11]Hu K, Xia Y, Zhu F, Noda NA. Evaluation of thermal breakage in bimetallic work roll considering heat treated residual stress combined with thermal stress during hot rolling. Steel Res Int 2017;89(4):1700368. https://doi.org/10.1002/srin.201700368.

[12]Goto K, Matsuda Y, Sakamoto K, Sugimoto Y. Basic characteristics and microstructure of high-carbon high speed steel rolls for hot rolling mill. ISIJ Int 1992;32:1184-9.

[13]Ryu JH, Ryu HB. Effect of thermal fatigue property of hot strip mill work roll materials on the rolled-in defects in the ultra-low carbon steel strips. ISIJ Int 2003;43(7):1036-9. https://doi.org/10.2355/isijinternational.43.1036

[14]Park JW, Lee HC, Lee S. Composition, microstructure, hardness, and wear properties of high-speed steel rolls. Metall Mater Trans A 1999;30:399-409.

[15]Hattori T, Kamitani Y, Sugino K, Tomita H, Sano Y. Super cermet rolls for manufacturing ultra-fine-grained steel. International Conference on Tribology in Manufacturing Processes ICTMP 2007 International Conference 24-26 September 2007, Yokohama.

[16]Hamayoshi S, Ogawa E, Shimiz K, Noda NA, Kishi K, Koga S. Development of large ceramic rolls for continuous hot-dip galvanized steel sheet production lines. Sokeizai 2010;51(12):54-9.

[17]Noda NA, Sakai H, Sano Y, Takase Y, Shimoda Y. Quasi-equilibrium stress zone with residual displacement causing permanent slippage in shrink-fitted sleeve rolls. Metals 2018;8(12):998. https://doi.org/10.3390/met8120998.

[18]Sakai H, Noda NA, Sano Y, Zhang G, Takase Y. Effect of driving torque on the interfacial creep for shrink-fitted bimetallic work roll. Tetsu-to-Hagane 2019;105(12):1126-34. https://doi.org/10.2355/tetsutohagane.TETSU-2019-048.

[19]Noda NA, Rafar RA, Sakai H, Zheng X, Tsurumaru H, Sano Y, Takase Y. Irreversible interfacial slip in shrink-fitted bimetallic work roll promoted by roll deformation. Eng Fail Anal 2021;126:105465. https://doi.org/10.1016/j.engfailanal.2021.105465

[20]Rafar RA, Noda NA, Tsurumaru H, Sano Y, Takase Y. Effect of shaft's rigidity and motor torque on interfacial slip for shrink-fitted bimetallic work roll. In: Parinov IA. Chang SH, Kim YH, Noda NA, editors. Physics and mechanics of new materials and their applications, Springer Cham; 2021, p. 381-8.

[21]Noda NA, Rafar RA, Sano Y. Stress due to interfacial slip causing sleeve fracture in shrink-fitted work roll. Int J Mod Phys B 2021, p. 2140020. https://doi.org/10.1142/S0217979221400208

[22]Noda NA, Sano Y, Aridi MR, Tsuboi K, Oda N. Residual stress differences between uniform and non-uniform heating treatment of bimetallic roll: Effect of creep behavior on residual stress. Metals 2018;8(11):952.

[23]Soda N. Bearing. Iwanami Shoten, Tokyo; 1964, p.196-203.

[24]Imai. Lubrication. 1959;4:307.

[25]Murata J, Onizuka T. Generation mechanism of inner ring creep. Koyo Eng J 2005;166:41-7.

[26]Niwa T. A creep mechanism of rolling bearings. NTN Tech Rev 2013;81:100-103.

[27]Ten, Sakajiri, Takemura, Yukawa. NSK Tech J 2006;680:13.

[28]New Bearing Doctor: Diagnosis of bearing problems. Objective: Smooth & reliable operation. NSK, https://www.nsk.com/common/data/ctrgPdf/e7005c.pdf. 1997 [accessed 28 June 2020].

[29]Zhan J, Takemura H, Yukawa K. A study on bearing creep mechanism with FEM simulation. Proceedings of IMECE2007, 2007 Seattle, Washington, USA. https://doi.org/10.1115/IMECE2007-41366.

[30]Zhan J, Yukawa K, Takemura H. Analysis of bearing outer ring creep with FEM. Advanced Tribology, 2009, Springer, Berlin, Heidelberg. https://doi.org/10.1007/978-3-642-03653-8_74.

[31]Noguchi S, Ichikawa K. A study about creep between inner ring of ball bearing and shaft. Proceeding of Academic Lectures of the Japan Society for Precision Engineering, 2010, Japan. https://doi.org/10.11522/pscjspe.2010A.0.565.0.

[32]Teramoto T, Sato Y. Prediction method of outer ring creep phenomenon of ball bearing under bearing load. Trans Of Society of Automotive Eng of Japan 2015;46:355-60. https://doi.org/10.11351/jsaeronbun.46.355.

[33]Bovet C, Zamponi L. An approach for predicting the internal behaviour of ball bearings under high moment load. Mech Mach Theory 2016;101:1-22. https://doi.org/10.1016/j.mechmachtheory.2016.03.002.

[34]Maiwald A, Leidich E. FE simulations of irreversible relative movements (creeping) in rolling bearing seats –Influential parameters and remedies. World Congress on Engineering and Computer Science 2013 Vol II, San Francisco, USA. http://www.iaeng.org/publication/WCECS2013/WCECS2013_pp1030-1035.pdf.

[35]Schiemann T, Porsch S, Leidich E, Sauer B. Intermediate layer as measure against rolling bearing creep. Wind Energy 2018;21:426-40. https://doi.org/10.1002/we.2170.

[36]Miyazaki T, Noda NA, Ren F, Wang Z, Sano Y, Iida K. Analysis of intensity of singular stress field for bonded cylinder and bonded pipe

in comparison with bonded plate. Int J Adhes Adhes 2017;77:118-37. https://doi.org/10.1016/j.ijadhadh.2017.03.019.

[37]Noda NA, Miyazaki T, Li R, Uchikoba T, Sano Y, Takase Y. Debonding strength evaluation in terms of the intensity of singular stress at the interface corner with and without fictitious crack. Int J Adhes Adhes 2015;61:46-64. https://doi.org/10.1016/j.ijadhadh.2015.04.005.

[38]Noda NA, Uchikoba T, Ueno M, Sano Y, Iida K, Wang Z, Wang G. Convenient debonding strength evaluation for spray coating based on intensity of singular stress. ISIJ Int 2015;55(12):2624-30. https://doi.org/10.2355/isijinternational.ISIJINT-2015-458.

[39]Wang Z, Noda NA, Ueno M, Sano Y. Optimum design of ceramic spray coating evaluated in terms of intensity of singular stress field. Steel Res Int 2016;88:1-9. https://doi.org/10.1002/srin.201600353.

[40]Noda NA, Chen X, Sano Y, Wahab MA, Maruyama H, Fujisawa R, Takase Y. Effect of pitch difference between the bolt-nut connections upon the anti-loosening performance and fatigue life. Mater Des 2016;96:476-89. https://doi.org/10.1016/j.matdes.2016.01.128.

[41]Noda NA, Takaki R, Shen Y, Inoue A, Sano Y, Akagi D, Takase Y, Galvez P. Strain rate concentration factor for flat notched specimen to predict impact strength for polymeric materials. Mech Mater 2019;131:141-57. https://doi.org/10.1016/j.mechmat.2019.01.011.

[42]Matsuda S, Suryadi D, Noda NA, Sano Y, Takase Y, Harada S. Structural design for ceramics rollers used in the heating furnace. Trans JSME Ser A 2013;79(803):989-99.

[43]Noda NA, Suryadi D, Kumasaki S, Sano Y, Takase Y. Failure analysis for coming out of shaft from shrink-fitted ceramics sleeve. Eng Fail Anal 2015;57:219-35. https://doi.org/10.1016/j.engfailanal.2015.07.016.

[44]Noda NA, Xu Y, Suryadi D, Sano Y, Takase Y. Coming out mechanism of steel shaft from ceramic sleeve. ISIJ Int 2016;56(2):303-10. https://doi.org/10.2355/isijinternational.ISIJINT-2015-558.

[45]Zhang G, Sakai H, Noda NA, Sano Y, Oshiro S. Generation mechanism of driving out force of the shaft from the shrink fitted ceramic roll by introducing newly designed stopper. ISIJ Int 2019;59(2):293-9. https://doi.org/10.2355/isijinternational.ISIJINT-2018-615.

[46]Marc Mentat team: Theory and User Information, Vol. A, MSC, Software, Tokyo;2008, p.713.

[47]Misumi-vona Top, Technical information, Dry coefficient of friction. https://jp.misumi-ec.com/tech-info/categories/plastic_mold_design/p107/c0874.html. [accessed 2 March 2019].

[48]Rafar RA, Noda NA, Taruya Y, Sano Y, Takase Y, Kondo K. Experimental verification of interfacial slip generation for shrink-fitted bimetallic work roll by using miniature roll, the 9th International Symposium on Applied Engineering and Sciences 2021 (SAES2021), 5th-8th December 2021.

[49]Murakami Y. Metal fatigue: effects of small defects and nonmetallic inclusions. Elsevier Science, Oxford UK; 2002.

[50]Aridi MR, Noda NA, Sano Y, Takata K, Sun Z. Fatigue Failure Risk Evaluation of Bimetallic Rolls in 4-High Hot Rolling Mills. Steel Res Int 2021;2100313.

[51]Aridi MR, Noda NA, Sano Y, Takata K, Sun Z. Fatigue Failure Analysis for Bimetallic Work Roll in Hot Strip Mills. Fatigue Fract Eng Mater Struct 2021. DOI: 10.1111/ffe.13651.

[52]Sano Y, Kimura K. Statistical analysis about crack and spalling on work roll for hot strip mill finishing rear stands. Tetsu-to-Hagane 1987;73:78-85.

[53] Ikeda T, Noda NA, Sano Y. Conditions for notch strength to be higher than static tensile strength in high-strength ductile cast iron. Eng Fract Mech 2019;206:75-88.

6 Residual stress simulation for bimetallic sleeve roll

6.1 Introduction

Fig. 6-1 compares a bimetallic solid roll and bimetallic sleeve roll where the shaft is shrink-fitted into a hollow cylinder. The sleeve rolls are practically and successfully used as the backup rolls with a diameter exceeding 1000mm and the large rolls for H-shaped steel rolling [1-13]. Although in Fig. 6-1(a) the shell cannot be replaced, in Fig. 6-1(b) the sleeve can be replaced after the sleeve wear exceeds the threshold amount. Recently, the authors investigated several peculiar problems such as residual roll bending [4-7] and the sleeve cracking caused by the sleeve circumferential slippage [8-13].

The sleeve rolls are also practically used as hot finishing rolling rolls having a smaller diameter than large H-shaped steel rolling. In this case, HSS bimetallic rolls are widely used as shown in Fig. 6-1(b) since they have excellent wear resistance, rough skin resistance, and thermal crack resistance [5]. Several efforts have be done to develop those hot finishing sleeve rolls since they are difficult to be manufactured due to the smaller sleeve thickness (D-d') / 2 where D=the body diameter and d'=the shaft diameter as shown in Fig. 6-1(b). Since the irreversible slip of the sleeve is the problem that has to be solved, the effect of rolling load and the effect of shrink-fitting conditions on the sleeve slip were investigated in the numerical simulation [9-13]. Since the sleeve slip may cause cracking and failure at the inner surface of the sleeve, it is necessary to reduce the residual stress at the inner surface.

Regarding HSS/DCI bimetallic solid rolls (HSS: high-speed steel, DCI: ductile casting iron) in Fig. 6-1(a), the residual stress was clarified during quenching and tempering through FEM simulations in the previous studies[3-8, 14-17]. However, regarding HSS/DCI bimetallic sleeve roll in Fig. 6-1(b), no

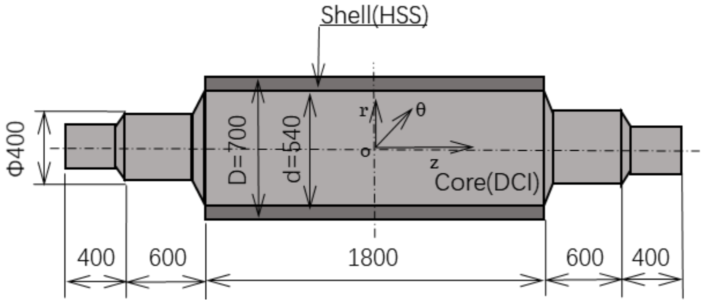

(a) Bimetallic solid roll

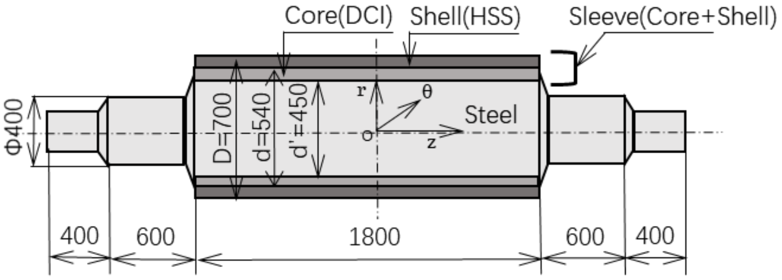

b) Bimetallic sleeve roll having shrink-fitted shaft

Fig. 6-1 Solid roll and sleeve roll dimensions (mm)

study is available for the residual stress. The target compressive residual stress at the outer surface can be in the range σ_θ=200～400MPa and the target tensile residual stress at the inner surface can be in the range $\sigma_\theta \leq$200MPa. In this study, therefore, two different manufacturing methods will be considered for the sleeve roll to satisfy the suitable residual stress in Fig. 6-2; one is turning inside of the solid roll after heat treatment and the other is heat treatment after turning inside of the solid roll. After a suitable manufacturing method is found, the fatigue risk of the sleeve will be discussed on the basis of the residual stress and rolling stress by comparing the sleeve bimetallic roll and the solid bimetallic roll.

6.2 Analysis method

6.2.1 Sleeve roll manufacturing process

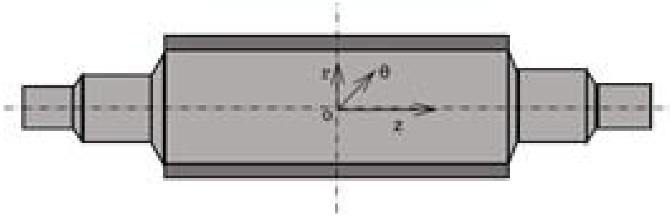

(a) Bimetallic roll annealed before quenching

(b) Solid heat treatment

(c) Sleeve heat treatment

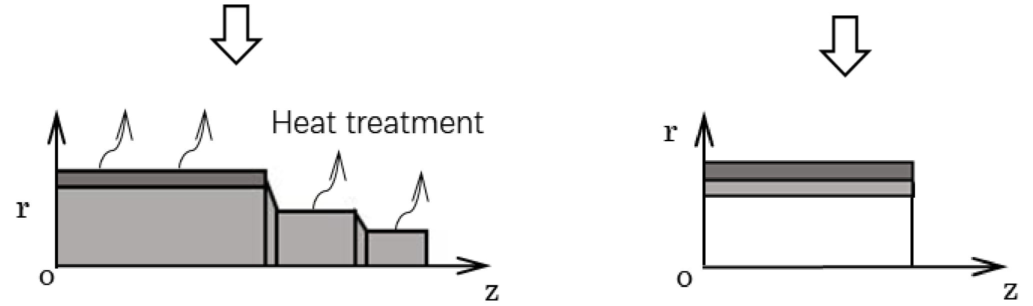

(b1) Quenching and tempering of solid roll

(c1) Turning inside

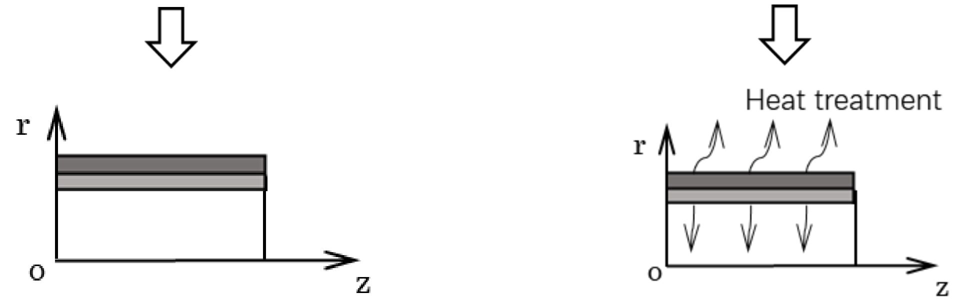

(b2) Turning inside

(c2) Quenching and tempering of hollow roll

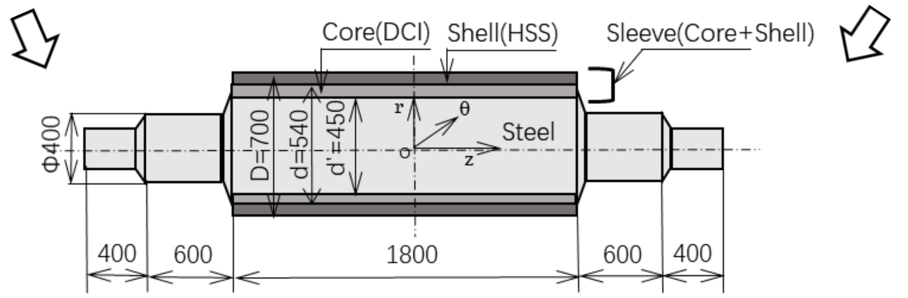

(d) Bimetallic sleeve roll having shrink-fitted shaft manufactured by (b) solid heat treatment and (c) sleeve heat treatment

Fig. 6-2 Two types of manufacturing methods for bimetallic sleeve roll

Fig. 6-2 illustrates the manufacturing method of the sleeve roll. Here, we consider the two different manufacturing processes from the solid roll in Fig. 6-2(a) to the sleeve roll in Fig. 6-2(e). As shown in Fig. 6-2(b), one is named "solid heat treatment" where turning the inner sleeve after the heat treatment of the solid roll. In this method, first, quenching and tempering as shown in Fig. 6-2(b1); second, turning inside as shown in Fig. 6-2(b2); then, shrink-fitting the shaft as shown in Fig. 6-2(e). On the other hand, as shown in Fig. 6-2(c), the other is named "sleeve heat treatment" where turning the inner sleeve before the heat treatment. In this method, first, turning inside as shown in Fig. 6-2(c1); second, quenching and tempering as shown in Fig. 6-2(c2); then, shrink-fitting the shaft as shown in Fig. 6-2(e).

Instead of starting from the solid roll in Fig. 6-2(a), the actual manufacturing often starts from an intermediate shape between Fig. 6-2(b1) and Fig. 6-2(c1) where small removable allowance remains at the inside of the sleeve. Specifically, by using centrifugal casting, a similar shape of Fig. 6-2(c1) with a small allowance at the inner surface is produced, and then turning is processed into an inner diameter. In this study, the residual stress of the solid roll in Fig. 6-2(b1) analyzed in the previous paper [14-17] is used to clarify the suitable manufacturing process. The target compressive residual stress at the outer surface can be in the range σ_θ=200～400MPa and the target tensile residual stress at the inner surface can be $\sigma_\theta \leq$200MPa. The residual stress simulation of the solid roll in Fig. 6-2(b1) is indicated in Appendix A.2. The residual stress distributions are shown in Fig. A-6. Instead, the residual stress simulation of the sleeve roll in Fig. 6-2(c2) will be indicated in Section 6-4. The residual stress distributions of the sleeve will be shown in Figure 10, Fig. 6-11 and Fig. 6-12.

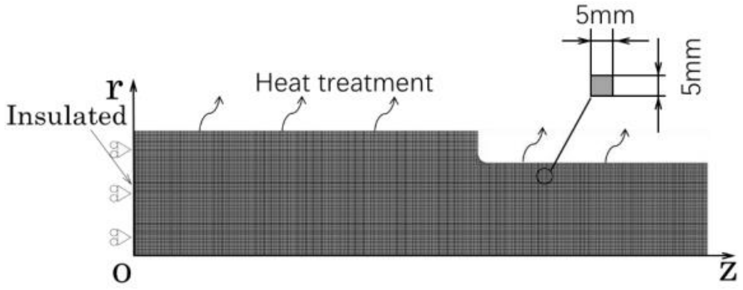

Fig. 6-3 Boundary condition for the solid roll

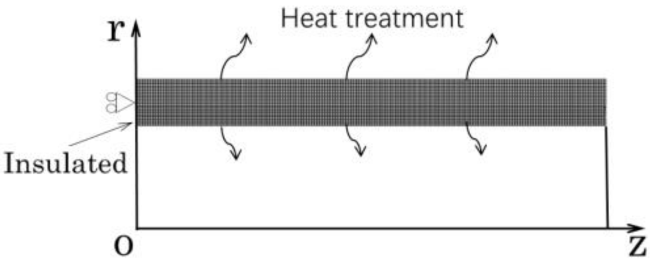

Fig. 6-4 Boundary condition for bimetallic sleeve roll

6.2.2 Analytical model and boundary conditions

Fig. 6-1(a) shows the HSS/DCI solid roll analyzed in the previous paper whose body diameter D = 700mm with a 60mm outer layer thickness and 1800mm length [14,15]. The outer layer is made of HSS and the inner layer including the shaft is made of DCI manufactured by centrifugal casting. Fig. 6-2 shows the detail dimensions of the bimetallic sleeve roll treated in this paper. The external shape and dimensions are the same as those of the solid roll in Fig. 6-1(a). The sleeve has a 125mm thickness and a 450mm inner diameter shrink-fitted with a shrink-fitting allowance δ. Figs. 6-3 and 6-4 show the axisymmetric analysis model applying 5mm × 5mm mesh for the thermal elastic-plastic finite element method using software MSC.Marc/Mentat 2012. During quenching the solid roll in Fig. 6-3 and the sleeve roll in Fig. 6-4, the quenching temperature at the surface is mainly provided in the simulation. Another simulation based on the ambient temperature and the heat transfer coefficient α as well as the radiation

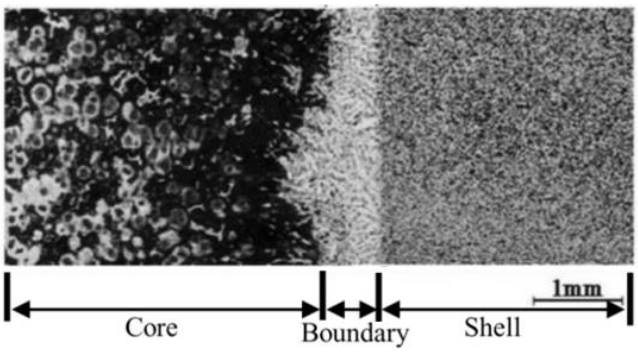

Fig. 6-5 Microstructure around HSS/DCI boundary [16-18].

effect is also used to express the measured sleeve temperature. Several physical properties such as elastic modulus, thermal expansion coefficient, specific heat, density, stress-strain characteristics, thermal conductivity, Poisson's ratio are used with certain temperature intervals from 23ºC to 1000ºC at the outer and inner layers. Then, the boundary conditions are set as shown in Fig. 6-3 and Fig. 6-4 to perform the elastic-plastic finite element method simulation.

6.2.3 Mechanical properties of outer and inner layer materials

Fig. 6-5 shows the microstructure around the HSS/DCI boundary [16-18]. The fine carbides with white color are uniformly distributed in the outer HSS layer side; however, toward the internal DCI layer side, coarse carbides can be seen. In the inner layer DCI, the spherical graphite surrounded by the ferrite is distributed uniformly around the boundary showing a healthy composite structure. Table 6-1 shows the material properties of the outer HSS layer and the inner DCI layer at room temperature including the effects of phase transformation. The properties at high temperatures used in this simulation are obtained experimentally by using the specimen cut-out from the roll manufactured in the same way. Fig. 6-6 shows the stress-strain diagram of HSS and DCI at high temperature.

Table 6-1 Mechanical properties for the shell and the core at room temperature

Property	Shell (HSS)	Core (DCI)
0.2 % proof stress (MPa)	1282	415
Young's modulus (GPa)	233	173
Poisson's ratio	0.3	0.3
Density (kg·m^{-3})	7.6	7.3
Thermal expansion coefficient (K^{-1})	12.6×10^{-6}	13.0×10^{-6}
Thermal conductivity (W/mK)	20.2	23.4
Specific heat (J/kgK)	0.46	0.46

6.3 Residual stress analysis of bimetallic roll

6.3.1 Solid heat treatment type

Fig. 6-7(a) shows the residual stress distribution σ_θ of the solid heat treatment type in Fig. 6-2(b2) after turning the inner portion of the bimetallic roll just after the quenching and tempering the solid roll.

The result in Fig. 6-7(a) is obtained by using the residual stress of the solid roll in Fig. 6-2(b1) studied previously [14-17] by adding turning process analysis in Fig. 6-2(b2). Fig. 6-7(a) shows the σ_θ distribution at z = 0 including the maximum tensile stress σ_θ = 463MPa at r = 270mm. The residual stress in the inner layer at z = 0 is in the range σ_θ = 453MPa ~463MPa exceeding the tensile strength σ_θ = 415MPa. Fig. 6-7(b) shows the residual stress distribution after shrink-fitting the shaft where the maximum tensile stress increases to σ_θ = 514MPa at r = 225mm.

6.3.2 Sleeve heat treatment type

Fig. 6-8(a) shows the residual stress distribution σ_θ at the cross-section z = 0 of the sleeve heat treatment type in Fig. 6-2(c2) after quenching and tempering the sleeve roll. Fig. 6-8(a) shows the distribution σ_θ at the cross-section z = 0, and Fig. 6-8(a) shows the stress distribution after shrink fitting including the maximum stress σ_θ = 95MPa at (r,z)=(225mm, 0).

After considering the whole longitudinal section, it is confirmed that $\sigma_\theta = 95\text{MPa}$ in Fig. 6-8(a) is the maximum tensile stress of the whole region. Therefore, the residual stress distribution σ_θ at z=0 can be used to discuss the validity of sleeve heat treatment. The maximum residual stress $\sigma_\theta = 95\text{MPa}$ which is much smaller than the maximum stress in Fig. 6-7(a) and the tensile strength $\sigma_\theta = 415\text{MPa}$. However, it should be noted that the compressive residual stress $\sigma_\theta = 333\text{MPa}$ at the outer surface is large enough to prevent the fatigue crack extension. It can be concluded that the sleeve heat treatment type as shown in Fig. 6-2(c) is useful for manufacturing the sleeve roll. Fig. 6-8(b) shows the residual stress distribution after shrink-fitting the shaft where the maximum tensile stress $\sigma_\theta = 156\text{MPa}$ at r = 225mm is small enough and the maximum compressive stress $\sigma_\theta = 297\text{MPa}$ is still large enough.

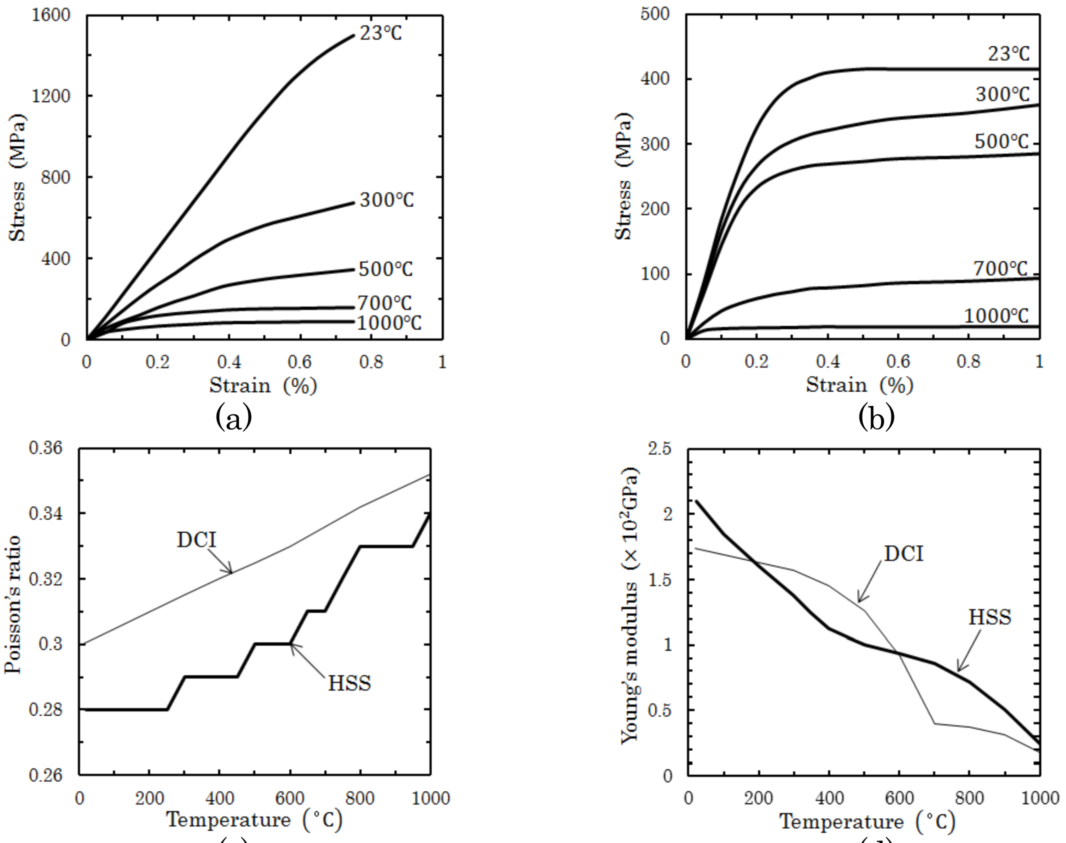

(a) (b)

(c) (d)

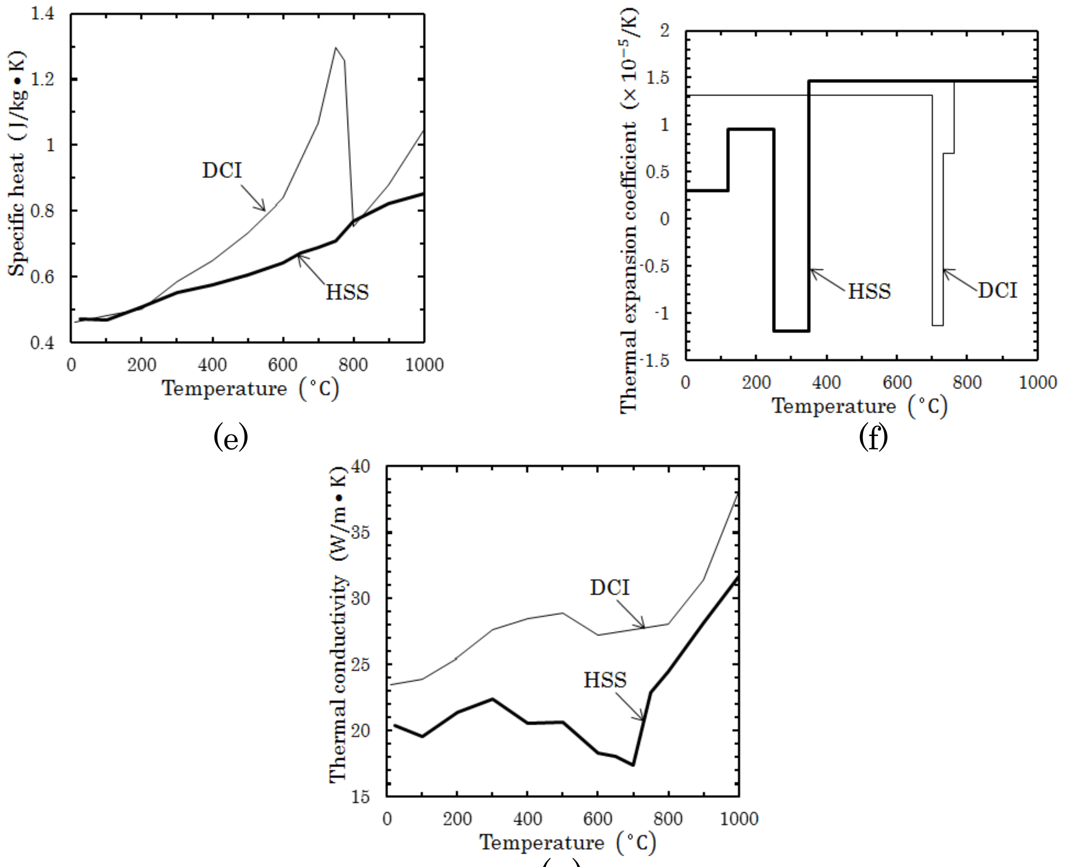

(e)

(f)

(g)

Fig. 6-6 (a) Stress-strain for HSS; (b) Stress-strain for DCI; (c) Poisson's ratio; (d) Young's modulus; (e) Specific heat; (f) Thermal expansion coefficient; (g) Thermal conductivity.

6.3.3 Comparison of the residual stress of bimetallic roll for both manufacturing methods

The above discussion clarified that the tensile residual stress of Fig. 6-8(a) is smaller than the tensile residual stress in Fig. 6-7(a). In the solid heat treatment method, when turning the inside of the sleeve, the tensile stress of the inner layer increases due to the reduction of the cross-sectional area. Instead, in sleeve heat treatment method, due to the heat treatment performed after the turning inside, the tensile residual stress at the inner sleeve surface is largely reduced. It can be concluded that the sleeve heat treatment is suitable for manufacturing sleeve rolls since the smaller tensile residual stress smaller and the compressive stress at the outer surface is large enough.

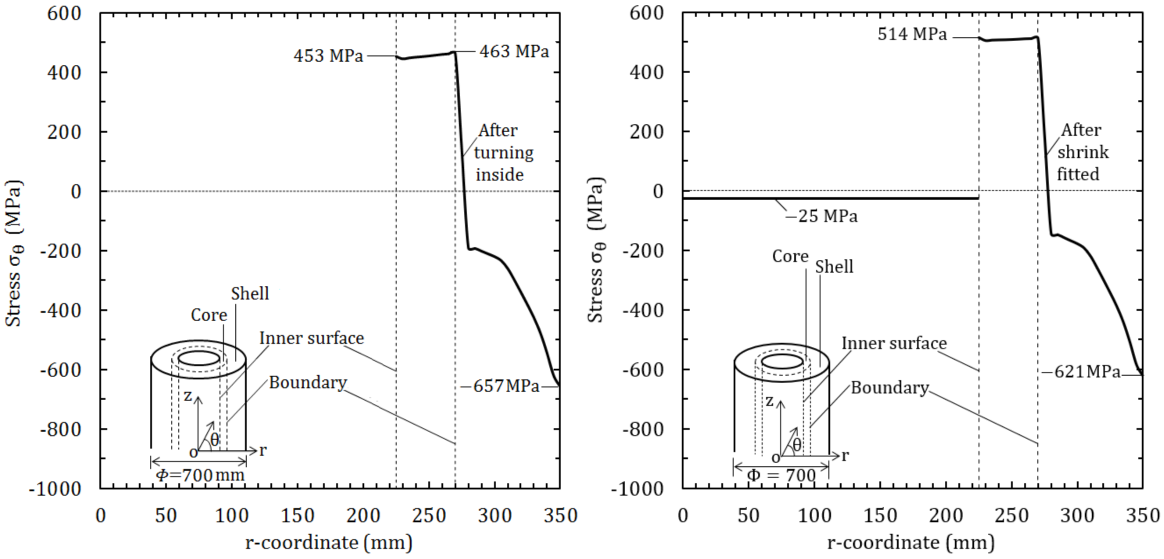

(a) Residual stress σ_θ distribution before shrink-fitting in Fig. 6-2(b2).

(b) Residual stress σ_θ distribution after shrink-fitting in Fig. 6-2(e).

Fig. 6-7 Residual stress σ_θ distribution obtained through solid heat treatment; (a) Residual stress σ_θ distribution at $z = 0$ before shrink-fitting, (b) Residual stress σ_θ distribution at $z = 0$ after shrink-fitting.

6.4 Residual stress simulation for the bimetallic sleeve roll

As shown in Appendix A.2, the quenching and tempering simulation was performed for the solid roll in Fig. 6-2(b1) in the previous papers [14-17]. In this paper, the quenching and tempering simulation is performed for the bimetallic sleeve in Fig. 6-2(c2) to compare the residual stress.

6.4.1 Temperature and stress change during the quenching

In this Section, the residual stress during quenching is analyzed and the residual stress generation mechanism is discussed. Fig. 6-9(a) illustrates the quenching history including the heating process in Region I and the quenching process in Region II and Region III. Fig. 6-9(b) illustrates corresponding stress,

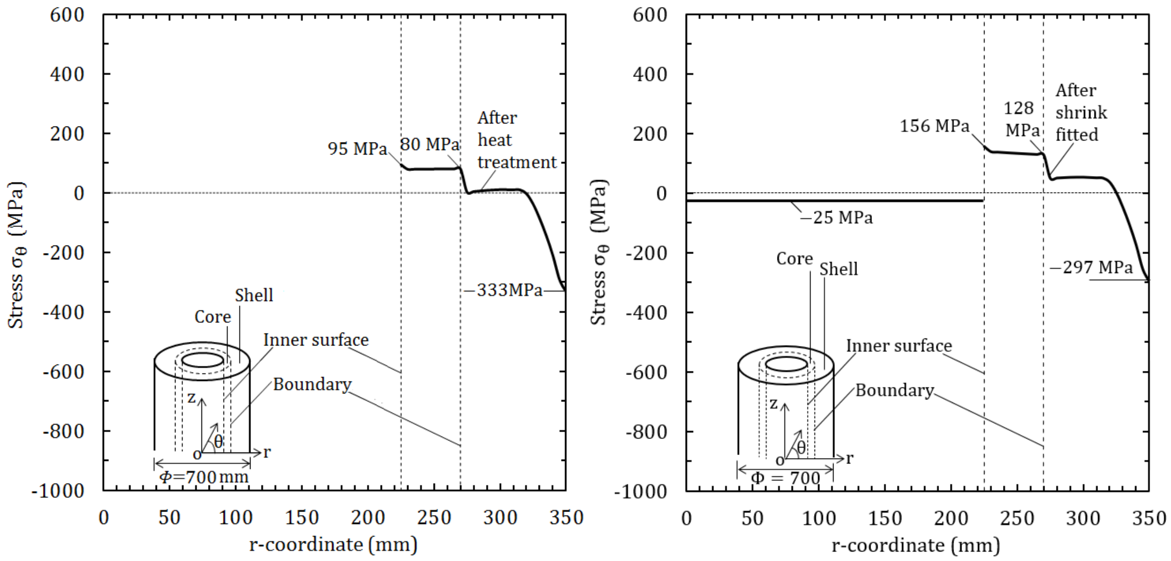

(a) Residual stress σ_θ distribution before shrink-fitting in Fig. 6-2(c2).

(b) Residual stress σ_θ distribution after shrink-fitting in Fig. 6-2(e).

Fig. 6-8 Residual stress σ_θ distribution obtained through sleeve heat treatment; (a) Residual stress σ_θ distribution at $z = 0$ before shrink-fitting, (b) Residual stress σ_θ distribution at $z = 0$ after shrink-fitting.

that is, the stress in heating process in Region I and the stress in quenching process in Region II and Region III. The temperature and the stress during the process in Region 1 to Region III can be explained in the following way.

In Region I: The temperatute is almost the same as the quenching temperature T_{Start} in whole sleeve with a small temperature difference maintained. The stress during pre-heating before quenching can be ignored.

In Region II: Due to quenching, the outer sleeve surface is cooled down from the temperature T_{Start}. Then, initially the tensile stress at the surface appears and increases due to the shrinkage of the outer layer, but this tensile stress immediately changes to the compressive stress. This is because the thermal shrinkage at the inner sleeve portion becomes larger than the thermal shrinkage at the outer sleeve surface and therefore the plastically elongated outer sleeve

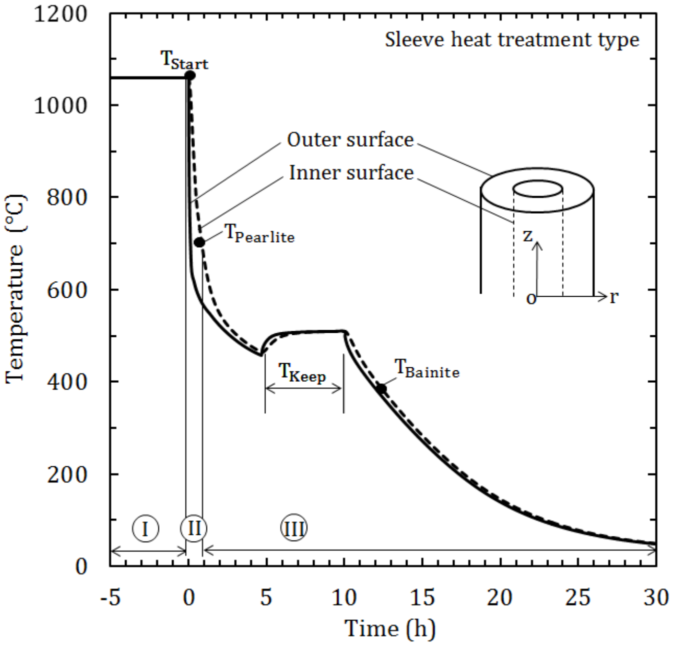

(a) Temperature at inner and outer surfaces provided along |z| ≤ 900mm in Fig. 6-2(c2)

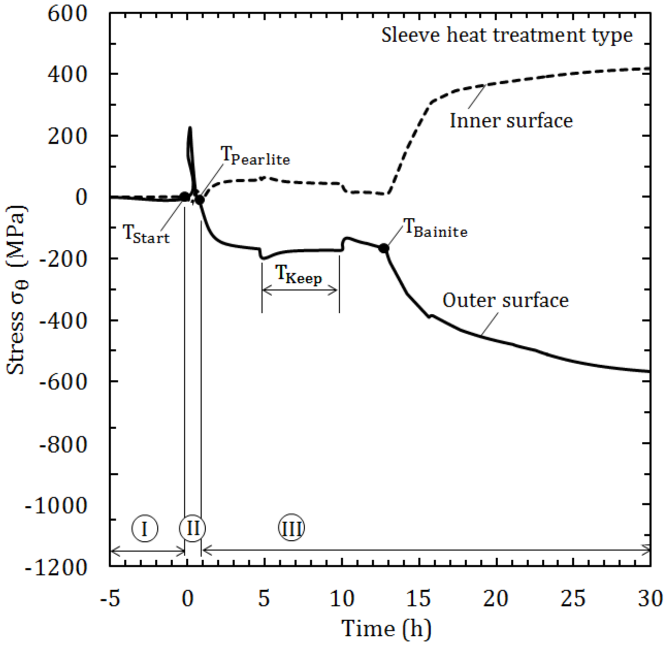

(b) Stress σ_θ at inner and outer surfaces when $z = 0$ in Fig. 6-2(c2)

Fig. 6-9 Temperature and σ_θ histories in sleeve heat treatment during quenching in Fig. 6-2(c2)

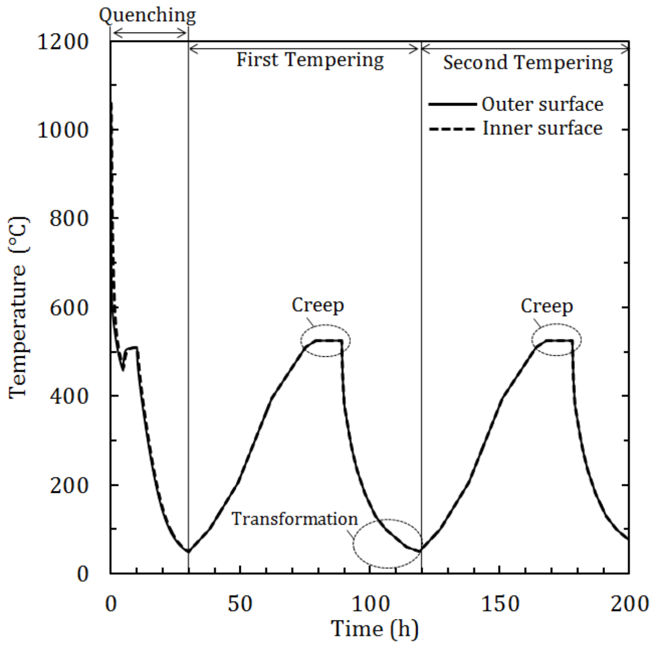

(a) Temperature at inner and outer surfaces provided along $|z| \leq 900$mm in Fig. 6-2(c2)

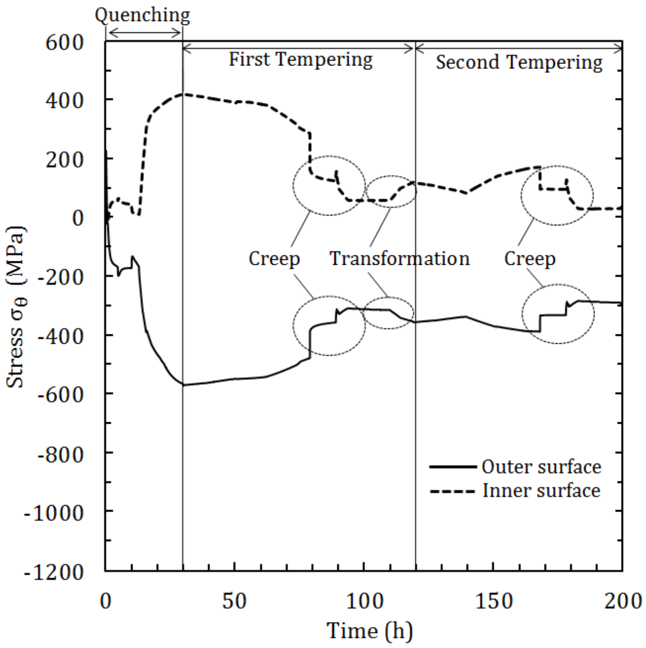

(b) Stress σ_θ at inner and outer surfaces in Fig. 6-2(c2).

Fig6-10 Temperature and σ_θ histories in sleeve heat treatment in Fig. 6-2(c2)

surface needs compression. Next, at temperature $T_{Pearlite}$, the pearlite expansion transformation appears at the inner layer, and during this process starting from the HSS/DCI boundary toward the inside surface, the compressive stress at the inner surface decreases until $T_{Pearlite}$ occurs. Then the stress at the inner surface center and the stres at the outer surface intersect.

In Region III: The residual stress of outer layer rapidly changes to the compression due to the pearlite transformation expansion at the inside sleeve portion. Then, the tensile stress at the center increases due to higher cooling rate. The stress at the inner layer becomes tensile, and the stress at the outer layer stress becomes compressive. When the temperature becomes T_{Keep}, the temperature is maintained by heating up the outer surface to adjust the initial excessive cooling. During this T_{Keep} keeping period, the compressive and tensile stresses increase slightly, and after that, the temperature difference disappears and the internal and external stresses decrease slightly. When the surface cooling starts again after T_{Keep} keeping, the bainite transformation expansion occurs in the outer layer at the temperature $T_{Bainite}$, and the compressive stress increases. The tensile stress at the inner surface also increases to balance the outer layer's compressive stress. In the cooling process after bainite transformation, the tensile stress increases due to the shrinkage at the inner layer, and to balance this the compressive stress at the outer layer increases. At the end of quenching, the residual stress at the inner surface becomes 418MPa.

6.4.2 Temperature and stress change during the tempering

Tempering treatment reduces the excessive residual stress due to quenching. Tempering also promotes martensitic transformation of retained austenite in microstructure. The previous studies indicated that the stress reduction due to tempering is mainly caused by the creep effect [17,25]. In this study, therefore, the time hardening law called power law, is used to express the creep behavior of the inner material DCI having lower strength under high temperature [14]. Eq. (6-1) is the creep constitutive equation of the inner layer DCI at the time t [19].

$$\varepsilon_c = A\sigma^m t^n \qquad (6\text{-}1)$$

The creep experimental was conducted under the constant stress σ=130MPa and σ =160MPa at T_{Keep}. Then, the constants A, m and n in Eq. (6-1) are determined and the following Eq. (6-2) is obtained [20-23].

$$\varepsilon_c = 8.43 \times 10^{-16} \sigma^{5.003} t^{0.4919} \qquad (2)$$

Fig. 6-10 shows the temperature history after tempering at the outer and inner surfaces in Fig. 6-2(c2) and the corresponding stress change σ_θ. As a result of twice tempering, the residual stress at the inner surface is significantly reduced to σ_θ = 94MPa, which is 22% of the stress at the end of quenching.

6.4.3 Stress reduction due to tempering expressed in terms of σ_θ and Mises stress σ_{eq}

The reason why the residual stress reduction is larger in the sleeve heat treatment will be discussed in comparison with the stress reduction in the solid heat treatment. Figs. 6-11(a) and 6-11(b) shows the residual stress distributions σ_θ in the sleeve heat treatment type in Fig. 6-2(c2) and in the solid heat treatment type in Fig. 6-2(b1). Here, the results are indicated at the beginning of the first tempering, at the beginning of the second tempering, and at the end of the second tempering. The sleeve roll result focuses on the stress at the inner surface r = 225mm, while the solid roll result focuses on the stress at the center r = 0 as a representative point of the inner layer. Then, the larger stress reduction effect in the first tempering process is discussed.

By comparing Fig. 6-11(a) and Fig. 6-11(b), the inner surface stress at the beginning of the tempering 418MPa in the sleeve heat treatment (Fig. 6-2(c2)) is

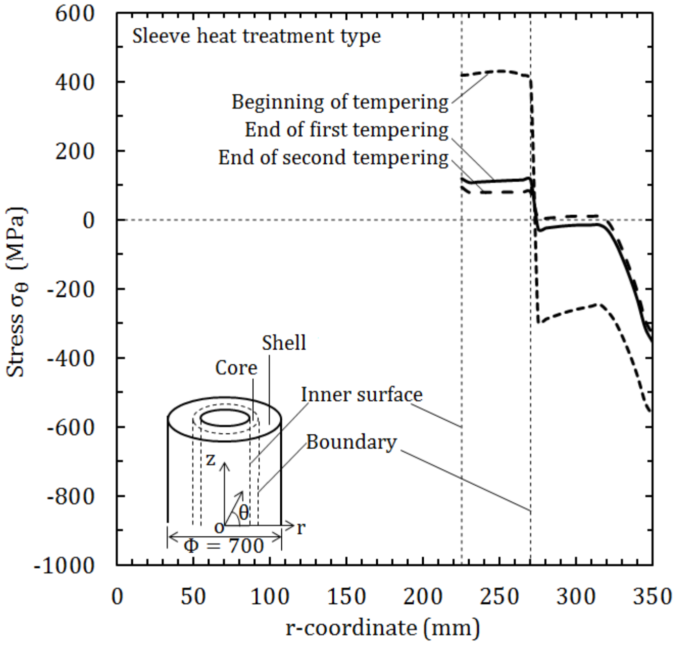

(a) Residual stress σ_θ at $z = 0$ in Fig. 6-2(c2)

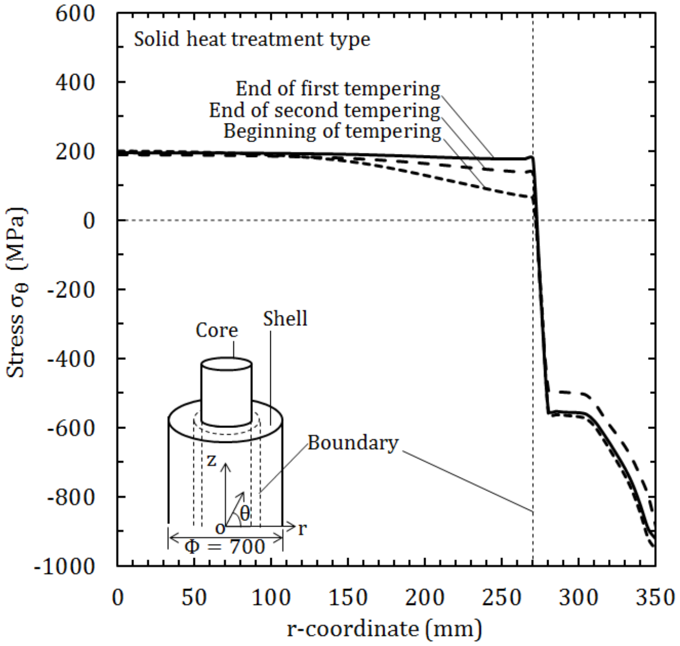

(b) Residual stress σ_θ at $z = 0$ in Fig. 6-2(b1)

Fig. 6-11 Comparison of stress distribution at z=0 between Fig. 6-2(c2) and Fig. 6-2(b1)

about twice larger than the stress in the solid heat treatment (Fig. 6-2(b1)). However, at the end of tempering, the sleeve heat treatment type (Fig. 6-2(c2))

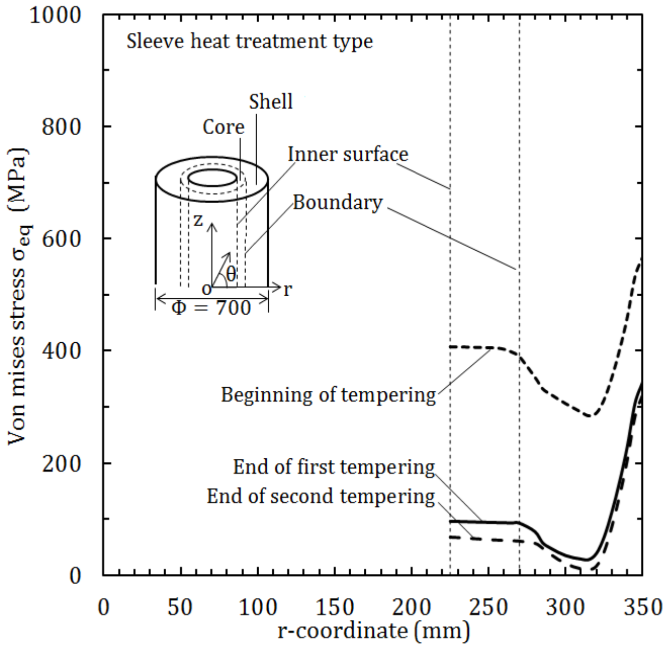

(a) Equivalent von Mises stress σ_{eq} at $z = 0$ in Fig. 6-2(c2)

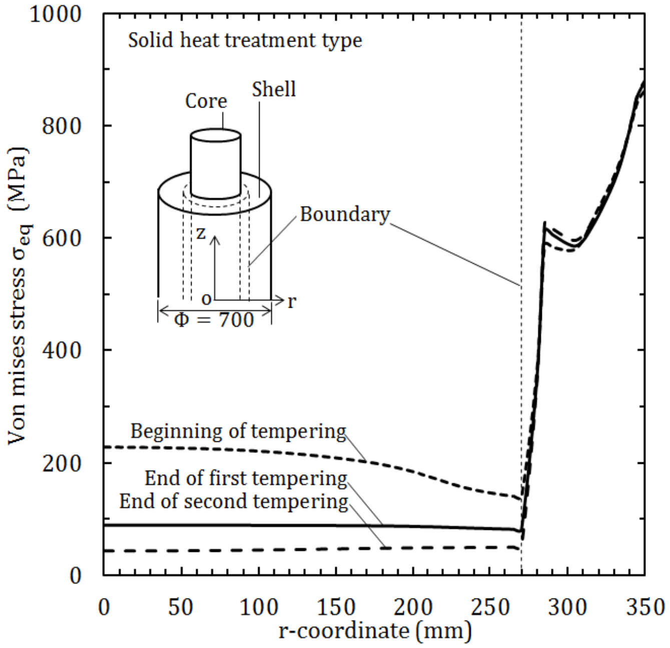

(b) Equivalent von Mises stress σ_{eq} at z=0 in Fig. 6-2(b1)

Fig. 6-12 Equivalent von Mises stress σ_{eq} at z=0 in Fig. 6-2(c2) and in Fig. 6-2(b1).

has a smaller residual stress at the inner surface.

As shown in Fig. 6-11(a), σ_θ at the inner surface (r=225 mm) of the sleeve roll is reduced by 71% after the first tempering process. However, σ_θ at the center (r = 0) of the solid roll (Fig. 6-11(b)) is reduced about 2% after the first tempering process. In this way, the sleeve heat treatment has a remarkable stress reduction at the inner surface residual stress σ_θ by the tempering process compared to the solid heat treatment type.

Next, the equivalent von Mises stress σ_{eq} is considered to discuss the stress reduction effect. Under multiaxial stress, the equivalent von Mises stress σ_{eq} can be regarded as the driving stress of creep deformation instead of the uniaxial stress σ in the creep constitutive Eq. (6-2) [23,24]. Here, the inner layer stress at r = 225 mm in the solid roll is compared with the inner surface stress at r = 225 mm in the the sleeve roll. In other words, the creep effect is discussed by substituting the equivalent von Mises stress σ_{eq} to the stress σ in Eq. (6-2).

Fig. 6-12(a) shows the residual distributions of von Mises stress σ_{eq} controlling the creep in the sleeve heat treatment after each heat treatment. Fig. 6-12(b) shows the results in the solid heat treatment type. From Fig. 6-12, the larger stress reduction of σ_{eq} is seen in the sleeve heat treatment compared to the solid heat treatment type. This is similar to the stress reduction of σ_θ in Fig. 6-11. The von Mises stress at the inner surface r = 225 mm in the sleeve roll at the initial stage of tempering σ_{eq} = 407MPa is more than twice larger than the one of the solid heat treatment σ_{eq} = 163MPa. This is because in the sleeve heat treatment the inner surface is stress free, while in the solid heat treatment type the stress state is triaxial.

6.5 Fatigue risk evaluation for bimetallic solid roll and bimetallic sleeve roll constructed by shrink-fitting

Table 6-2 and Table 6-3 show the maximum stress, minimum stress, mean stress, and stress amplitude at r=225mm and at r=270mm. The critical region r=225mm and 270mm are considered based on the previous roll failures experienced in industries [1], where the critical region for the bimetallic solid roll is near the HSS/DCI boundary (r=270mm in this study) and the critical region for the bimetallic sleeve roll is at the shrink-fitted region (r=225mm in this study). Also, previous studies explained the roll failure near the boundary HSS/DCI inside of the bimetallic solid roll is caused by the variation of σ_r during the roll rotation. And the slip failure at the shrink-fitted region inside of the bimetallic sleeve roll is caused by the variation of σ_θ. Therefore, the maximum and minimum values of σ_θ and σ_r at r=225mm and 270mm during a roll rotation can be the driving force causing the internal failure for both bimetallic solid roll and bimetallic sleeve roll.

In this section, although the standard rolling force ratio is $P/P_{total} = 1.0$, a more severe rolling force ratio $P/P_{total} = 1.5$ is considered to evaluate fatigue failure risk because the rolling trouble may cause such impact force due to the rolling plate biting and the temperature drop of the rolled material. In Table 6-2 and Table 6-3, the superscript “solid” represents the bimetallic solid roll while the superscript “sleeve” represents the bimetallic sleeve roll. Table 6-2 and Table 6-3 also show the mean stress $\sigma_m + \sigma_{res}$ which represents the superposing of the mean stress σ_m with the residual stress σ_{res}. Residual stress for the bimetallic

Table 6-2 Maximum stress, minimum stress, mean stress, stress amplitude at r=225 mm

Stress	σ_{max} (MPa)	σ_{min} (MPa)	σ_m (MPa)	σ_a (MPa)	$\sigma_m + \sigma_{res}$ (MPa)
σ_θ^{solid}	8	-56	-24	32	130
σ_r^{solid}	10	-299	-145	155	14
σ_θ^{sleeve}	91	-25	33	58	189
σ_r^{sleeve}	2	-140	-69	71	-94

solid roll is taken from the previous study [25]. Meanwhile, for the bimetallic sleeve roll, the residual stress is considered from the Fig. 6-8(b).

Table 6-3 Maximum stress, minimum stress, mean stress, stress amplitude at r=270 mm

Stress	$\sigma_{\max}$ (MPa)	$\sigma_{\min}$ (MPa)	σ_m (MPa)	σ_a (MPa)	$\sigma_m + \sigma_{res}$ (MPa)
σ_θ^{solid}	9	-133	-62	71	74
σ_r^{solid}	7	-453	-223	230	-77
σ_θ^{sleeve}	105	-9	48	57	176
σ_r^{sleeve}	-1	-167	-84	83	-96

Since the mean stress in Table 6-2 and Table 6-3 for the bimetallic solid roll are large compressive stress, the fatigue limit lines should be newly prescribed under large compressive stress since no study is available. Fatigue failure under large compressive stress was treated by several previous papers but usually, they considered rolling contact fatigue in ball/roller bearings and backup roll surface spalling [26,27]. Only few data are available for ordinary fatigue strength under large compressive stress fields [28]. Fig. 6-13 shows a stress amplitude versus mean stress diagram (σ_a-σ_m diagram) to discuss the fatigue limit for the stresses in Table 6-2 and Table 6-3. The thick solid lines passing through points A, D, F, G, H in Fig. 6-13 determines the fatigue limit line. Details of this fatigue limit line A, D, F, G, H is included in Appendix A.3 [29].

Fig. 6-13(a) shows the fatigue limit diagram at r=225mm and Fig. 6-13(b) shows the fatigue limit diagram at r=270mm. Fig. 6-13(a) and Fig. 6-13(b) show the change of the mean stress σ_m after superposing the residual stress σ_{res}. All stresses move closer to the fatigue limit line due to the tensile residual stress except σ_r^{sleeve} for the bimetallic sleeve roll due to the compressive residual stress.

Table 6-4 Safety factor defined as $\mathrm{SF} = \overline{\mathrm{OB}'}/\overline{\mathrm{OB}}$ to evaluate the stresses in Fig. 6-13

At r=225 mm		At r=270 mm	
Stress	Safety factor	Stress	Safety factor
$\sigma_\theta^{\mathrm{solid}}$	1.98	$\sigma_\theta^{\mathrm{solid}}$	1.65
$\sigma_r^{\mathrm{solid}}$	1.03	$\sigma_r^{\mathrm{solid}}$	0.94
$\sigma_\theta^{\mathrm{sleeve}}$	1.24	$\sigma_\theta^{\mathrm{sleeve}}$	1.30
$\sigma_r^{\mathrm{sleeve}}$	4.41	$\sigma_r^{\mathrm{sleeve}}$	4.32

Table 6-4 shows the safety factor evaluation for the stresses in Fig. 6-13. The safety factor is defined as $\mathrm{SF} = \overline{\mathrm{OB}'}/\overline{\mathrm{OB}}$ where O is the origin point, B is the stress point, and B' is the intersection point of line OB to the fatigue limit line (see Fig. A.4.1(a)). A larger SF value means the point is relatively safer than another point having a smaller SF value. Therefore, the relative safety factor SF can be used to compare the risk of fatigue failure. At r=270 mm, the most dangerous stress for the bimetallic solid roll can be found as $\sigma_r^{\mathrm{solid}}$ with SF=0.94 and the most dangerous stress for the bimetallic sleeve roll can be found as $\sigma_\theta^{\mathrm{sleeve}}$ with SF=1.30. Similar results are obtained at r=225mm as can be expressed as $\sigma_r^{\mathrm{solid}}$ with SF=1.03 and $\sigma_\theta^{\mathrm{sleeve}}$ with SF=1.24. It is found that the stress appearing at the inside of the bimetallic sleeve roll is safer than the stress appearing at the solid bimetallic roll although the damage and defects when the slippage occur are not taken into consideration yet in this analysis.

6.6 Conclusion

The sleeve rolls are successfully used as the backup rolls with a diameter exceeding 1000mm and the large rolls for H-shaped steel rolling. Although the sleeve rolls have some peculiar problems, they have some advantages such as that the shaft can be reused. In this paper, therefore, the residual stress of the sleeve roll was considered by comparing two manufacturing methods; one is turning inside of the solid roll after heat treatment and the other is heat treatment after

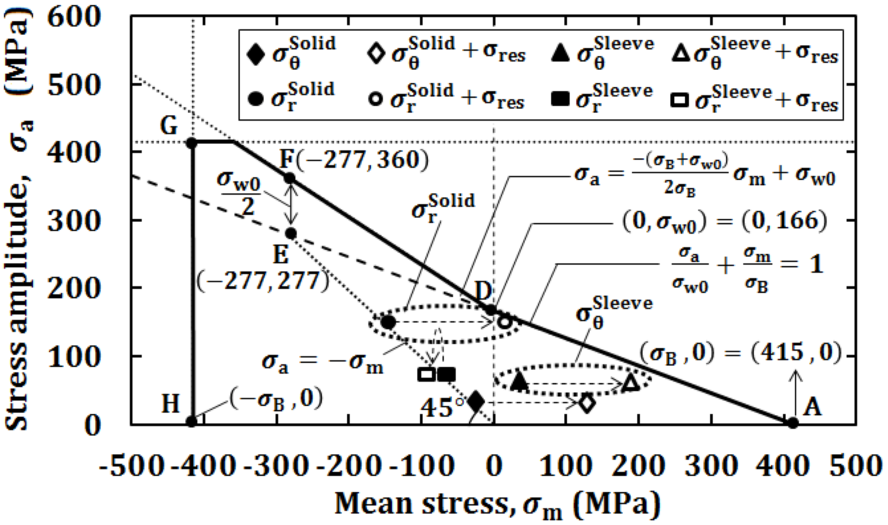

(a) Fatigue limit diagram evaluation at r=225 mm

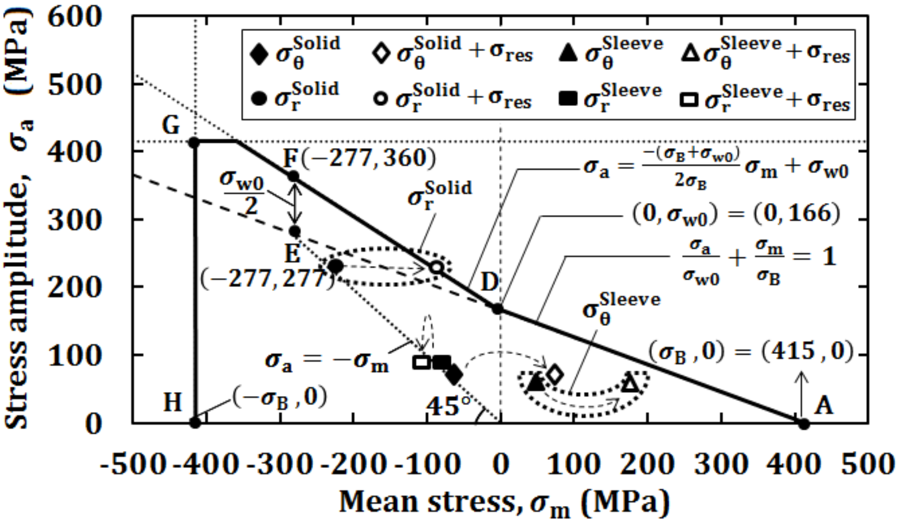

(b) Fatigue limit diagram evaluation at r=270 mm

Fig. 6-13 Fatigue limit diagram at r=225 mm and r=270 mm

turning inside of the solid roll. After a suitable manufacturing method is found, the fatigue risk of the sleeve was discussed on the basis of the residual stress and rolling stress by comparing the sleeve bimetalic roll and the solid bimetalic roll. The conclusions can be summarized as follows.

1. The tensile residual stress at the inner surface of the sleeve heat treatment (Fig. 6-2(c2)) is much smaller than the tensile residual stress at the inner layer of the solid heat treatment (see Fig. 6-2(b2)). It may be concluded that the sleeve heat treatment is suitable for manufacturing the sleeve roll since the inner layer of the fracture hardly occurs (see Fig. 6-7, Fig. 6-8).
2. The tensile residual stress of the sleeve heat treatment can be reduced significantly by the tempering. This is because the inner surface is free of stress in the sleeve heat treatment although the center of the solid heat treatment has triaxiality of stress (see Fig. 6-12).
3. The fatigue failure risk was investigated by using the fatigue limit diagram with the safety factor SF (see Fig. 6-13). At r=270 mm, the most dangerous stress for the bimetallic solid roll appears as σ_r^{solid} whose relative safety factor SF=0.94. On the other hand, and the most dangerous stress for the bimetallic sleeve roll is σ_θ^{sleeve} whose relative safety factor SF=1.30. Similar results are obtained at r=225 mm as σ_r^{solid} with SF=1.03 and σ_θ^{sleeve} with SF=1.24. It may be concluded that the stress at the inside of the bimetallic sleeve roll is safer than the solid bimetallic roll although the damage and the defect appearing at the slipped surface have to be considered in the future studies.

References for Chapter 6

[1] Y. Sano, in *The 245th JSMS Committee on Fatigue of Materials and The 36th JSMS Committee on Strength Design・Safety Evaluation,* The Society of Materials Science Japan, Kyoto, Japan 1999, 40.
[2] T. Koizumi, K. Edamatsu, *Tetsu-to-Hagane* 1981, *67*, 12.
[3] K. Sakebe, *Japan Steel Works Technical Report* 1969, *26*, 3044.
[4] N.A. Noda, H. Sakai, Y. Sano, Y. Takase, Y. Shimoda, Metals 2018, 8, 998.
[5] K. Sakai, Tetsu-to-Hagane 1974, 60, 1591.
[6] T. Inoue, K. Haraguchi, S. Kimura, J. Soc. Mater., Sci. Jpn. 1976, 25, 521.

[7] R. Isomura, Tetsu-to-Hagane 1961, 47, 936.
[8] K. Arimoto, Ph.D. thesis, Kyoto University, 2007,
[9] N.A. Noda, Y. Sano, X. Wang, Y. Nakagawa, W.H. Guan, K. Ono, K. Hu, Trans.of Society of Automotive Engineers of Japan 2015, 46, 831.
[10] H. Sakai, N.A. Noda, Y. Sano, G. Zhang, Y. Takase, Tetsu-to-Hagane 2019, 105, 1126.
[11] H. Sakai, N.A. Noda, Y. Sano, G. Zhang, Y. Takase, ISIJ Int. 2019, 59, 889.
[12] N.A. Noda, R.A. Rafar, H. Sakai, X. Zheng, H. Tsurumaru, Y. Sano, Y. Takase, Eng. Fail. Anal. 2021, 126, 105465.
[13] N.A. Noda, R.A. Rafar, Y. Sano, International Journal of Modern Physics B 2021, 2140020.
[14] N.A. Noda，K. Hu，Y. Sano, K. Ono, Y. Hosokawa, Steel Res. Int. 2016, 87, 1478.
[15] N. A. Noda，K. Hu，Y. Sano, K. Ono, Y. Hosokawa, Steel Res. Int. 2017, 88, 1600165.
[16] N.A. Noda, Y. Sano, M.R. Aridi, K. Tsuboi, N. Oda, Metals 2018, 8, 952.
[17] N.A. Noda, M.R. Aridi, R. Torigoe, K. Tsuboi, Y. Sano, J. Jpn. Soc. Technol. Plasticity 2020, 61 , 183.
[18] Y. Sano, J. Jpn Soc. Technol. Plasticity 1998, 39, 2.
[19] D.L. May, A.P. Gordon, D. S. Segletes, in Turbo Expo: Power for Land, Sea, and Air, vol. 55263, p. V07AT26A005. American Society of Mechanical Engineers, 2013.
[20] WO2013042528 A1: 2012, Centrifugal casted composite roller for hot rolling and method for producing same.
[21] Z. Tanaka, T. Obata, Journal of Japan Welding Society 1967, 36, 222.
[22] M. Miyakawa, Creep deformation theory and design, Nikkan Kogyo Shimbun. Ltd, Tokyo, Japan 1963.
[23] Marc Mentat team:Theory and User Information. Vol. A, MSC. Software, Tokyo, 2012.
[24] R. Ohtani, Japan Society of Material Science 1969， 18， 824.
[25] N.A. Noda, M.R. Aridi, Y. Sano, International Journal of Modern Physics B 2021, 35, 2140044.
[26] T. Sakai, B. Lian, M. Takeda, K. Shiozawa, N. Oguma, Y. Ochi, M. Nakajima, T. Nakamura, Int. J. Fatigue 2010, 32, 497.
[27] E. Zalnezhad, A.A.D. Sarhan, P. Jahanshahi, Int. J. Adv. Manuf. Technol. 2014, 70, 2211.
[28] K.H. Schroder. A Basic Understanding of the Mechanics of Rolling Mill Rolls. Eisenwerk Sulzau-Werfen, ESW-Handbook, Tenneck, Austria 2003.
[29] M.R. Aridi, N.A. Noda, Y. Sano, K. Takata, S. Zifeng. Fatigue failure analysis for bimetallic work roll in hot strip mills. Steel Research International 2021, (Accepted) 10.1002/srin.202100313.
[30] A.A. Garcia-Granada, D.J. Smith, M.J. Pavier, Int. Journal Mech. Sci. 2000, 42, 1027.
[31] K. Kamimiyada, Y. Konno, A. Yanagitsuru, Mater. Trans. 2020, 61, 1987.
[32] A. Ince, G. Glinka, Fatigue Fract. Engng. Mater. Struct. 2011, 34, 854.
[33] K. Kasaba, T. Sano, S. Kudo, T. Shoji, K. Katagiri, T. Sato, J. Nucl. Mater 1998, 258-263, 2059.
[34] H. Nishitani, N. Yamashita, Trans. of the JSME 1966, 32, 1456.
[35] H. Nisitani, M. Goto, Trans. of the JSME 1984, 50, 1926.
[36] Y. Akiniwa, K. Tanaka, N. Taniguchi, Trans. of the JSME 1987, 53, 1768.

7 Main conclusion

In this paper, the mechanism of interfacial slip in a sleeve assembly type roll constructed by shrink-fitting is verified by FEM analysis, and to apply it to the actual machine, the roll material, the fitting conditions, and the effect of the rolling load is considered. Finally, the experimental method of a miniature roll is demonstrated to verify the analysis. Then, the fatigue failure risk is discussed focusing on several critical points on the actual roll by assuming similar defects in an experimental roll. The following conclusions based on each chapter can be summarized as follow.

Chapter 1 provided a brief introduction of the bimetallic work roll and the problems encountered in the sleeve assembly type rolls. Although the shrink-fitting sleeve assembly roll has many advantages compared to the solid roll, it also has unique problems such as residual bending and sleeve slip. Therefore, this study was focused on clarification of the sleeve slip in the bimetallic work roll.

In Chapter 2, the mechanism of the sleeve slip formation under free rolling for the hot rolling roll was considered. In addition, in this chapter, to get closer to the actual rolling conditions, the effect of elastic deformation of the shaft on the interfacial slip was investigated under the free rolling state with reference to the previous study which the shaft is a rigid body. Furthermore, in addition to the steel shaft, other shaft materials were considered to clarify the effect of elastic deformation of the shaft material on the interfacial slip. The irreversible relative displacement was focused, which is corresponding to the interfacial slip in ball bearing. The conclusions can be summarized as follows:

1. The accumulation of the irreversible relative displacement $u_{\theta,ave.}^{P(0)\sim P(2\pi)}$ due to the rotation force can be regarded as the slip per rotation since the order of the experiment agrees with the simulation results.
2. The interfacial displacement is promoted by the roll deformation since $u_{\theta,ave.}^{P(0)\sim P(\varphi)}$ increases with decreasing the shaft Young's modulus E_{shaft} as shown in Fig. 2-5. The effect of E_{shaft} on the irreversible relative displacement is related to the interface slippage region size ℓ_{slip} as shown in Fig. 2-7.
3. The interface slippage region ℓ_{slip} can be explained from the smaller contact stress region ℓ_{small} as shown in Fig. 2-9.

In Chapter 3, the effect of rolling torque on the interfacial slip was considered for hot rolling rolls. In addition, the effects of the shrink-fitting ratio and the friction coefficient which are the parameters of the resistance torque are also considered since they may contribute to slippage resistance. Here, the interface slip and the displacement increase rate were analyzed. The discussion on the interfacial slip and the displacement increasing rate are summarized as follows:

1. Under the conditions of $T=T_m\sim3T_m$ and $P=P_0\sim3P_0$, the effect on the displacement increasing rate is larger, and the slip increases as the load condition increases.
2. When the shrink fit rate δ/d increases, the displacement increase rate $du_{\theta}^{P(0)\sim P(2\pi)}(\theta,\varphi)/d\varphi$ decreases significantly because of the increase of the slip resistance torque on the shrink fit surface (see Fig. 3-7).
3. With increasing the friction coefficient μ, the displacement increase rate $du_{\theta}^{P(0)\sim P(2\pi)}(\theta,\varphi)/d\varphi$ decreases exponentially (see Fig. 3-8).

In Chapter 4, the interfacial slip in shrink-fitted roll was confirmed experimentally under free rolling conditions by using a miniature roll. The behavior of the sleeve slip obtained in the experiment was considered and compared with the numerical analysis results. In addition, the effect of the sleeve inner surface defects due to the interfacial slip on the sleeve strength is considered. In this chapter, the fatigue risk in terms of the stress concentration factor, Kt of the defect is evaluated. The following conclusions are obtained.

1. The numerical analysis values for both rolls A and B are 3.6~4.3 times the experimental values, and the orders are almost the same, confirming the usefulness of the numerical simulation.
2. The slip defects caused by the interfacial slip begin with scratch wear on the top of the finishing process. Under the influence of erosive wear and adhesive wear, the width and size of scratch wear increase, and eventually, large adhesion lumps are generated. Then it stops as an ellipsoidal defect.
3. The characteristics of each defect region was described and the defect formation was clarified.
4. For roll B (shrink-fit ratio $\delta/d=0.21\times10^{-3}$), the slip amount (32.3 mm) obtained from the movement of the marking line of the roll used in the experiment is the length of the defect on the sleeve and shaft. It is almost the same as the sum of (defect ②: 33.2 mm, defect ④: 32.7 mm). Thus the starting point and end point of the scratch can accurately evaluate the actual condition of slip.
5. The fatigue limit for the actual roll was evaluated by considering the stress concentration coefficient of an ellipsoidal defect, Kt≅1.14. The point was situated inside the fatigue endurance line and it is on the safe side regardless of the impact force conditions and the stress concentration of the defect.

Chapter 5 was focused on the high-speed steel bimetallic sleeve rolls, which are made by shrink-fitting the composite sleeve and shaft. In this study, in addition to the residual stress, the stress concentration on the inner surface of the sleeve caused by the interfacial slip under the actual rolling conditions and the defects caused by the slip were considered for the sleeve assembly type composite roll. Then, the effect on safety against sleeve cracking due to fatigue was evaluated by considering the root area $\sqrt{area}$ of the defect. The conclusions are as follows:

1. The maximum stress $\sigma_{\theta max}$, minimum stress $\sigma_{\theta min}$, and stress amplitude $\sigma_{\theta a}$ at the interface where slip occurs with roll rotation is clarified (see Fig. 5-7). These act as fluctuating stresses.
2. Under the conditions $P = 1.5P_0, T = 1.5T_m$, which take into account the impact force, the stress amplitude σ_a is about twice of the standard conditions $P = P_0, T = T_m$.
3. The safety of the bimetallic sleeve assembly type roll (real roll) is evaluated with reference to the defect dimensions due to slippage observed in the miniature roll and the hot rough rolling roll.

In Chapter 6, the difference of the residual stress generated between the bimetallic solid roll and the current study of bimetallic sleeve roll constructed by shrink-fitting was studied. After shrink-fitting of the shaft, the residual stress was compared with one of the solid rolls. The conclusions are as follows:

1. The tensile residual stress at the inner surface of the sleeve heat treatment (Fig. 6-2(c2)) is much smaller than the tensile residual stress at the inner layer of the solid heat treatment (see Fig. 6-2(b2)). It may be concluded that the sleeve heat treatment is suitable for manufacturing the sleeve roll since the inner layer of the fracture hardly occurs (see Fig. 6-7, Fig. 6-8).
2. The tensile residual stress of the sleeve heat treatment can be reduced significantly by the tempering.

3. The fatigue failure risk was investigated by using the fatigue limit diagram with the safety factor SF (see Fig. 6-13). It may be concluded that the stress at the inside of the bimetallic sleeve roll is safer than the solid bimetallic roll.

Acknowledgement

Alhamdulillah. A very special thanks to my beloved family for their love, support, understanding and encouragements.

I would like to thank my supervisor, Professor Nao-Aki Noda for giving me the opportunity to study under his supervision and also for his valuable guidance and advice throughout my study. I highly appreciated his advice, assistance and commitment which help me to prepare and complete my Ph.D. study.

Also, I would like to appreciate Dr. Yoshikazu Sano, my project advisor for his great advice. I would also like to thanks the laboratory technical staff, Dr. Yasushi Takase, for his help and advice concerning the simulations and the mathematical computations, and also facilitating in experiment.

Many thanks to the contributions and insightful observations of my committee members, Prof. Yasuhiro Akahoshi, Prof. Kenji Matsuda, Prof. Toshihiko Umekage, and Prof. Hiroshi Yamada.

Particular thanks to Dr. Radzi, Dr. Hiromasa Sakai, Dr. Rei Takaki, Hiroyuki Tsurumaru and Yudai Taruya for their valuable discussions, support and friendship. Thank you to all lab members of Elasticity and Fracture Laboratory, and all those who have helped me carry out my work.

To all my friends and others who in one way or another shared their support either morally or emotionally, thank you. And also thanks for all the wonderful memories. “Good times come and go, but the memories will last forever”.

Also, special thanks to Keiko Matsuoka Sensei for her help throughout my stay in Japan.

Many thanks to the technical staff of the postgraduate and student office including the Departments of Mechanical Engineering, Kyushu Institute of Technology for their support throughout my years of study in Japan.

Lastly, my thanks and appreciations also go to the Ministry of Education, Culture, Sports, Science and Technology of Japan (MEXT) for the Monbukagakusho scholarship, which made it possible for my study and stays in Japan.

A Appendix

A.1 Interfacial displacement $\boldsymbol{u_\theta^{P(0)\sim P(\varphi)}(\theta)}$ and average interfacial displacement $\boldsymbol{u_{\theta,ave.}^{P(0)\sim P(\varphi)}(\theta)}$

Fig. A-1 illustrates two-dimensional modeling where the roll rotation is expressed by the load shifting on the fixed roll surface [12-15]. The roll is assumed to be subjected to the concentrated rolling load P = 13270 N/mm [4, 5]. As shown in Fig. A-1, the continuous roll rotation can be expressed by the discrete load shifting with a constant interval φ_0. The most suitable value of φ_0 can be chosen to reduce the computational time without loosening the accuracy. From the comparison among the results $\varphi_0 = 0.25°\sim12°$, the load shift angle $\varphi_0 =$ 4° is adopted in the following discussion since the relative error between $\varphi_0 =$ 0.25° and $\varphi_0 = 4°$ is less than a few percent. In the following, both forces are denoted by P.

Fig. A-2 shows the variation of $u_\theta^{P(0)}(\theta)$ due to the initial load $P(0)$ by comparing the elastic and rigid shaft. As shown in Fig. A-2(a), the displacement is symmetric with respect to $\theta = 0$ as can be expressed in the following equation:

$$-u_\theta^{P(0)}(-\theta) = u_\theta^{P(0)}(\theta) \qquad (\mathrm{A}-1)$$

Fig. A-2(b) shows the displacement $u_\theta^{P(0)\sim P(\pi)}(\theta)$ for the elastic shaft due to the load shifting $P(0)\sim P(\pi)$ and the displacement $u_\theta^{P(0)\sim P(2\pi)}(\theta)$ due to the load shifting $P(0)\sim P(2\pi)$ in comparison with $u_\theta^{P(0)}(\theta)$. As shown in Fig. A-2(b), $u_\theta^{P(0)\sim P(\pi)}(\theta)$ and $u_\theta^{P(0)\sim P(2\pi)}(\theta)$ are not symmetric anymore with respect to $\theta = 0$ due to the load shifting as given in the following equation:

$$-u_\theta^{P(0)\sim P(2\pi)}(-\theta) \neq u_\theta^{P(0)\sim P(2\pi)}(\theta) \qquad (\mathrm{A}-2)$$

In Figs. A-2(a) and A-2(b), the average values of the displacements are also indicated by $u_{\theta,ave.}^{P(0)}$ and $u_{\theta,ave.}^{P(0)\sim P(\varphi)}$. Since those displacement varies depending on

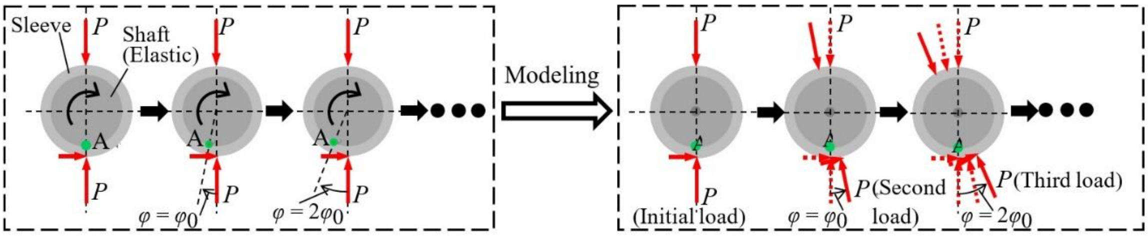

(a) Rotation of the real roll. (b) Rotation of the loads in the FEM model.

Fig. A-1 The roll rotation can be replaced by discrete load shifting by the angle φ_0 on the fixed roll.

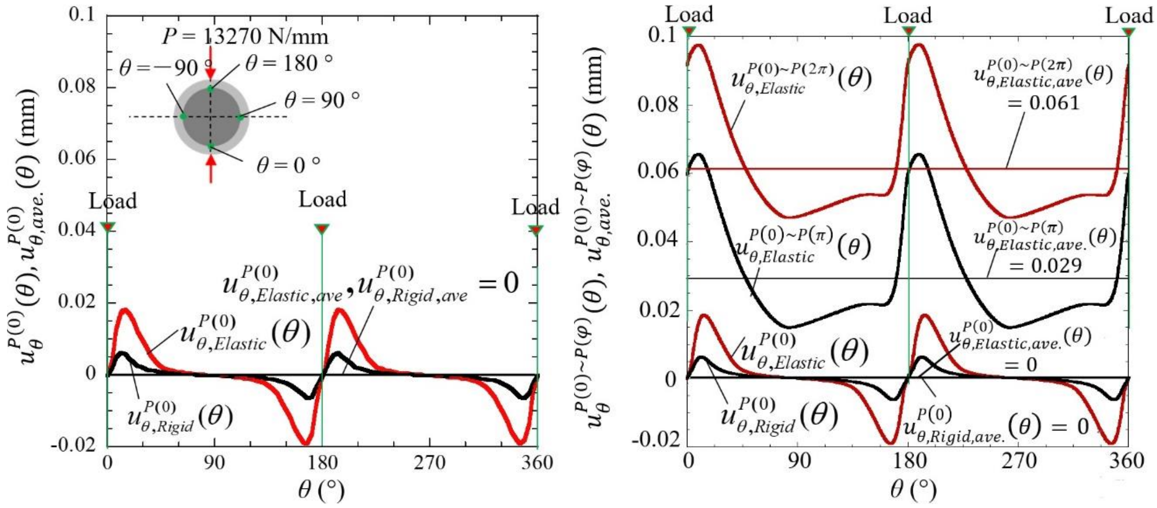

(a) Displacement $u_\theta^{P(0)}(\theta)$ due to the initial loading $P(0)$.

(a) Displacement $u_\theta^{P(0)\sim P(\varphi)}(\theta)$ due to loading shift $P(0)\sim P(\pi)$ and $P(0)\sim P(2\pi)$.

Fig. A-2 Variations of the interfacial displacement.

θ, the average displacement can be defined as follows:

$$u_{\theta,ave.}^{P(0)\sim P(\varphi)} = \frac{1}{2\pi}\int_0^{2\pi} u_\theta^{P(0)\sim P(\varphi)}(\theta)d\theta \qquad (\mathrm{A}-3)$$

When the initial load P is applied at $\varphi = 0$, the average displacement is zero as $u_{\theta,ave.}^{P(0)} = 0$ and $u_\theta^{P(0)}(\theta)$ is symmetric. Due to the load shifting from $\varphi = 0$ to $\varphi = \varphi$, the average displacement $u_{\theta,ave.}^{P(0)\sim P(\varphi)}$ increases losing the symmetry. This is because $u_\theta^{P(0)}(\theta)$ is irreversible as shown in Fig. 2-3.

A.2 Residual stress simulation of the bimetallic solid roll

In this paper, as shown in Fig. 6-11(b), the residual stress distributions are obtained by using the quenching and tempering simulation method in the previous paper [14-17]. In roll companies, the surface residual stress of the roll is always confirmed after tempering the roll by using the non-destructive inspections such as X-ray diffraction method and ultrasonic method. The authors' previous simulation may provide the residual stress distribution from the surface to the inside of the roll under various different heat treatments. Since the internal stress cannot be obtained by using these non-destructive method, the destructive inspections such as Sachs boring method and disk cut method were sometimes applied spending high cost and time-consuming effort [30,31]. In this sense, the residual stress simulation has been requested to obtain the residual stress distribution from the surface to the inside of the roll under various different heat treatments.

Fig. A-3 illustrates the surface temperature history of the bimetallic solid roll (see Fig. 6-2(b1)) during heat treatment consisting of the pre-heating,

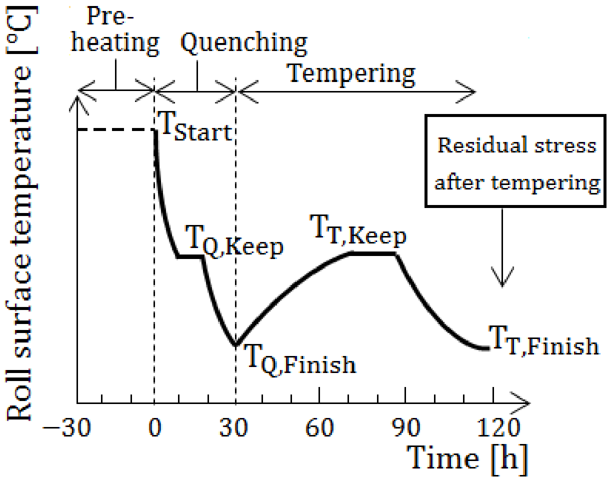

Fig. A-3 Heating, quenching, and tempering treatment of the bimetallic work roll

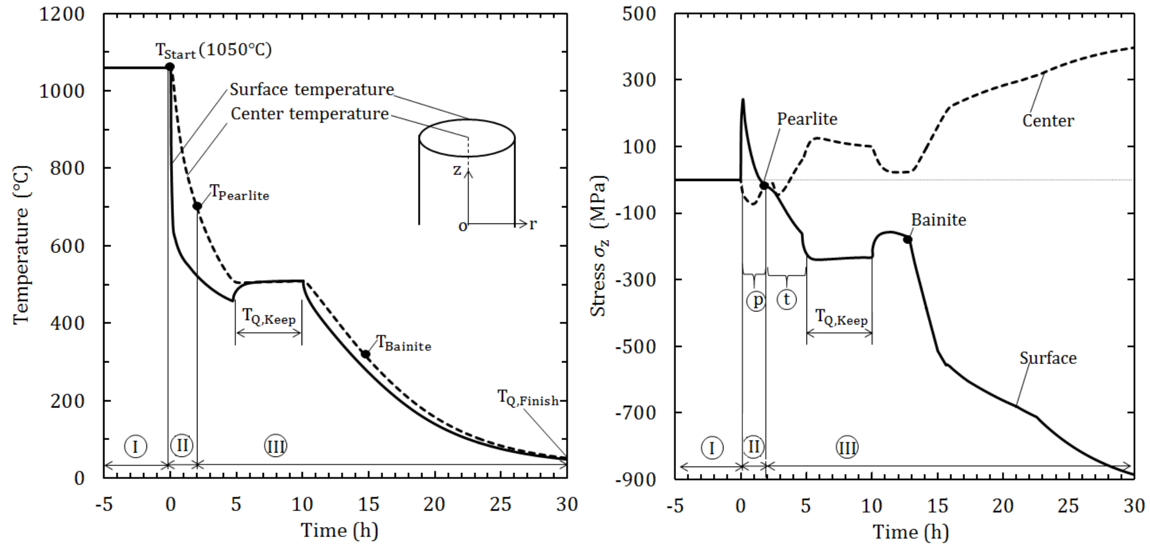

(a) (b)

Fig. A-4 (a) Temperature at inner and outer surfaces provided along $|z| \leq 900$mm in Fig. 6-2(b1); (b) Stress σ_r at inner and outer surfaces when $z = 0$ in Fig. 6-2(b1).

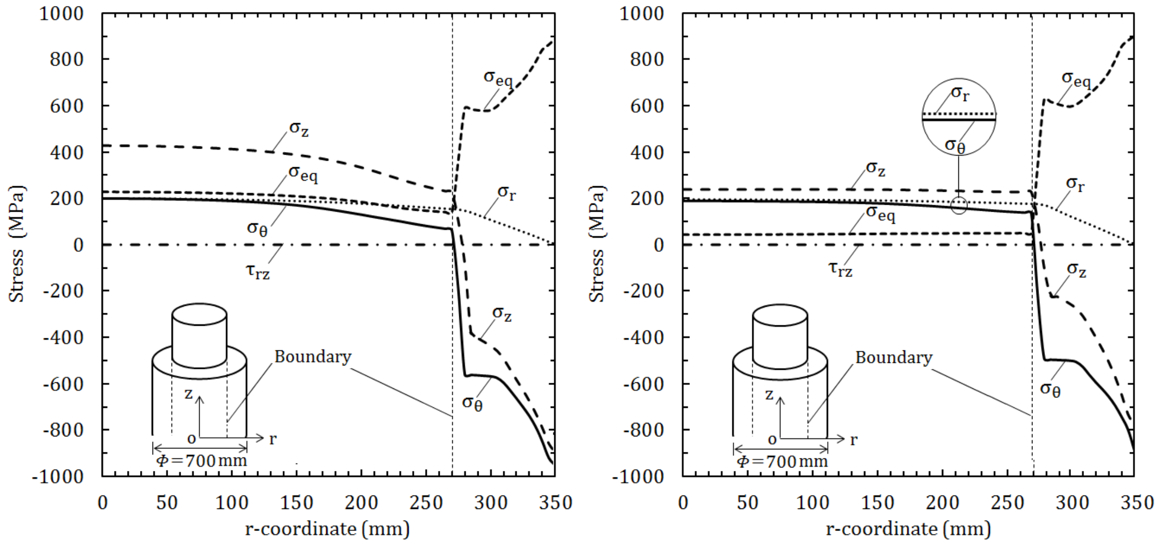

(a) (b)

Fig. A-5 Residual stress distributions at z=0 in Fig. 6-2(b1) for all stress components. (a) At the beginning of tempering and (b) At the end of second tempering (see Fig. 6-2(b1)) quenching, and tempering. In pre-heating process, the whole roll is heated up to the uniform temperature of $T_{Start} = 1050°C$ and kept for several hours. Then, the roll temperature drops rapidly through air cooling. After that, the roll is put into the furnace again and maintained at $T_{Q,Keep}$ to prevent excessive thermal stresses caused by rapid cooling. After keeping period, the roll is cooled down slowly until to the temperature of $T_{T,Finish}$. After the quenching process, the tempering process will be performed 2 times to release the residual stress and obtained the stable microstructure.

Fig. A-4 shows the histories of (a) temperature and (b) stress σ_z for the bimetallic solid roll during quenching process. The temperature and the stress in Region 1 to Region III have beed explained in the Section 6.4.1 in this paper.

Fig. A-5(a) and Fig. A-5(b) shows the obtained stress distributions σ_θ, σ_z, σ_r,τ_{rz}, σ_{eq} at z=0. Fig. A-5(a) shows the ones before the first tempering and Fig. A-5(b) shows the ones after the second tempering. From these figures, it is seen that tempering does not affect σ_r, τ_{rz} very much. Instead, tempering reduces σ_z largely at both inner and outer layers. And tempering reduces σ_θ only at the outer layer.

A.3 Fatigue limit line under large compressive stress

In the previous study [29], the fatigue limit lines are newly prescribed under large compressive stress since no study is available. Fig. A-6 shows a stress amplitude versus mean stress diagram (σ_a-σ_m diagram) to discuss the fatigue limit under large compressive alternative loading $\sigma_m \leq 0$. First of all, assume the ultimate tensile strength σ_B can be applied to the compressive stress $\sigma_m < 0$ and alternative stress $\sigma_a > 0$ as express in Eq. (A-4).

$$|\sigma_m| < \sigma_B, \ |\sigma_a| < \sigma_B \tag{A-4}$$

The so-called modified Goodman law can be expressed in Eq. (A-5) for $\sigma_m \geq 0$.

$$\frac{\sigma_a}{\sigma_{w0}} + \frac{\sigma_m}{\sigma_B} \leq 1 \tag{A-5}$$

Assume this limit line $\sigma_a/\sigma_{w0} + \sigma_m/\sigma_B = 1$ can be extended to the negative region $\sigma_m < 0$ [32]. Consider pulsating compressive loading $\sigma_a + \sigma_m = \sigma_{max} = 0$ as illustrated in Fig. A-6(c). In Fig. A-6(a), the line is indicated as $\sigma_m = -\sigma_a$ denoted by a dotted line with an angle of $45°$ from the ordinate from the origin. In the region described by Eq. (A-6), the crack does not propagate and no final failure happens.

$$\sigma_a + \sigma_m = \sigma_{max} \leq 0 \tag{A-6}$$

Denote the intersection $\sigma_a/\sigma_{w0} + \sigma_m/\sigma_B = 1$ and $\sigma_a + \sigma_m = 0$ as point E as shown in Fig. A-6(a). Since point E satisfies Eq. (A-6), there is no final failure. Therefore, by adding a certain amount of positive tensile stress, point F and point F' are newly considered [33]. Regarding the fully reversed loading, the fatigue limit is known as point D as shown in Fig. A-6(b). Point D can be the fatigue limit under the maximum tensile stress $\sigma_{max} = \sigma_m + \sigma_a = 166\,\mathrm{MPa}$ and the maximum compressive stress $\sigma_{min} = \sigma_m - \sigma_a = -166\,\mathrm{MPa}$. Instead, at point E, as shown in Fig. A-6(c), the maximum tensile stress $\sigma_{max} = \sigma_m + \sigma_a = 0$ but the maximum compressive stress $\sigma_{min} = \sigma_m - \sigma_a = -554\,\mathrm{MPa}$ is more than three times larger than the compressive stress of point D, $\sigma_{min} = -166\,\mathrm{MPa}$ since $\sigma_{min} = -554\,\mathrm{MPa} = -277\,\mathrm{MPa} \times 2 < -166\,\mathrm{MPa} \times 3 = -498\,\mathrm{MPa}$. Therefore, at point E, even with no crack propagation and no final failure, more severe damage is accumulated regarding crack initiation compared to point D.

Consider F' whose maximum tensile stress $\sigma_{max} = 166\,\mathrm{MPa}$ is the same as point D as shown in Fig. A-6(e). Due to the larger compressive stress $\sigma_{min} = -554\,\mathrm{MPa}$ at point E compared to the one $\sigma_{min} = -166\,\mathrm{MPa}$ at point D, the tensile stress necessary for the fatigue limit can be smaller than $\sigma_{max} = 166\,\mathrm{MPa}$.

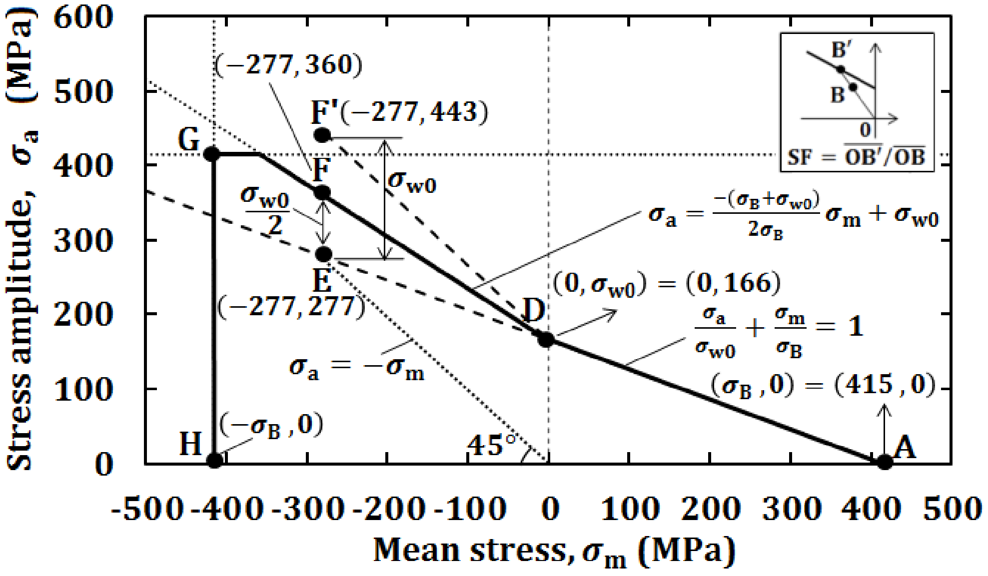

(a) Fatigue limit line A-D-F-G-H

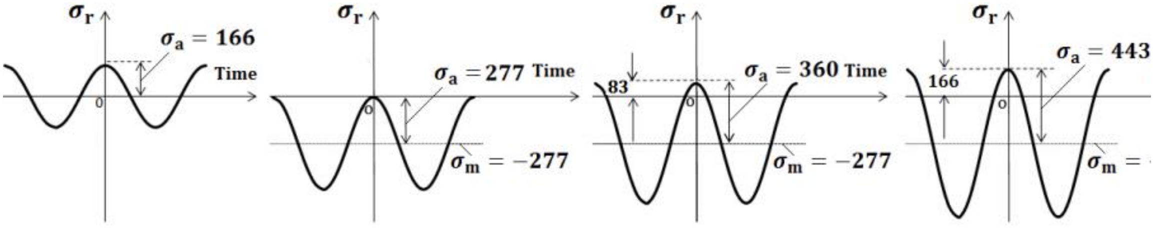

(b) Stress at point D (c) Stress at point E (d) Stress at point F (e) Stress at point F'

Fig. A-6 (a) Fatigue limit lines under large compressive stress; (b) Stress at point D; (b) Stress at point E; (d) Stress at point F; (e) Stress at point F'

Instead, at point E, there is no tensile stress, therefore there is no crack propagation and no final failure as the previous studies indicated [34-36]. In this way, it is found that the fatigue limit point F should be between point D and point F'. In this study, therefore, half value $\sigma_{w0}/2 = 83$ MPa is assumed for this tensile stress at point F as shown in Fig. A-6(d). By drawing the line through point D and point F in Fig. A-6(a), the fatigue limit can be estimated. The range can be expressed by the following equation.

$$\sigma_a \leq -\frac{\sigma_B+\sigma_{w0}}{2\sigma_B}\sigma_m + \sigma_{w0} \quad \text{(A-7)}$$

For large compressive alternative loading, the fatigue limit is determined by Eq. (A-4) to Eq. (A-7), which is expressed by the thick solid lines passing through points A, D, F, G, H in Fig. A-3(a).

B List of publications

1. R.A. Rafar, N.A. Noda, H. Tsurumaru, Y. Sano, Y. Takase. Effect of shaft's rigidity and motor torque on interfacial slip for shrink-fitted bimetallic work roll. In: I.A. Parinov, S.H. Chang, Y.H. Kim, N.A. Noda, editors. Physics and mechanics of new materials and their applications, Springer Cham; 2021, p. 381-388.
2. N.A. Noda, R.A. Rafar, Y. Sano. Stress due to interfacial slip causing sleeve fracture in shrink-fitted work roll. International Journal of Modern Physics B (2021) pp 2140020. https://doi.org/10.1142/S0217979221400208.
3. N.A. Noda, R.A. Rafar, X. Zheng, H. Tsurumaru, Y. Taruya, Y. Sano, Y. Takase. Numerical simulation for interfacial slip for shrink-fitted bimetallic work roll considering elastic deformation of shaft. Journal of Japan Society for Design Engineering (2020). https://doi.org/10.14953/jjsde.2020.2915
4. N.A. Noda, R.A. Rafar, H. Sakai, X. Zheng, H. Tsurumaru, Y. Sano, Y. Takase. Irreversible Interfacial Slip in Shrink-Fitted Bimetallic Work Roll Promoted by Roll Deformation. Engineering Failure Analysis 126 (2021) 105465, https://doi.org/10.1016/j.engfailanal.2021.105465.
5. N.A. Noda, M.R. Aridi, R. Abdul Rafar, S. Zifeng, Y. Sano, K. Takata, Y. Takase. Effect of manufacturing process on residual stress in bimetallic solid roll and bimetallic sleeve roll. Journal of Japan Society for Design Engineering 2021. https://doi.org/10.14953/jjsde.2021.2921
6. R.A. Rafar, N.A. Noda, H. Tsurumaru, Y. Sano, Y. Takase. Novel design concept for shrink-fitted bimetallic sleeve roll in hot rolling mill. International Journal of Advanced Manufacturing Technology (2022) 1-14, 10.1007/s00170-022-08954-2.
7. N.A. Noda, R. Abdul Rafar, Y. Taruya, X. Zheng, H. Tsurumaru, Y. Sano,

Y. Takase, K. Nakagawa, K. Kondo. Interface Slip Verification and Slip Defect Identification in Shrink-Fitted Bimetallic Sleeve Roll Used in Hot Rolling Mill. Tribology International 175, (2022) 107793. https://doi.org/10.1016/j.triboint.2022.107793

8. N.A. Noda, R. Abdul Rafar, X. Zheng, H. Tsurumaru, Y. Taruya, Y. Sano, Y. Takase. Fatigue Strength Analysis of Bimetallic Sleeve Roll by Simulation of Local Slip Accumulation at Shrink-Fit Interface Caused by Roll Rotation. International Journal of Advanced Manufacturing Technology (2022) 1-17. https://doi.org/10.1007/s00170-022-10669-3

Conference paper:

1. Effect of shaft's rigidity and motor torque on interfacial slip for shrink-fitted bimetallic work roll. International Conference on Physics and Mechanics of New Materials and Their Applications, March 2021..
2. Fatigue fracture of shrink-fitted bimetallic sleeve roll considering slip damage. 日本材料学会九州支部　第8回学術講演会講演論文集　〔令和3年11月27日〕.